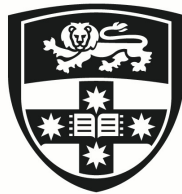


Development of Magnetised Plasma Rockets using Inverse Design and Kinetic Simulation

ALEXANDER G. RYAN



THE UNIVERSITY OF
SYDNEY

Supervisor: Prof. Marcela Bilek
Associate Supervisors: Prof. Iver Cairns and Prof. David McKenzie

A thesis submitted in fulfilment of
the requirements for the degree of
Doctor of Philosophy

School of AMME
Faculty of Engineering
The University of Sydney
Australia

31 March 2023

Declaration

This is to certify that to the best of my knowledge, the content of this thesis is my own work. This thesis has not been submitted for any degree or other purposes.

I certify that the intellectual content of this thesis is the product of my own work and that all the assistance received in preparing this thesis and sources have been acknowledged.

Alexander Ryan, 30 September 2022

Authorship

This thesis contains material published in *Plasma Science and Technology* (2022) 31 085003, in Chapter 2. In all cases, I designed the study, performed the experiments, analysed the data, wrote the drafts of the manuscript and prepared the illustrations.

Alexander Ryan, 30 September 2022

As supervisor for the candidature upon which this thesis is based, I can confirm that the authorship attribution statements above are correct.

Marcela Bilek, 30 September 2022

Abstract

Electric propulsion systems have become a leading solution for accelerating spacecraft, driving an appetite for lifetime, mass, and efficiency improvements. Advancements in additive manufacturing and computing power were leveraged to rapidly design the magnetic fields directly impacting an electric thruster's performance. Fully kinetic particle-in-cell (PIC) simulation methods were also harnessed to characterise plasma sources beyond experimentation. To validate the plasma rocket models, simulations were first performed on existing and well characterised Cathodic Arc devices. The Cathodic Arc PIC models are the first to include continuously generated cathode spots and to model the far-field plasma jet. Results successfully predicted the evolution of the ion charge state energy distributions shown in experimental data. The models also explored novel physics associated with the effects of wave-particle interactions and ion charge state coupling. To address the inverse design problem presented by the magnetic circuits of electric thrusters, the novel use of Monte Carlo sampling and conditional filtering was applied to design the magnetic nozzle of an RF plasma rocket. Following an analysis of designs with PIC simulation, devices were constructed with a helicon source, allowing plasma jet density and ion energy to be determined experimentally, with results further validating the model. A novel evolution-based design and optimisation strategy was developed to overcome the limitations of the sampling method. The objective function integrated a numerical model for plasma behaviour within a magnetic field to assess candidates across a large design space. Designs with different scores were constructed using an array of Neodymium magnets confined within an additively manufactured vessel situated about a helicon source. Experimentation showed a correlation between thrust and objective score, and an agreement with simulation data. The techniques developed in the research process can now be applied to improve the design of electric thrusters and other electromagnetic devices.

Acknowledgements

I would like first to thank my primary supervisor Marcela Bilek, who has been supportive of my autonomy in pursuing a range of areas in plasma and aerospace research, all the while ensuring that I didn't drift too far from having a core upon which to build my dissertation. I am thankful for your intelligent suggestions whenever I run into a challenging hurdle. The fantastic support also extended to my associate supervisors, David McKenzie and Iver Cairns, with all of us regularly meeting despite the complexities associated with global events over the last few years to discuss each engaging research problem as they arose. I found our discussions in these meetings challenging and intellectually stimulating, maintaining my motivation to explore the research within and surrounding the thesis. Thank you, Iver for your insights and constructive criticism, they were greatly appreciated, keeping me from complacency and improving the quality of my writing while also imparting plasma knowledge. I appreciated the backing of CUAVA when travelling to conferences in Australia. Thank you, David, for your constant enthusiasm for my work and assuring me that I was on the right path, coupled with help from your deep knowledge of plasma physics and experimental analysis, especially as experimental issues were a particular challenge over the course of the project.

The use of the vacuum system, as well as the matching network, power supply, and diagnostic apparatus, was critical to much of the experimental work performed herein and would have been a significant challenge without the efforts and support of Stephen Bathgate. I am very thankful for your time and patience in explaining the lab apparatus's ins and outs, as well as your insights into the associated physics. I am also enormously thankful for the support of John Cary, you were vital to me starting this journey when you let me use VSim during my undergraduate thesis, and then extended my use of the code right until the very end of my dissertation, adding the support of the team at Tech-X along the way. In addition to VSim, your words of support throughout our many emails inspired me to tackle this project with gusto.

I greatly appreciated the assistance in the lab throughout the project from Georgio and Khadijeh and their patience while helping me get an incredibly challenging plasma source working correctly. I would also like to my good friend Pascal for his support throughout the project, including the use of his expertise in inexpensive manufacturing.

I am eternally thankful to my amazing partner Raechel, who has been a constant source of unwavering and incredible support despite the seemingly never-ending challenges since I started this journey. You have been an unfailing source of help, strength and patience. I will endeavour to match your support when you need it. I would also like to express my immense gratitude to my family, my parents, Julia and Stephen, and my

siblings Jasper and Isabel. In your special ways, you all built the sturdy emotional foundations on which I could support this adventure, and you have encouraged me through the many trials that had to be overcome to reach this point. I would also like to thank my grandparents, Walter (Mick) and Heather, for their support and patience while I undertook this long project and for reminding me what a special task this is. I dedicate this thesis to my grandparents, Jill and George, from whom I hope that I have inherited many great qualities.

Publications

Published papers

- [1] A. G. Ryan, M. M. Bilek, I. H. Cairns and D. R. McKenzie, ‘Magnetised and unmagnetized axisymmetric particle-in-cell simulations of ion energy distributions in cathodic vacuum arcs,’ *Plasma Sources Science and Technology*, 2022, ISSN: 0963-0252.

Published conference manuscripts

- [1] A. G. Ryan and J. Olsen, ‘Application of particle-in-cell simulation techniques in the analysis and optimisation of magnetic nozzle geometries,’ in *68th International Astronautical Congress*, p. 37 321.
- [2] A. G. Ryan, M. M. Bilek, I. H. Cairns and D. R. McKenzie, ‘Experimental validation of the use of additive manufacturing and metaheuristic inverse design to develop an electrodeless plasma thruster,’ in *73rd International Astronautical Congress*, p. 71 482.

Contents

Declaration	ii
Authorship	iii
Abstract	iv
Acknowledgements	v
Publications	vii
Published papers	vii
Published conference manuscripts	vii
Contents	viii
List of Figures	xi
Chapter 1 Introduction	1
1.1 Fundamentals of propulsion	1
1.2 Fundamentals of plasma physics	4
1.2.1 Plasma waves	6
1.2.2 Plasma generation	8
1.2.2.1 Radio frequency plasma	8
1.2.2.2 Cathodic Arcs	9
1.2.3 Magnetic Mirroring	11
1.2.4 Magnetic Nozzle Physics	11
1.3 Electric Propulsion	15
1.3.1 Electrostatic propulsion	15
1.3.1.1 Electrothermal propulsion	18
1.3.2 Electromagnetic propulsion	18
1.3.2.1 Magneto-plasma-dynamic Propulsion	19
1.3.2.2 Pulsed plasma propulsion	19
1.3.2.3 RF Plasma Propulsion	19
1.4 Particle-in-cell Simulation	21

1.4.1	Electrostatic PIC	22
1.4.1.1	Self-similarity Scaling	24
1.4.2	Electromagnetic PIC	24
1.4.3	PIC Simulation of Vacuum Arcs	25
1.4.4	Simulation of magnetised RF plasma jets	26
1.5	Inverse Design	28
1.5.1	Metaheuristic optimisation	28
1.5.2	Inverse design of magnetic circuits	30
1.5.3	Inverse design of Electric propulsion systems	30
1.6	Thesis overview	31
Chapter 2	Kinetic Simulation of a Cathodic Arc	33
2.1	Introduction	33
2.2	Model description	34
2.2.1	Cathodic arc model	34
2.2.2	Modelling the effect of an applied magnetic field	37
2.2.3	Model accuracy	38
2.3	Results and Discussion	39
2.3.1	Results for the Miniature Arc Gun	39
2.3.2	Evaluation of the Miniature Arc Gun results	46
2.3.3	Applied magnetic field effects	48
2.3.3.1	Ion charge state filtering	55
2.3.4	Potential humps	55
2.4	Conclusions	56
Chapter 3	Simulation and Development of an RF Plasma Thruster	59
3.1	Monte Carlo sampling design	60
3.1.1	Magnetostatic simulation	61
3.1.2	Solution condition function	62
3.1.3	Design solutions	64
3.2	PIC simulation model	65
3.3	PIC simulation results	66
3.4	Experimental validation	69
3.4.1	Thruster development	69
3.4.2	Plasma diagnostics	73
3.4.2.1	Langmuir probe analysis	73

3.4.2.2	RPA analysis	75
3.4.2.3	Vacuum system	76
3.4.3	Experimental results and discussion	77
3.5	Conclusions	80
Chapter 4	Evolutionary Design of RF Plasma Thrusters	82
4.1	Introduction	82
4.2	Methods	84
4.2.1	Evolutionary Algorithm Implementation	84
4.2.2	Magnetostatic simulation	86
4.2.3	Objective functions	87
4.2.3.1	Objective function method 1	87
4.2.3.2	Objective function method 2	88
4.2.4	Particle-in-cell simulation	91
4.3	Results and discussion	91
4.3.1	Optimisation solutions	92
4.3.2	Validation of physical magnet array	94
4.3.3	Simulated performance predictions	95
4.4	Experimental validation	100
4.5	Conclusions	105
4.5.1	Future work	106
Bibliography		107
Appendix		119
Appendix A		119
Appendix B		120
Appendix C		122

List of Figures

1.1	Simplified cross-section of a centrally triggered cathodic arc device, showing the path that a cathode spot takes along the cathode surface towards the anode after an initial trigger.	10
1.2	Axisymmetric diagram of an example magnetic nozzle applied to a helicon thruster using a half-helix antenna situated around a physical vessel in grey, indicating the \vec{B} flux lines in black with an axial parallel into converging-diverging field topology, and the solenoid coils in red. Also shown is the magnetic turning point \vec{B}_{tp} , the magnetic nozzle throat in blue (of area A_t), and the azimuthal current \vec{J}_θ .	13
1.3	Axisymmetric diagram of a typical gridded ion thruster showing the anode vessel in black, the hollow cathodes for breakdown and neutralisation in blue, the black cusp field created by the magnets indicated in red, as well the grids for screening electrons and accelerating ions.	16
1.4	Axisymmetric diagram of a typical Hall effect thruster showing the ferromagnetic structure in grey, solenoids in red, channel in green, the hollow cathodes for neutralisation in black, the annular anode plate in blue along with the axial \vec{E} field, the radial \vec{B} field indicated with black arrows, and the azimuthal current in and out for the page.	17
1.5	Nodal charge density ρ interpolation scheme in terms of weightings w_i for each node of the simulation grid.	23
1.6	The simplified electrostatic PIC process for the axisymmetric domain simulated in this thesis.	23
1.7	An element of the Yee lattice, showing \vec{E} vectors on cell edges and \vec{B} vectors normal to and at the centre of cell faces.	25
1.8	Flowchart overview of the iterative evolutionary algorithm process from an initial population sample to a converged solution.	29
2.1	Diagram showing the process of spot initialisation using an initial assumption of spot density $n_{spot}(A)$ to extrapolate simulated starting spot density n'_{spot} within a simulation cell (B).	35
2.2	Annular simplification of fractal spot propagation showing radius R_s for each spot generation period τ .	36
2.3	Miniature Arc Gun experimental apparatus showing the locations of the cathode (green), anode (red), the simulation region, and the location of the pinhole detector aperture.	36
2.4	Cathodic Arc PIC model setup showing electrostatic boundary conditions and an applied magnetic field (black flux lines).	37

2.5	<i>Al</i> ion number density n_i distribution in axisymmetric (r, z) coordinates $15\mu s$ from the pulse start for the unmagnetised simulation with the anode and cathode shown in red and green, respectively.	40
2.6	Simulated ion velocity (v_z) distributions (solid lines) and corresponding experimental results at $15\mu s$ (dotted lines) for <i>Al</i> (top) and <i>Nb</i> (bottom)[116].	41
2.7	Electrostatic potential field of the simulated unmagnetised (<i>Al</i>) cathodic arc plasma jet at $15\mu s$.	42
2.8	Electrostatic potential at the spatial location of the cathode spot over time (unmagnetised).	43
2.9	Phase-space plots of <i>Al</i> ion kinetic energy (E_k) and axial displacement from the cathode surface (colorised by Z_i). Mean values shown in black.	44
2.10	Plots of <i>Al</i> ion kinetic energy against the product of charge state and potential for all three unmagnetised simulated charge states. The mean trends are shown in black. The red line indicates the function $E_k = Z_i \phi_i - \phi_0 $.	44
2.11	Phase-space plots of <i>Al</i> ion kinetic energy (E_k) and axial displacement from the cathode surface within $10mm$ (colorised by Z_i). Mean values shown in black.	45
2.12	Unmagnetised Al^{2+} ion axial phase-space density plot $15\mu s$ from pulse start, colorised by particle probability density kernel.	46
2.13	Electron axial displacement phase-space, blue dots represent individual super-particles in simulation. Mean value for electron temperature indicated in black demonstrating isothermal trend.	47
2.14	Comparison of <i>Al</i> ion velocity (v_z) distributions for the grounded cathode case (dotted lines) and grounded anode case (solid lines).	48
2.15	Magnetised <i>Al</i> ion number density n_i distribution in axisymmetric (r, z) coordinates $15\mu s$ from pulse start with a solenoid field (black flux lines).	48
2.16	Simulated <i>Al</i> ion velocity (v_z) distributions for the unmagnetised (dashed lines) and magnetised (solid lines) cases.	49
2.17	<i>Al</i> electron number density n_e axisymmetric spatial distributions at $15\mu s$ from the start of a pulse (top) without and (bottom) with a magnetic field.	50
2.18	Electrostatic potential field of the simulated magnetised (<i>Al</i>) cathodic arc at $15\mu s$.	51
2.19	Plots of <i>Al</i> ion kinetic energy against the product of charge state and potential for all three magnetised simulated charge states.	51
2.20	Electrostatic potential at the location of the cathode spot over time (magnetised).	52
2.21	Magnetised Al^{2+} ion axial phase-space density plot $15\mu s$ from pulse start, colorised by particle phase density.	53
2.22	Simulated ion v_z distributions with an applied magnetic field (solid) and are compared with unmagnetised experimental results at $> 90\mu s$ (dotted) [116].	54
2.23	Radial profile of electrostatic potential at $25mm$ from <i>Al</i> cathode surface, with (inset bottom right) a diagram showing the measurement location (1).	54

2.24	The mean value of the charge state Z_i (color bar) as a function of position (r,z) $15\mu s$ from pulse start (top) without and (bottom) with a magnetic field.	55
2.25	Profile of electrostatic potential from the Al cathode surface to the anode for the unmagnetised and magnetised cases, (showing a potential hump in the unmagnetised case) as a function of displacement magnitude $ d(r, z) $. With (inset bottom right) a diagram showing the measurement location (1).	56
3.1	Overview of the Monte Carlo design space sampling for two annular NdFeB permanent magnets drawn from a database of off-the-shelf products.	61
3.2	Axisymmetric simulation domain for performing magnetostatic simulations within FEMM showing the possible regions of magnetic material in red, the plasma source region in blue, the design space in grey, and the radial Robin boundary in green.	62
3.3	Magnetisation simulation results for ten magnet configuration solutions ($F_s \in (1)$) found using Monte Carlo sampling, stacked vertically in axisymmetric coordinates, with blue region corresponding to out of bounds region for plasma generation as shown in Figure 3.2	64
3.4	Cross sections through the centre of the simulated magnetic field topologies for solution 3594 with the inclusion of an annular μ metal shield (left) and without (right). Also shown are the locations of each magnet with magnetisation direction (red boxes and red arrows), the plasma source (blue rectangle), the physical plasma source walls (green), and the magnetic flux lines in black	65
3.5	RF plasma source located within the PIC simulation domain, defined in axisymmetric coordinates with the indicated boundary conditions indicated. Also shown are a magnetic element configuration (blue) (example shown is solution 3594 without μ shielding), the magnetic flux lines (red), the plasma generation region (dark grey), and the physical confining boundary (green). Axes units are in mm.	67
3.6	Number density distributions at $6\mu s$ from simulation start for Argon ions n_i (top row) and electrons n_e (bottom row). Results are for the μ metal shielded variant (left column) and the base design (right column). Magnetic flux lines indicated in red.	68
3.7	Analysis of PIC simulation model data as a function of axial location for both designs, showing parallel (a) and perpendicular (b) Argon ion velocity relative to \vec{B} , mean local magnetic flux density of the plasma jet (c), Larmor radius for each plasma species (d), Argon ion kinetic energy (e), and plasma β (f).	70
3.8	Render of design 3594 showing the magnet vessel, copper helicon antenna and physical plasma nozzle (left), along with the μ metal confinement version (right) with annular μ metal shield also shown.	71
3.9	Physical annular NdFeB magnets sitting inside the machined Teflon housing prior to assembly.	71
3.10	Base antenna module (left) and module for the μ metal variant (left), with both showing the borosilicate physical plasma vessel, RF power leads, and propellant inlets	72
3.11	Fully configured thruster (μ version) with Swagelock propellant line, borosilicate glass nozzle, teflon magnet housing, annular μ metal, and RF power leads.	72

- 3.12 Example $I - V$ trace from a Langmuir probe measurement (left) with the linear fit to the ion saturation region shown in black, the plasma floating potential V_f , and intersection to extrapolated ion saturation current I_{sat} (blue). Also shown is the first derivative of the natural log of the I-V trace (right), giving the electron temperature (dotted line) via Equation 3.5. 74
- 3.13 Locations of each probe within the vacuum system used for this study, showing Teflon coating and locations at an axial displacement from the thruster exit along its central axis. 75
- 3.14 Example RPA probe data analysis with the cumulative ion current I raw data (blue dots), fitted curve (red), and the first derivative of I ($IEDF$) with respect to the magnitude difference between screen potential V_{screen} and probe plate potential V_{probe} . Both y-axes are in arbitrary units. 76
- 3.15 Experimental apparatus exterior showing stainless steel vacuum chamber vessels and the locations of the RF power supply, matching network, probe feed-throughs, and gas inlet (left). Also shown is the interior of the vacuum chamber with thruster mounting location and gas connection (right). 77
- 3.16 RF rocket operating at 50W forward power 15sccm Argon propellant (2mTorr chamber pressure) for both standard mode (left) and design with μ metal confinement (right). 78
- 3.17 Argon ion number density n_i results at different radial and axial locations for the base design at 100W forward power and 15sccm flow rate (left), and overlayed with the corresponding PIC simulation results in blue (right). Dashed black lines indicate the curve fit to experimental results. 78
- 3.18 Axial ion energy results E_k for both the PIC model (blue) and the experimental analysis using an RPA (red with errors) 79
- 4.1 The general software architecture for the evolutionary magnetic topology optimisation loop used for this study. 84
- 4.2 Overview of design space Ω (grey grid) including the exclusion region allocated for plasma generation (blue), and the regions of radially magnetised NdFeB material (red) that comprise a configuration Ω^* . 85
- 4.3 Magnetostatic simulation domain showing the boundary conditions, design space Ω (grey grid), and plasma generation region (blue) as in Figure 4.2. Also shown is the radial magnetisation direction \vec{M} for each magnet (red) in the configuration Ω^* . 86
- 4.4 The Objective function setup for Method 2 showing successful (blue) and unsuccessful (red) particle tracks p_k leaving the injection plane (dotted). Exit boundaries are black and the loss boundary is the 'L' shaped region in grey/pink. 89
- 4.5 RF plasma source located within the PIC simulation domain, defined in axisymmetric coordinates with the boundary conditions indicated. Also shown are a magnetic element configuration (blue) (example shown is Ω_B^*), some magnetic flux lines (red), the plasma generation region (dark grey), and the physical confining boundary (green). Axes units are in mm. 91

- 4.6 Iterative objective function scores $\mathcal{F}_1(\Omega^*)$ (method 1, solid lines) and $\mathcal{F}_2(\Omega^*)$ (method 2, dashed lines) for each generation, both average scores (indicating convergence) (blue) and maximum scores (red) are shown. 92
- 4.7 Average cell density $\overline{\Omega^*}$ for 1000 candidates at six population iterations as they converge from left to right (iteration indicated at the bottom), magnetised regions are indicated by yellow, empty regions are blue, and combined is in green. The population convergence for candidate Ω_B^* using $\mathcal{F}_2(\Omega^*)$ is shown. 93
- 4.8 Magnetostatic simulation results for configurations (left) A (from $\mathcal{F}_1(\Omega_A^*)$) and (right) B (from $\mathcal{F}_2(\Omega_B^*)$), showing NdFeB elements (blue), magnetic field lines (black), and the plasma generation region (red dashed line). 93
- 4.9 Demonstration of the positioning of the magnetic cube elements for test configurations Ω_A^* (top left) and Ω_B^* (bottom left). The magnetic flux lines for the 3D configurations of Ω_A^* (top right) and Ω_B^* (bottom right) are also shown to qualitatively illustrate the similarities to Figure 4.8 with overlays of the physical plasma vessel. 95
- 4.10 Magnetic field-testing apparatus for measuring B_r and B_z in (r, z) using a Hall effect sensor. In this demonstration the magnetic array Ω_A^* is being tested (left). 96
- 4.11 Magnetic flux density $|B|$ along the magnetic array z-axis showing 2D and 3D simulations in dashed orange and solid red lines respectively, as well as the measured results (dotted blue). 96
- 4.12 Magnetic flux lines $|B|$ encompassing the cylindrical plasma generation region (grey rectangle) for 2D and 3D simulations in green and red respectively, as well as the experimentally measured results (dotted blue). 97
- 4.13 Ar ion distributions of $n_i(r, z)$ determined by simulating eight different magnet configurations (A to H) Ω^* in axisymmetric (r, z) coordinates during a quasi-steady state discharge ($5.6\mu s$). Magnetic flux lines are shown in red. 97
- 4.14 Comparison of \bar{v}_z determined from simulation results for all eight tested configurations Ω_i^* 98
- 4.15 Comparison of $\mathcal{F}_2(\Omega^*)^2$ and thrust T measured in simulation showing positive correlation, thus validating \mathcal{F}_2 against PIC simulation (post \mathcal{F}_2 tuning). 99
- 4.16 Example of one of the $3 \times 3 \times 3mm^3$ NdFeB magnets, shown next to a US quarter on a $1cm^2$ grid for size comparison. 100
- 4.17 Plasma source components including copper helicon antenna, propellant injection, and plasma confinement (left) as well as the fabricated PVDF and NdFeB array for Ω_B^* (right). 101
- 4.18 Final assembly for Ω_B^* showing the PVDF vessel with inserted magnets prior to completion (top left), the modified helicon plasma source module (top right), and the assembled final thruster (bottom). 101
- 4.19 Diagram of the plasma diagnostic apparatus used, including Langmuir probe (blue), RPA (green), thruster housing and propellant line (dashed lines), example magnetic flux lines (red), and RF power delivery. Not to scale unless indicated. 102

- 4.20 An optimised RF thruster (system B) inside the vacuum chamber, with magnet array, helicon plasma source, and a Borosilicate/PVDF physical plasma nozzle. 102
- 4.21 RF thrusters using magnetic configurations *A* (left) and *B* (right) operating at 50W power and 25sccm *Ar* flow rate at 2mTorr vacuum pressure. Langmuir probe also shown, located at 100mm from thruster exit. 103
- 4.22 RPA data analysis showing normalised gaussian fits of *Ar* ion energy distributions at 100mm from the thruster exit ($z = 170mm$), and centred on the thruster z -axis for configurations A (dashed line) and B (solid line). 104
- 4.23 Experimentally measured radial profile of *Ar* ion number density n_i at $z = 170mm$ (100mm from thruster exit) for configurations Ω_A^* (blue) and Ω_B^* (red), taken using a round planar Langmuir probe of area $1.75cm^2$. 104
- 4.24 The modified matching network previously developed at the University of Sydney [170], now with a $10\mu H$ inductor to work with the helicon antenna used in the thesis (left), along with the smith chart confirming a match for the vector impedance measured to be 29Ω at 87° (Section 3.4.1) (right). The circuit diagram for the matching network is also shown (bottom right). 119

Introduction

The following research project was motivated by the exponential growth in electric propulsion device use for in-space propulsion, and the development of these thrusters using sophisticated design strategies to maximise performance in an environment where every gram and millimetre counts. Inverse design strategies have until recently been limited in application and scope due to both available computational resources and the additive manufacturing techniques required to construct design solutions with complex geometries. Additionally, the kinetic plasma simulation methods used to determine thruster effectiveness prior to experimentation are continuously improving, and have only recently reached the level of accuracy and speed where they can be used as part of an effective optimisation process. The thesis aims to use kinetic simulation to study the design of the magnetic fields that are applied to plasma jets created by electrodeless thrusters and deposition sources, due to the currently incomplete understanding of the physical mechanisms involved, as well as an examination of the impact magnetic fields have on the performance of these devices. Furthermore, the thesis aims to demonstrate the novel application of inverse design strategies for developing plasma devices with desirable properties. Given the growing interest in the benefits of helicon radio frequency (RF) rockets, namely the extended operation time as a result of electrodeless function and reduced complexity with the omission of a neutraliser, RF rockets were chosen as the core device to perform much of the presented work.

1.1 Fundamentals of propulsion

Thrusters, both chemical and electric, operate with the same basic underlying principle. Momentum \vec{p} is imparted to a vessel over time due to an outflow of material (exhaust) in the direction opposing the desired vector of movement. Thrust \vec{T} , as described in Equation 1.1, mathematically defines the rate of momentum change with time, or force, due to a propulsion system with a fixed exhaust velocity \vec{v}_e

$$\vec{T} = - \left(\frac{d(\vec{p})}{dt} \right) = - \left(\frac{d(m_P \vec{v}_e)}{dt} \right) = -\vec{v}_e \left(\frac{d(m_P)}{dt} \right) \quad (1.1)$$

where m_P is the propellant mass, and t is time. Thrust is a key quantity when describing the performance capabilities of propulsion devices. For convenience, and as the research covered in this thesis concerns spacecraft propulsion, the term spacecraft will be used to describe the object being transported. As a spacecraft is accelerated by a propulsion system its total mass will decrease as stored propellant is converted into the exhaust and lost. It is necessary to define the mass of the spacecraft without propellant as the fixed dry mass m_0 , and the stored propellant mass m_P independently. The combined mass is called the wet mass $m_W = m_0 + m_P$. Thus, by considering Newton's second law, the instantaneous spacecraft acceleration \vec{a} due to the propulsion system is described by the following relationship.

$$\vec{a} = \frac{\vec{T}}{m_{SC}} = \frac{\vec{T}}{m_0 + m_P(t)} \quad (1.2)$$

Or, in terms of spacecraft velocity \vec{v} ,

$$\frac{d\vec{v}}{dt} = \frac{\vec{T}}{m_{SC}} \quad (1.3)$$

Where m_{SC} is the instantaneous spacecraft mass at a time t and $m_P(t)$ is the remaining stored propellant at t . By substituting 1.3 back into 1.2 and rearranging the following relationship is determined,

$$(m_0 + m_P(t)) \frac{d\vec{v}}{dt} = -\vec{v}_e \left(\frac{d(m_P(t))}{dt} \right) \quad (1.4)$$

Simplified to,

$$(m_0 + m_P(t')) d\vec{v} = -\vec{v}_e d(m_P(t)) \quad (1.5)$$

Following integration and re-arranging the following relationship is produced for the time interval between t_i and t_f ,

$$\int_{\vec{v}_f}^{\vec{v}_i} d\vec{v} = -\vec{v}_e \int_{t_f}^{t_i} \frac{1}{(m_0 + m_P(t))} d(m_P(t)) \quad (1.6)$$

By solving the integrals on both sides of Equation 1.6 the following solution is given,

$$\vec{v}_f - \vec{v}_i = -\vec{v}_e \ln \left(\frac{m_0 + m_P(t_f)}{m_0 + m_P(t_i)} \right) \quad (1.7)$$

Equation 1.7 is known as the ideal rocket equation and was first formulated by Tsiolkovsky in 1903, for this reason, it is often called the Tsiolkovsky rocket equation [1]. The quantity $|\vec{v}_f - \vec{v}_i| = \Delta v$ is another key

parameter for describing propulsion system performance, as it predicts the total energy imparted to a spacecraft by a propulsion system. Δv is used to allocate fuel margins prior to launch and determine the feasibility of mission goals given spacecraft characteristics such as wet mass m_W , dry mass m_0 , and propulsion system performance. The linear relationship between \vec{v}_e and Δv implies that increase \vec{v}_e will increase a thrusters performance. Another key quantity, specific impulse I_{sp} , is related to \vec{v}_e by the following,

$$I_{sp} = \frac{|\vec{v}_e \cdot \hat{n}|}{g_0} \quad (1.8)$$

Where g_0 is standard gravity ($9.81 m s^{-2}$) and \hat{n} is the unit vector of the desired direction of motion. I_{sp} is equivalent to the amount of time it would take a thruster to burn through all of its starting propellant m_P while accelerating the spacecraft at g_0 . By combining Equations 1.1 and 1.8, I_{sp} is related to \vec{T} by the following,

$$T(t) = I_{sp} g_0 \left(\frac{d(m_P(t))}{dt} \right) = I_{sp} g_0 \dot{m}_P \quad (1.9)$$

The rocket equation is often written in the following form, determining Δv in the case that all stored propellant is used, and the propulsion system exhibits consistent thrust.

$$\Delta v = I_{sp} g_0 \ln \left(\frac{m_0 + m_P(t_0)}{m_0} \right) \quad (1.10)$$

As thruster-specific impulse is effectively fixed (aside from small changes over time due to performance degradation), space mission trajectory designs use calculations of required Δv and equation 1.10 to allocate required fuel allocations for a spacecraft of mass m_0 .

For electric propulsion systems, there is also an important relationship between thrust power and supplied power by the spacecraft. The electric propulsion system directed kinetic energy over time, or jet power P_{jet} can be determined using the exhaust kinetic energy as follows,

$$P_{jet} = \frac{d}{dt} \left(\frac{1}{2} m_P(t) v_e^2 \right) = \frac{1}{2} \dot{m}_P |v_e^2| \quad (1.11)$$

Or in terms of thrust \vec{T} ,

$$P_{jet} = \frac{|\vec{T}^2|}{2 \dot{m}_P} \quad (1.12)$$

The thrust efficiency η_t is simply the ratio of the jet power to the total power supplied by the spacecraft to the propulsion system P_s .

$$\eta_t = \frac{P_{jet}}{P_s} \quad (1.13)$$

Equation 1.13 can be re-written using 1.12 and 1.9 to show the relationship between the key parameters of thrust \vec{T} , specific impulse I_{sp} , thrust efficiency η_t and the required power supplied by the spacecraft.

$$P_s = \frac{|\vec{T}| I_{sp} g_0 \dot{m}_P}{2\eta_t \dot{m}_P} = \frac{|\vec{T}| I_{sp} g_0}{2\eta_t} \quad (1.14)$$

This shows a linear relationship between required power P_s with both thrust \vec{T} and specific impulse I_{sp} . The relationship is supported empirically by the performance of operational ion and Hall effect EP systems as described in Section 1.3.1.

Another important consideration when developing electric propulsion systems is its mass m_{PS} , as this regulates the feasibility of high mass propulsion systems relative to the total spacecraft dry mass m_0 . The critical parameter to maximise for space missions is the payload mass, or put another way, the dry mass excluding all subsystems, so the propulsion system mass m_{PS} needs to be considered within optimisation efforts. The effect of propulsion system mass can be quantified by the system-specific impulse I_{ssp} , formulated as follows,

$$I_{ssp} = \frac{I_{sp} g_0 (m_W - m_0)}{m_{PS}} \quad (1.15)$$

Where total impulse is $I_{tot} = I_{sp} g_0 (m_W - m_0)$ if all stored propellant is utilised. The use of I_{ssp} has been demonstrated by Koppel et al. as an effective measure of propulsion system effectiveness. Thruster I_{ssp} motivates optimisation efforts to minimise propulsion system mass without compromising thrust efficiency and I_{sp} [2].

1.2 Fundamentals of plasma physics

Plasma, the fourth state of matter and the most abundant in the universe, was first described by Sir William Crookes in 1879 as "radiant matter", and was coined as "plasma" by Irving Langmuir as an analogy to blood plasma [3, 4]. The formal definition of plasma requires a substance to be a quasi-neutral collection of positively and negatively charged particles that behaves collectively, satisfying three criteria related to fundamental plasma properties Debye length λ_D , frequency ω_p , and the parameter N_D [5]. Collective behaviour is a result of

constituent particles acting under the influence of their own states due to induction and other electrodynamic interactions. The displacement in which a plasma is statistically quasi-neutral is the Debye length λ_D , a quantity related to the ion number density n_i and the electron temperature T_e by the following,

$$\lambda_D = \sqrt{\frac{\epsilon_0 K T_e}{n_i q_e^2}} \ll L \quad (1.16)$$

where ϵ_0 is the permittivity of free space ($\epsilon_0 = 8.85 \times 10^{-12} \text{ Fm}^{-1}$), K is Boltzmann's constant ($K = 1.38 \times 10^{-23} \text{ JK}^{-1}$), q_e is the charge of an electron ($q_e = -1.60 \times 10^{-19} \text{ C}$), and L is the length scale or approximate size of the total plasma system. The parameter $K T_e$ gives the electron temperature in eV , so it is often used to define $T_{\text{eV}} = K T_e$ for brevity. In the presence of a surface of fixed potential relative to the plasma, charged particles such as electrons if the surface is positive, will be attracted and form a 'shield' at the surface, thus completely neutralising the \vec{E} field. In reality, however, the electrons close to the surface are non-stationary with thermal energy $K T_e$ and can therefore stochastically escape the potential well created by the surface potential, into the local plasma. This region is called the sheath and has a width close to λ_D , linking with the term for this phenomenon "Debye shielding". If the sheath width λ_D is close to the system length scale L the quasi-neutrality requirement will be violated, large dynamic electric fields will be created, and the collection of charges will not constitute a plasma, hence the condition in Equation 1.16.

A group of charges only behaves collectively, thus constituting a plasma, if the previously mentioned plasma parameter condition $N_D \gg 1$ is satisfied, where N_D is the number of charged particles in a sphere of radius λ_D (the Debye sphere). The condition $N_D \gg 1$ is related to the sheath, as a small number of particles cannot statistically form a Debye shield. Finally, plasma discharges often have a fraction of neutrals that collide with ions and electrons in a mean time interval of τ , so if the neutral collisions are more frequent than the plasma frequency ω_p (see Section 1.2.1) the collection of particles will behave like a gas dominated by physical collisions. The final plasma criteria is therefore $\omega_p \tau > 1$.

The behaviour of constituent particles within a pure plasma is fundamentally governed by physical collisions, Coulombic collisions, and electromagnetic fields (as well as gravity to a small degree). The Lorentz force defined in Equation 1.17 can be used to predict non-collisional particle behaviour due to static and dynamic electric and magnetic fields. The physical behaviour predicted by the Maxwell-Faraday and Maxwell-Ampere equations (1.19 and 1.18 respectively) instigates the collective behaviour of plasma, as any particle motion induce \vec{E} and \vec{B} fields that in turn dictate particle motion via 1.17.

$$\vec{F} = q_e(\vec{E} + \vec{v} \times \vec{B}) \quad (1.17)$$

$$\vec{\nabla} \times \vec{B} = \mu_0(\vec{J} + \varepsilon_0 \frac{\partial \vec{E}}{\partial t}) \quad (1.18)$$

$$\vec{\nabla} \times \vec{E} = -\frac{\partial \vec{B}}{\partial t} \quad (1.19)$$

where \vec{J} is the plasma current density and μ_0 is the permeability of free space ($\mu_0 = 1.26 \times 10^{-6} \text{ Hm}^{-1}$). In addition to collective behaviour, plasma is influenced by externally applied \vec{E} and \vec{B} fields such as those generated by electrodes and electromagnets or permanent magnets. External fields develop forces that act to 'drift' charged particles in the plasma. The Lorentz force on a particle in a magnetic field is the cross product $\vec{v} \times \vec{B}$ from 1.17, thus the particle will gyrate as \vec{v} changes relative to \vec{B} and angular momentum is conserved. The motion of a charged particle in a stationary \vec{B} field can be characterised by the radius of its gyration, the Larmor radius r_L (also called the gyroradius) defined by,

$$r_L = \frac{m_p v_{\perp}}{|q_e \vec{B}|} = \frac{v_{\perp}}{\omega_c} \quad (1.20)$$

where v_{\perp} is the particle velocity perpendicular to the magnetic field \vec{B} , and m_p is the particle mass. Particle gyrofrequency ω_c is important when exploring second-order effects such as plasma waves, with particle gyration effectively becoming an additional mode of oscillation. The motion of the guiding centre of rotation of a charged particle is the particle's drift velocity. One type of drift velocity \vec{v}_E arises due to the effect of \vec{E} applied in addition to a \vec{B} . By cross multiplying both sides of Equation 1.17 and omitting orthogonal vector components, the drift velocity \vec{v}_E can be determined as follows,

$$\vec{v}_E = \frac{\vec{E} \times \vec{B}}{|\vec{B}|^2} \quad (1.21)$$

The particle drift due to $\vec{E} \times \vec{B}$ has implications for plasma behaviour such as confinement, playing a critical role in Hall effect thruster operation by instigating a transverse electron current for plasma breakdown, as well as presenting a core challenge in Tokamak fusion reactors [5, 6]. Other drift forces on charged particles can arise from 1.17 given the dynamics governed by Equations 1.18 and 1.19 when electromagnetic fields are non-uniform or time-varying.

1.2.1 Plasma waves

As a result of the complex collective behaviour of plasmas, there are many non-linear effects involving particle interaction with, and creation of, electrostatic and electromagnetic waves. The most intuitive example of

this behaviour is the pressure waves formed by mutual Coulombic repulsion of ions, directly comparable to sound waves in a typically collisional medium such as gas. In a plasma, electrons will oscillate with ions, thus maintaining quasi-neutrality, although as mentioned prior the electron thermal behaviour will lead to leakage from perfect Debye shielding. The resulting electric fields created by thermal ion repulsion and electron thermal motion drive ion acoustic waves. The ion sound speed v_s is, therefore, a function of electron temperature, ion temperature and ion mass,

$$v_s = \sqrt{\left(\frac{KT_e + \gamma_{ion}KT_i}{M} \right)} \quad (1.22)$$

where γ_{ion} is the ion species adiabatic index, and given that ion compression is in one dimension, the value for γ_{ion} is 3. For the scenario where $T_e \gg T_i$ the formula for v_s is often simplified to omit the $\gamma_{ion}KT_i$ terms. Ions that are accelerated to exceed v_s (or $M > 1$, where M is the plasma Mach number) will also create an acoustic shock wave akin to a sonic boom.

Electrons that are offset from ions within a plasma will accelerate to neutralise the local potential field, however, they will overshoot due to their inertia resulting in oscillations that persist due to a lack of attenuating effects such as collisions. The frequency of these electron oscillations within a plasma is equivalent to the plasma frequency ω_p . As discussed, electrons also have thermal motion, so the frequency of electron plasma oscillations is defined in terms of both ω_p and T_e if the plasma is collisionless and there are no external fields. By combining the oscillations due to electron cyclotron frequency ω_c and plasma frequency ω_p in a direction perpendicular to an applied magnetic field ($\hat{k} \perp \vec{B}$), the upper hybrid frequency plasma oscillations ω_h occur where $\omega_h^2 = \omega_p^2 + \omega_c^2$. Furthermore, an applied magnetic field \vec{B} with \hat{k} close to $\hat{k} \perp \vec{B}$ also instigates ion cyclotron waves Ω_c in the same way as cyclotron waves ω_c . The case when ion wave motion is exactly $\hat{k} \perp \vec{B}$ gives the lower hybrid plasma frequency $\omega_l = \sqrt{\omega_c \Omega_c}$ [5, 7].

Plasma waves discussed so far are electrostatic waves, however electromagnetic (EM) waves also propagate within plasmas, doing so according to Maxwell's equations (such as Equations 1.19 and 1.18). EM behaviour includes the interaction of external sources of EM radiation with plasma as well as the generation of EM waves through plasma oscillations. EM plasma waves are classified into either ion or electron waves. Electron waves occur either with cyclotron resonance (R-waves) or without (L-waves), where R and L waves are circularly polarised in the anti-clockwise and clockwise directions. Ion EM waves include Alfvén waves and Magnetosonic waves, occurring when an applied magnetic field is either $\hat{k} \perp \vec{B}$ or $\hat{k} \parallel \vec{B}$ respectively [5].

1.2.2 Plasma generation

Mechanisms for plasma breakdown require a process for electron acceleration, with collisions between neutral atoms and electrons producing ions and more electrons, resulting in a cascade of particle collisions (plasma breakdown) that rapidly reduces the relative fraction of neutrals in the gas. The process for electron acceleration, and hence plasma generation, can be broken into alternating current (AC) and direct current (DC) methods. DC plasma sources rely on a constant or pulsed current to accelerate electrons in one direction through a potential gradient until they collide with neutral particles or ions. The most common DC plasmas can be found in gas discharge tubes such as Neon lamps, where the potential difference between plates situated at each end of the tube accelerates electrons and ions. AC plasma discharges at low frequencies ($< 1kHz$) operate similarly to DC plasmas with the polarity between electrodes (and thus swapping the direction of potential gradient) switching at the AC frequency, creating electron and ion oscillations [7]. Due to their simplicity glow discharges can often be run in both DC and low-frequency AC modes.

1.2.2.1 Radio frequency plasma

At high frequencies ($> 3MHz$) AC driven conductors produce electromagnetic waves that can ionise gas through non-linear wave-particle interactions, these discharges are classified as radio frequency (RF) plasma. There are three different types of RF plasma sources, including capacitively coupled plasma, inductively coupled plasma, and resonant discharges such as helicon and electron cyclotron resonant (ECR). RF plasmas are typically generated using a driving frequency of approximately $10MHz$, as well as at microwave frequencies in the order of GHz . Capacitively coupled plasma is generated and maintained by the oscillating electric field between two plates, driven at an RF frequency with a wavelength much larger than their separation ($\lambda \gg d_{plates}$), resulting in a rapidly alternating electrostatic acceleration of electrons. The inductively coupled plasma source uses the oscillating electric field from a circular antenna situated around the plasma to create the initial breakdown in a similar manner to a capacitively coupled plasma, however, the electromagnetic waves produced by the antenna coupled with the conductive plasma surface create an evanescent field that maintains the discharge [8]. By definition the evanescent field in the inductively coupled plasma surface is not able to directly accelerate particles within the plasma volume, affecting its efficiency [5, 7].

The generation of helicon plasma was first demonstrated by Lehan and Thonemann in 1965 and developed further by Boswell and others [9–12]. Helicon plasma is generated by employing a helicon antenna, a subset of RF antennas with a physical geometry that facilitates the propagation of electric waves throughout an axially magnetised plasma discharge. These waves are characterised as right-hand circular polarised electromagnetic waves called whistler waves, with a frequency between the lower hybrid frequency ω_l and ion plasma frequency ω_p (Section 1.2), ionising plasma through resonant wave-particle interaction with electrons [5]. This contrasts

with an inductively coupled plasma in which the discharge is maintained by collisional heating, with the aforementioned conductive skin effect reducing power absorption at high densities [7]. Helicon antennas were initially investigated in detail at driving frequencies of 7 to 10 MHz, however, most current systems use 13.56 MHz due to scientific RF band requirements, although a broad range of frequencies have also been demonstrated [12, 13]. A variety of antenna geometries have been shown to create helicon discharges, with the three most common being Boswell, Nagoya, and helix [7, 11, 14, 15]. Each antenna will excite helicon waves at different modes, where each mode classifies a different topology of the generated propagating electric field. The modes are $m \in (-1, 0, 1)$, and antennas can excite up to two different modes depending on the direction of current flow and the direction of the applied \vec{B} field [14].

Microwave plasma sources typically require a resonant cavity to create and maintain the standing electromagnetic waves required for a continuous discharge. However, electron cyclotron resonance (ECR) sources avoid this by applying a fixed external magnetic field that maintains a consistent electron cyclotron frequency ω_c . As with helicon sources, ECR sources rely on resonant wave absorption, by exciting electrons at their local cyclotron frequency electrical power is efficiently coupled with the plasma discharge as the EM fields propagate throughout the plasma volume [16, 17].

1.2.2.2 Cathodic Arcs

Cathodic arcs are an electrostatic process that occurs when a current is induced by the potential difference between a cathode surface and a locally situated anode. The science of the arcs that occur between electrodes such as vacuum arcs is still not completely understood and is an active area of research [18, 19]. The unique process that completes the circuit between the cathode surface and the anode is discrete emissions that propagate along the cathode surface called cathode spots. The high energy density present in the creation of these spots creates a surface ablation containing a dense collection of electrons and ions with high degrees of ionisation, that then undergoes electrostatic repulsion and accelerates to high velocities. The ionisation of the cathode surface material also creates electrons that interact collectively with the emitted ions to develop a plasma discharge. This explosive surface reaction also causes local melting and the ejection of macroparticles of cathode material. As the current continues to flow through the circuit, new spots are formed in consecutive locations to the previous spots, multiplying as the arc propagates radially outwards in fractal patterns [18, 20, 21]. The exact mechanism that facilitates the movement of one spot to another is not completely understood, with current thinking attributing the spot motion to the local imperfections on the cathode surface that result from the explosive ejection of macroparticles and surrounding melting from a prior cathode spot [18, 21].

To initiate a cathodic arc, the circuit between the cathode and anode needs to be completed, achieved using an arc trigger. In a centrally triggered cathodic arc device like that shown in Figure 1.1 there are a few mechanisms involved in triggering the arc. A pin is placed at the centre of the cathode, and for an electric trigger, this pin

is briefly raised to a high potential, creating an initial arc discharge between the trigger pin and cathode. For a thermionically triggered arc, there is still a pin at the centre, however, it is raised to a high temperature that instigates thermionic electron emissions that collide with the cathode and initiate the arc. For reference many vacuum arc thrusters use a thermionic trigger [22, 23]. Once the arc is triggered the cathode spots are set in motion and move towards the anode. The potential difference between the cathode and anode is known as the burn voltage V_{burn} [18, 24].

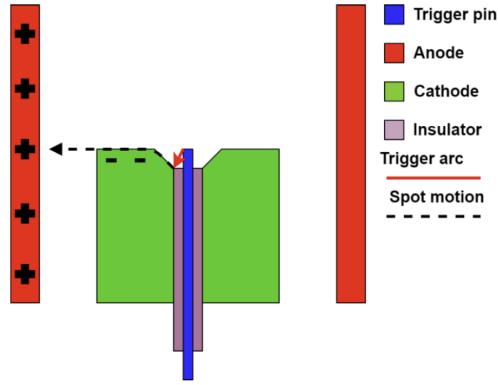


FIGURE 1.1: Simplified cross-section of a centrally triggered cathodic arc device, showing the path that a cathode spot takes along the cathode surface towards the anode after an initial trigger.

The plasma created within cathode spots has several important properties, eventuating in the use of these arcs in several useful applications. These properties include a relatively pure emission (>90% ionisation of the cathode material) of particles from the cathode material (for a range of metals including Molybdenum), ionisation of constituent particles (with most particles exhibiting multiple degrees of ionisation), and the ions leaving the spots to have a high velocity (of the order 1×10^4 to $1 \times 10^5 \text{ ms}^{-1}$) directed normally to the cathode surface [19, 20, 24]. Each degree of ionisation corresponds to a loss of one electron, and a corresponding increase in positive charge by one (the convention is 1+, 2+, 3+ etc.). Cathode spots can achieve values as high as 7+, however, most will be 2+ [18]. To date, the primary application of cathodic arcs has been in the field of deposition. Beginning in the 1950s and 60s it was discovered that refractory metals that could not be easily deposited on surfaces using evaporation could be deposited using vacuum arc processes [18]. By selecting the desired surface coating material as the cathode material, the ions ejected from cathode spots can be directed to form a film coating over a target surface [18, 21]. This is where the properties of high ion purity and direction emission are leveraged successfully.

With the production of charged particles such as electrons and ions come responsiveness to electric and magnetic fields [24]. This property is used in thin film deposition to filter out unwanted macroparticles by redirecting the flow of the plasma along magnetic flux lines. The macroparticles are neutral and have high momentum, therefore they will travel in a continuous direction, unperturbed by the presence of a magnetic field [18, 21].

The mean ion energy of the cathodic arc discharge is of particular interest in the field of arc deposition [25]. Higher ion energies are associated with more cohesive crystalline structures, resulting in desirable properties such as improved conductivity, rigidity, and chemical resistance [18]. For example, diamond-like carbon films require high ion energies (19 – 150eV) to achieve sub-plantation and promote sp^3 bonding [24, 26].

1.2.3 Magnetic Mirroring

Magnetic fields that are parallel to the z-axis (in cylindrical coordinates) and then increase in magnetic flux density at an arbitrary positive axial location can act as a particle mirror. The reasons for this become clear when considering the magnetic moment μ_m of a charged particle moving in a magnetic field as defined in Equation 1.23,

$$\mu_m \equiv \frac{m_p v_{\perp}^2}{2|\vec{B}|} \quad (1.23)$$

The invariance of μ_m and Equation 1.23 produces the relationship $|\vec{B}| \propto v_{\perp}$, therefore by also considering that particle energy is conserved, the velocity component v_{\parallel} will decrease to zero with an increase in $|\vec{B}|$. Particles in the parallel field with a unit vector \hat{v}_{\perp} of zero will be impossible to reflect as $\mu_m \equiv 0$, as mirroring will require particles with sufficient \hat{v}_{\perp} relative to the ratio of magnetic flux density in the parallel field region B_0 to the maximum at the mirror location B_m . It is convenient to define a 'loss cone' of angle θ to delineate the minimum particle \hat{v}_{\perp} to be reflected given a B field ratio,

$$\frac{B_0}{B_m} = \hat{v}_{\perp 0}^2 = \sin^2 \theta \quad (1.24)$$

Here $\hat{v}_{\perp 0}$ is the unit perpendicular velocity in the parallel field region B_0 and the quantity B_0/B_m is also defined as the inverse mirror ratio $R_m^{-1} = B_0/B_m$. Magnetic mirrors are designed such that there is sufficient R_m to confine and direct the bulk of plasma for plasma processing, propulsion, and fusion.

1.2.4 Magnetic Nozzle Physics

To improve the thrust efficiency of electric propulsion devices, an axisymmetric diverging magnetic field can be applied to the plasma discharge to improve the exhaust speed of the thruster through a series of magnetic and electrostatic processes. These applied fields are defined as magnetic nozzles (MN), with the earliest studies into their use as acceleration mechanisms for plasma jets performed by Anderson et al. in 1969, who demonstrated a transition from subsonic to supersonic ion motion at the region of peak magnetic field strength (MN throat), analogous to a solid Laval nozzle used in traditional rockets [27]. Since then there has

been extensive investigation into the mechanism of force transfer from the MN to the plasma jet with both two-dimensional and one-dimensional models [28–37]. Fundamentally, MNs confine and accelerate plasma, converting random thermal energy into axially directed kinetic energy. Momentum exchange ultimately occurs between ions and the magnet that produces the MN (such as a solenoid), and for this reason, the design of MNs is key to the thrust performance optimisation of the electric thrusters that utilise them. An MN can also improve the performance of deposition sources such as cathodic arcs by developing the higher ion energies required for material properties (Section 1.2.2.2) [18]. The use of an MN with plasma sources, generated by both permanent magnets and electromagnets, has been shown to increase the thrust from plasma jets by a factor of two or more [28].

The most common MNs, such as those applied to electron cyclotron resonance (ECR) and helicon sources, facilitate ambipolar diffusion to produce thrust. Ambipolar acceleration (diffusion) is the process of ‘hot’ electrons rapidly expanding and creating a negative potential gradient that accelerates slower low temperature ‘cold’ ions attempting to neutralise the discharge ($T_e \gg T_i$). The electrons that are experiencing deceleration due to the negative relative potential gradient are effectively exchanging energy with the ion species, thus the process of ambipolar acceleration of ions is ‘electron driven’ [5, 28, 38–40]. The efficiency of the energy exchange is due to the size of the electron pressure gradient created by the expanding plasma, and this gradient can be manipulated using an MN by confining and directing electrons. Alternatively, non-electron-driven MNs are used to axially re-direct ions that have already undergone heating or acceleration perpendicular to the desired thrust direction through magnetic mirroring, such as in VASMIR [41].

Although the primary acceleration mechanism is an ambipolar electrostatic field, there have also been investigations into the effects of MN on the formation of current free double layers, as well as electromagnetic acceleration mechanisms such as Hall acceleration, self-field acceleration, and swirl acceleration [42–44].

If the plasma ions remain trapped within magnetic field lines by failing to acquire enough kinetic energy, they will return to the opposing pole of the magnet, thus hitting the other side of the thruster or another part of the spacecraft. The definition of the ion detachment location is an active area of research and has seen significant investigation with a variety of models proposed [41, 45–50]. A good indicator of magnetisation is the Larmor radius r_L (Equation 1.20) of a charged particle, by supposing that r_L is much larger than the length scale of the variation in magnetic flux density, the particle gyro-motion will reduce to a linear trajectory, equivalent to demagnetisation. Generally, electrons remain magnetised to the diverging magnetic field used in plasma processing and thrusters, due to their small mass, while ions will rapidly demagnetise. Therefore, ion detachment is related to the axial diffusion of the plasma jet overcoming the radial force from the magnetic field and not any one particle species, leading to an early definition of detachment as the ratio of plasma pressure to magnetic pressure exceeding unity [41]. In contrast, Ahedo and Merino et al. later assert that the electron diffusion detaches plasma outwards from magnetic field lines rather than inwards and that this induces an opposing

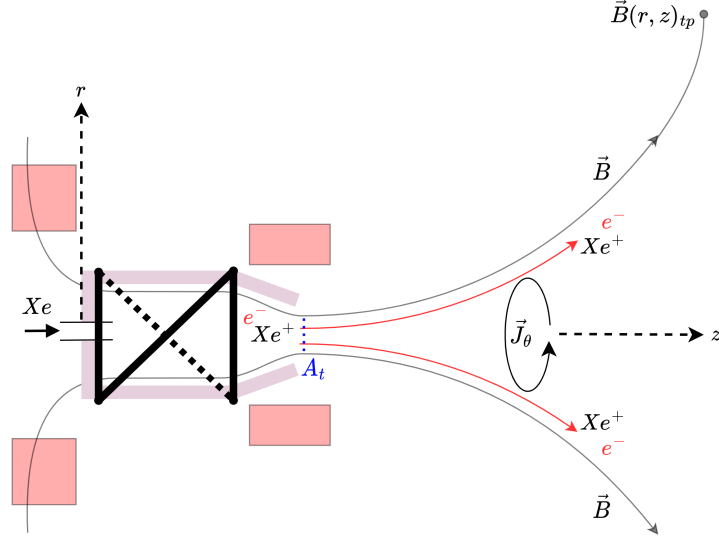


FIGURE 1.2: Axisymmetric diagram of an example magnetic nozzle applied to a helicon thruster using a half-helix antenna situated around a physical vessel in grey, indicating the \vec{B} flux lines in black with an axial parallel into converging-diverging field topology, and the solenoid coils in red. Also shown is the magnetic turning point \vec{B}_{tp} , the magnetic nozzle throat in blue (of area A_t), and the azimuthal current \vec{J}_θ .

magnetic field that drives increased plasma jet divergence confined to an infinite plasma induced MN [28]. Ultimately it is the demagnetisation of the ions that create the detached plasma jet, as once the ions are no longer interacting with the magnetic nozzle directly they drive electron diffusion away from the MN [48].

As discussed, ambipolar or a double layer (CFDL) \vec{E} fields drive ion acceleration within MNs. In addition to these mechanisms, the electron pressure created by the plasma source itself accelerates ions across the sheath at the back of the plasma source into a downstream plume. Thrust was therefore approximated by Fruchman et al. as a function of z ,

$$T = 2\pi \int_0^{r_p(z)} r(p_e + m_i n_e u_z^2) dr \quad (1.25)$$

where p_e is the electron pressure, u_z is the axial ion velocity, m_i is the ion mass, n_e is the electron density (assuming $n_i = n_e$) and $r_p(z)$ is the plasma jet radius as a function of z [29]. Takahashi and et al. describes the total axial force for a plasma expanding into a magnetic nozzle as the combination of three distinct thrust components $T_{total} = T_s + T_w + T_B$. T_s is the thrust due to the peak electron pressure generated by the plasma source and is conserved as a function of axial location z . T_B is the thrust due to the Lorentz force applied to ions as a result of the diamagnetic (azimuthal) electron current and the radial magnetic field B_r , and T_w is effectively the loss of ions through impact with the physical radial plasma source wall, imparting positive and negative axial momentum.

$$T_s = 2\pi \int_0^{r_s} r p_e(r, z_0) dr \quad (1.26)$$

$$T_B = -2\pi \int_{z_0}^z \int_0^{r_p(z)} r \frac{B_r(r, z)}{B_z(r, z)} \frac{\partial p_e}{\partial r} dr dz \quad (1.27)$$

$$T_w = -2\pi \int_{z_0}^\infty r_s m n_w u_r(r_s, z) u_z(r_s, z) dz \quad (1.28)$$

Here, $p_e(r, Z_0)$ is the electron pressure at the plasma source back wall z_0 , r_s is the radius of the plasma source, and n_w is the plasma number density at the source radial wall. The thrust term T_w has been experimentally measured to have a negligible effect on thrust, due to the plasma confinement within the axial magnetic field [51]. The analytical description for T_{total} in the preceding equations does not directly take into account ion detachment through diffusion or demagnetisation and the loss of axial ion momentum flux due to plume divergence. Little et al. developed an analytical thrust and efficiency model for electron-driven converging-diverging MNs with an exhaust region, based on the magnetic field geometry and plasma discharge in a magnetic coordinate system. A dependency on ion Mach number and plasma radius at the exhaust plane was demonstrated, supporting earlier work by Ahedo et al and others [28, 29, 40].

$$M = \sqrt{\frac{m_i v_0^2}{T_e}} = \frac{v_0}{v_s} \quad (1.29)$$

where v_0 is the ion velocity and v_s is the ion sound speed. Additionally, Little et al. asserted that, due to previous observations of over 99% ion separation at the far plume, ion detachment from the magnetic field occurs prior to the turning point of the magnetic nozzle as the majority of momentum has been exchanged by this point, while the electrons detach at a greater axial location [40, 52]. The turning point can be visualised as the location at which an out-flowing magnetic flux tube that starts coincident with the plasma source with radius r_s has diverged to a point where $\vec{B}(r_{tp}, z_{tp})$ is orthogonal to $\vec{B}(r_s, z_0)$, demonstrated in Figure 1.2. Thrust efficiency C_t for a magnetically aligned plasma jet is therefore defined as,

$$C_t = \frac{1}{\bar{n}_t A_t} \iint_{\zeta_{tp}} n (M^2 + 1) \frac{B_z}{B} dA \quad (1.30)$$

where A_t is the throat area, n_t is the mean ion number density at the throat, and ζ_{tp} is the surface of constant $|\vec{B}|$ intersecting the turning point of the MN. The design implications of this for MN optimisation are the minimisation of nozzle divergence while maximising ion Mach number M and overall plasma density n [40].

1.3 Electric Propulsion

Electric propulsion (EP) devices use two fundamental operational processes, plasma discharge creation, and ion acceleration to create momentum flux and thus thrust. How each of these processes is achieved is the differentiating factor between different thruster technologies. EP devices can be split into three broad categories including electrostatic, electrothermal and electromagnetic (EM), based on the fundamental electrodynamic physics they use to drive ion acceleration [53].

1.3.1 Electrostatic propulsion

Electrostatic propulsion systems fundamentally use the potential gradient created by an electrode to accelerate ions via the Coulomb force $\vec{F} = q_i \vec{E}$ thus generating thrust in the opposing direction. The number of different EP technologies continues to grow, however, the two that have been flown the most in space are Ion thrusters and Hall effect thrusters.

Gridded ion thrusters have significant flight heritage, having flown on the Dawn spacecraft on the mission to explore Vesta and Ceres [54]. These devices, as illustrated in the diagram in Figure 1.3, use the potential difference created by electrically charged grids to accelerate ions and produce thrust. The gas propellant is injected into a vessel that also serves as the anode, and a hollow cathode injects electrons into the vessel where they undergo electrostatic acceleration towards the screening grid via Equation 1.17 and collide with propellant neutrals, thus generating a DC plasma discharge. The first electrostatic grid, the screening grid, has a positive bias to extract electrons, and the second grid has a negative bias to accelerate the ions that pass through the screening grid. Gridded ion thrusters typically incorporate a magnetic cusp field within the anode vessel to confine the plasma and improve propellant ionisation by minimising wall losses and sputtering. In addition to DC discharges, the use of RF sources to supply operating plasma for gridded ion thruster systems has also been demonstrated with both ECR, on the microwave discharge ion thrusters used to manoeuvre Hyabusa-1, and inductively coupled plasma in the Busek BIT-3 thruster [55, 56]. The ion jet exiting the thruster system is positively charged and could remain coupled to the thruster and spacecraft, minimising thrust and potentially causing damage to subsystems, therefore the ion jet requires neutralisation [6]. Neutralisation of the plume is achieved by employing an external hollow cathode to supply a beam of electrons that couple with the ion jet and balances the net charge. The unimpeded exhaust velocity for the ion jet for a gridded ion thruster can be determined as a function of the acceleration grid potential V_a using Equation 1.31,

$$v_{ei} = \sqrt{\frac{2q_e V_a}{m_i}} \quad (1.31)$$

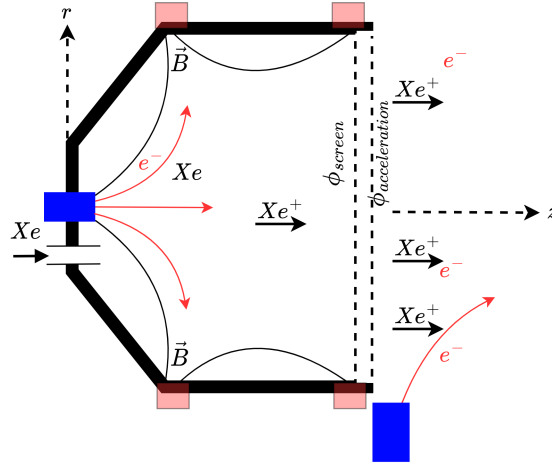


FIGURE 1.3: Axisymmetric diagram of a typical gridded ion thruster showing the anode vessel in black, the hollow cathodes for breakdown and neutralisation in blue, the black cusp field created by the magnets indicated in red, as well the grids for screening electrons and accelerating ions.

The relative potential of each grid, as well as their displacement and hole sizing, are critical to the optimisation of performance, with each set of holes and fields across the grids forming an array of ion optics that create individual jets of ions. The change in the behaviour of the ion optics between grids due to grid erosion is the key factor affecting gridded ion thruster lifetime, with erosion primarily caused by sputtering and degradation due to particle impingement on the surfaces of the grids [57, 58]. In addition to using a hollow cathode to create a plasma discharge inside the anode vessel, gridded ion thruster systems using RF breakdown stages have been recently demonstrated such as BIT-3, with RF plasma sources overcoming the high voltage and high-temperature requirements of hollow cathodes [59].

As with gridded ion thrusters, Hall effect thrusters have a lot of in-space heritage, typically exhibiting more thrust efficiency and low specific impulse than gridded ion thruster devices. They are being used extensively to manoeuvre satellites and have been demonstrated on platforms undertaking lunar operations such as on SMART-1 [60, 61]. A Hall effect thruster uses a radial \vec{B} field and an axial \vec{E} field to create and confine an azimuthal electron current \vec{J}_θ via Equation 1.21. The axial \vec{E} field is produced by a circular anode at the base of a cylindrical channel, into which propellant gas is injected, and the radial \vec{B} field is generated using electromagnets or permanent magnets situated around the channel as illustrated in Figure 1.4. The electrons are supplied by a hollow cathode at the thruster channel exit, and while drifting towards the anode the electrons collide with propellant neutrals to create ions and more electrons. The ions within the resulting Hall discharge are accelerated by the potential gradient created between the positive anode and the negative azimuthal electron current \vec{J}_θ trapped towards the thruster exit, with the band of trapped electrons analogous to the grid in a gridded

ion thruster. In addition to supplying electrons for the plasma discharge, the hollow cathode also neutralises the ion jet from the Hall effect thruster in much the same manner as in a gridded ion thruster [6].

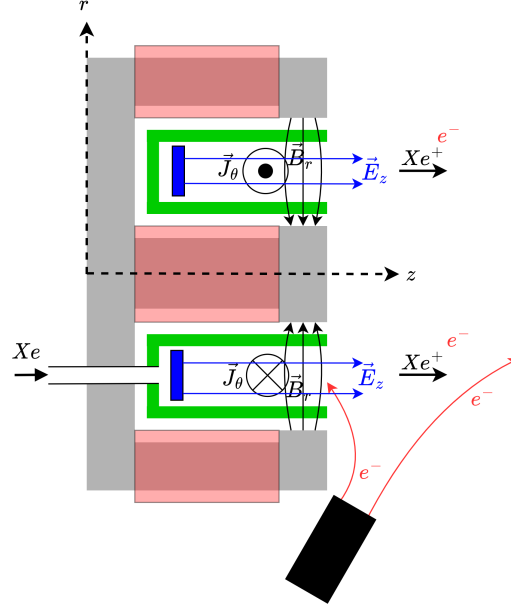


FIGURE 1.4: Axisymmetric diagram of a typical Hall effect thruster showing the ferromagnetic structure in grey, solenoids in red, channel in green, the hollow cathodes for neutralisation in black, the annular anode plate in blue along with the axial \vec{E} field, the radial \vec{B} field indicated with black arrows, and the azimuthal current in and out for the page.

There are several design considerations for Hall effect thruster performance, such as the erosion of the channel walls due to ion bombardment, and plasma instabilities due to fluctuations in hollow cathode emissivity [62–64]. To mitigate the erosion of channel walls, more sophisticated $\vec{B}(r, z)$ field topologies have been implemented that confine the plasma in a way that reduces channel impingement, creating a 'magnetic shield' [65].

The hollow cathodes typically used in Hall effect thruster and gridded ion thruster systems operate by thermionic emission, requiring a heating element that takes up to 600s to heat up and produce the required currents. The hollow cathode heater is also a primary failure mechanism for Hall effect thruster and gridded ion thruster systems, so hollow cathodes are being innovated to produce the high currents required for a thruster while removing the heating element [66, 67]. Direct heaterless hollow cathode development was first demonstrated by Schatz et al. following an initial demonstration of a heaterless breakdown mechanism by Aston et al. [68, 69], and has since been integrated into commercial thrusters. HHCs use an electrical arc to heat the low work function material such as Lanthanum hexaboride that would ordinarily be heated by a heating element. Once the high voltage arc initiates plasma breakdown, a lower voltage is used to maintain the discharge along with the flow of propellant gas [68].

In addition to Hall effect thrusters and gridded ion thrusters, electrospray thrusters such as Field Emission Electric Propulsion (FEEP) thrusters have seen use at power levels from $50mW$ to $20W$ [70, 71]. These devices use an ionic liquid wetted to a thin rod and then drawn out into a cone shape called a Taylor cone by the potential of an extractor plate situated above the rod. Following extraction, the ions are then accelerated by the voltage between the extractor plate and an accelerator plate in a similar configuration to the ion optics of a gridded ion thruster [72]. While these devices can be run at low power levels, they can be used to manoeuvre nanosatellites such as 1U CubeSats.

The erosion-based performance degradation and failure modes present in electrostatic EP systems are a limiting factor in their broader use as in-space propulsion solutions. Additionally, the requirement for ion plume neutralisation adds more complexity to a propulsion system's design and subsystem power management, increasing cost, points of failure and I_{ssp} , as hollow cathodes are often the most complex component in an EP system [73]. Alternative propulsion technologies such as electrodeless thrusters seek to avoid designs requiring a hollow cathode for the discussed reasons.

1.3.1.1 Electrothermal propulsion

Electrothermal propulsion devices are the closest EP technologies to traditional chemical propulsion, as they use heated propellant accelerated through a converging-diverging nozzle. Resistojets use an electric heating element (such as a tungsten filament) to heat propellant gas that is compressed and then expands at high velocity. Arcjet thrusters use a sustained electric arc between a central cathode rod and a surrounding anode that also acts as a converging-diverging nozzle to rapidly heat and accelerate propellant gas. Arcjets are capable of higher I_{sp} due to the larger thermal energy densities of electrical arcs. Arcing leads to rapid erosion through ablation, and sputtering, changing the physical geometry and electrostatic behaviour of the device over time, thus compromising performance [74].

1.3.2 Electromagnetic propulsion

In contrast to electrostatic thrusters, EM thrusters accelerate ions through interaction with both electric and magnetic fields. Many electric propulsion systems use magnetic fields to transport electrons and create a discharge such as Hall effect thrusters (Section 1.3.1), however, ion acceleration in these devices is primarily due to an electrostatic process dictated by Coulombic forces. EM propulsion relies on the Lorentz force to accelerate ions, comprising a spectrum of different technologies that utilise magnetic and electric fields with differing relative portions.

1.3.2.1 Magneto-plasma-dynamic Propulsion

Magneto-plasma-dynamic (MPD) thrusters consist of a central cathode rod, an anode shaped to align with the electric field of the operating plasma, and an externally applied or self-generated magnetic field. A Self-field (SF) MPD operates at large anode currents, as the current between electrodes induces an azimuthal magnetic field \vec{B}_θ that, in combination with the plasma current \vec{j} , develops a Lorentz force acting on ions $\vec{F} = \vec{j} \times \vec{B}_\theta$ [53, 75]. SF MPD thrusters are being developed for use at high power levels ($> 100kW$), where they operate most efficiently. The development of SF MPD devices is thus prohibitively expensive for many organisations due to the overhead costs for high-power EP development (such as the vacuum chamber), and in-space testing is currently infeasible due to the available power margins on active spacecraft (for reference the International Space Station (ISS) has a maximum power output of $120kW$) [76]. Applied-field (AP) MPD thrusters use an externally applied MN, allowing for lower anode currents and therefore lower power requirements, resulting in an increase in investigation [77]. During AP MPD operation a Lorentz force is applied to ions by the MN and the azimuthal current generated by the anode-cathode potential difference and the perpendicular magnetic field $\vec{F} = \vec{j}_\theta \times \vec{B}$. An AP MPD thruster was demonstrated by Boxberger et al. to perform at 62% thrust efficiency and an I_{sp} of $4665s$ at $100kW$, exemplifying the maintained interest in these devices [77, 78]. MPD thrusters experience electrode degradation over time due to ion bombardment and sputtering, a limiting factor for extended use that they share with many other EP devices [79].

1.3.2.2 Pulsed plasma propulsion

A pulsed plasma thruster operates in a similar way to a vacuum or cathodic arc source (Section 1.2.2.2), as an igniter plug will trigger a high-energy arc pulse between a conductive surface and an anode. The conductive surface material will ablate due to the high arc temperature into macro particles and plasma, with the ejected plasma jet creating thrust [80]. Pulsed plasma thruster devices contain solid propellant in the form of a rod that is held in place between an anode that is either a cylinder for coaxial pulsed plasma thrusters or two plates in traditional pulsed plasma thrusters. Recently vacuum arc sources such as cathodic arcs have been demonstrated as coaxial pulsed plasma thrusters, making use of the dense solid propellant material and high I_{sp} due to the large energy density of electric arcs [19, 81–83]. The rapidly changing electric and magnetic fields created by the pulsed plasma and electrodes result in complex electrodynamic behaviour that is currently actively researched. The potentially unstable behaviour of pulsed plasma thrusters at high power has limited their use at levels greater than $100W$ [53, 84, 85]

1.3.2.3 RF Plasma Propulsion

RF plasma thrusters use an antenna (made of a conductive material such as copper) to ionise a propellant gas in the presence of a magnetic field, creating a high-velocity plasma jet that facilitates thrust production [14].

There is typically no physical contact between the antenna circuit and the operational plasma, thus most RF plasma thrusters are considered to be electrodeless plasma propulsion devices, overcoming the limitations of the electrode or channel degradation over time experienced by other EP devices such as ion and Hall effect thrusters [86]. As discussed in Section 1.2 these devices operate by coupling a high-frequency electric field with the electrons within a plasma discharge following an initial breakdown, with forward power levels ranging from $< 5W$ to over $100kW$ [41, 87]. The constituent electrons within the plasma discharge exchange their thermal energy with non-energetic 'cold' ions through ambipolar acceleration within an expanding magnetic field, creating a directed kinetic jet of ions that impart thrust. Thruster concepts using RF plasma generation have been studied since the Variable Specific Impulse Magnetoplasma Rocket (VASMIR) precursors in the 1970s at MIT and early electron cyclotron resonance (ECR) thrusters [41, 76, 88].

There has been an influx of research into helicon thrusters due to their efficient production of high-density operating plasma due to the propagating electromagnetic field (Section 1.2)[89]. Recent thrust efficiency improvements by groups such as Takahashi et al. have demonstrated η_t values of up to 20% at a supplied power of $6kW$ [90]. Currently, the two systems closest to widespread commercial operation in space are the Maxwell and REGULUS propulsion systems developed by Phase Four and T4i respectively. The Maxwell block 2 system exhibits $13mN$ of thrust at $500W$ with $700s$ I_{sp} , while the REGULUS-50 system has a thrust of $0.55mN$ at $50W$ and an I_{sp} of $550s$ [91, 92]. These performances are still behind the electrostatic gridded ion thruster and Hall effect thruster devices, requiring further optimisation outside of their utility of consistent performance over time[93].

Helicon double layer thrusters are a relatively recent concept that use the electrostatic potential drop across a current-free double layer to accelerate ions within a diverging magnetic field, following plasma generation due to a Helicon antenna [44], as an alternative to the ambipolar acceleration mechanism used in other helicon thrusters. The potential difference across the double layer can be of the order of $10eV$ and given the short width of the double layer (of magnitude $10\lambda_D$), ions can be accelerated to over $10 km.s^{-1}$. There are still challenges associated with the operational reliability of RF thrusters using a current free double layer such as helicon double layer thrusters, however, research into their use is still active [94]. The use of permanent magnets instead of electromagnets has been suggested as an avenue for optimising the power requirements for helicon and other RF thrusters. The optimisation of permanent magnets for use with RF thrusters is an ongoing engineering challenge [89, 95].

As discussed in Section 1.2.2 plasma can be also generated using microwaves through electron cyclotron resonance (ECR). These thrusters, distinct from the ECR-based gridded ion thruster previously covered, operate in the same basic configuration as helicon thrusters with the use of a magnetic nozzle to produce thrust by directing RF plasma [96]. Despite being in development for as long as helicon thrusters, there have been no in-space demonstrations so far. The system that is closest to the demonstration is the MINOTAUR device, with a

thrust efficiency of 16% and a max I_{sp} of 1001s [97]. Most ECR thrusters use a centrally located antenna that is in contact with the plasma, potentially leading to performance degradation due to erosion. Erosion can be overcome by using a coaxial antenna, however, these thrusters have a lower thrust efficiency than competing thrusters (5% opposed to 10-20%)[98, 99].

The large commercial RF plasma thruster project VASMIR is a two-stage device, the first is a helicon antenna that creates an RF plasma discharge in the presence of an axial magnetic field. Plasma is then directed using a series of solenoids to the second antenna while maintaining a relatively low ion temperature, and at the second antenna, the ions undergo ion cyclotron resonance heating (ICRH). Due to the large axial magnetic field ($> 1T$) created by the surrounding solenoids, as the ICRH stage heats and accelerates collisionless ions in a direction perpendicular to the applied field, ion confinement is maintained. The resulting high-energy ions are then shaped by a diverging magnetic field (magnetic nozzle, see Section 1.2.4) into an expanding jet of axial plasma. As ICRH exhibits efficient energy transfer (up to 100%), the device has the capacity for significant efficiency [75]. The VASMIR has since been continuously optimised and the current design (VX-200SS) exhibits a η_t of up to 70% and an I_{sp} of 4900s at 200kW with Argon propellant [76]. Adoption of this system is currently prohibited by high power requirements for the electromagnets and RF stages, as well as the overall system weight.

1.4 Particle-in-cell Simulation

Particle-in-cell (PIC) simulation is a method for simulating plasma dynamics using a series of iterative calculation steps, performed on individual particles within a gridded domain at discrete timesteps [100]. PIC simulation codes are kinetic and propagate particles according to the Lorentz force equation, thus they should in principle be accurate as there are very few assumptions made about plasma behaviour (Section 1.2). PIC is suited to problems with non-Maxwellian energy distributions that cannot be accurately solved using magnetohydrodynamic (MHD) or other fluid simulations, such as magnetised collisionless plasma jets. Because of this, these codes can simulate most forms of plasma, including plasmas found in electric propulsion systems that cannot be simulated by other means. With adequate resolution, electrostatic codes can capture all complex non-linear dynamics that arise through potential differences [100].

To improve performance, hybrid codes are sometimes used, treating a selection of particle species, such as electrons or neutrals, as a fluid [100]. Hybrid PIC models require complex treatment if non-linear behaviour is an important component of the simulated plasma, as fluid models need to incorporate analytical descriptions of these effects. For this reason, hybrid PIC codes are developed and validated for specific types of plasma [101, 102].

PIC algorithms can be implemented in 1,2, and 3-dimensional Cartesian coordinates, however for most simulations of plasma jets and electric propulsion devices it is convenient to use a 2-dimensional axisymmetric

coordinate system. This can present additional challenges when dealing with plasma behaviour near and along the axis, although this can be overcome with cylindrical normalisation and weighted super-particles [103].

The primary software used to perform PIC simulations in this thesis is VSim 11, developed by the Tech-X Corporation [104]. This software was previously used to simulate plasma discharges, including electric propulsion systems, such as the Hall effect thruster simulation by Miranda et al. [104]. The PIC computations were performed on the ARTEMIS cluster at the University of Sydney. VSim was chosen due to the improved run-time efficiency over in-house PIC codes, as well as the ability to run effectively on a cluster.

1.4.1 Electrostatic PIC

Electrostatic PIC simulation omits the propagation of time-varying electric and magnetic fields, focusing on the behaviour of particles in an evolving electrostatic field created by the plasma. For the convenience of calculation, simulated particles are assumed to be a collection of multiple real particles (super-particles), leveraging the collective behaviour of the plasma. These super-particles are injected into the simulation domain within a specific volume and density with randomised positions, and the initial velocities are normally distributed in each dimension according to initial assumptions of thermal energy.

The charge density is computed for each node on a simulation grid using the super-particle positions and shapes, with a weighting relative to the distance from each node, as illustrated in Figure 1.5. The electrostatic potential ϕ is determined for each iteration by applying the discretised Poisson equation (Equation) in each direction at the nodes. The electric field \vec{E} in each cell is calculated from the potential difference between two nodes. The process specific to our PIC method is summarised in the flowchart shown in Figure 1.6, where m_s is the particle mass, v_t is the particle velocity transverse to the (external, time-invariant) magnetic field \vec{B} , Δx is the cell size, and Δt is the timestep. Performance improvements can be made to the charge electric field calculation from charge density by first performing a Fourier transform on the charge distribution within the domain, solving Poisson's equation in Fourier space, and then performing another Fourier transform to determine the \vec{E} field in real space [105].

$$\nabla \vec{E} = \frac{\rho}{\epsilon_0} \quad (1.32)$$

Particles are propagated by the finite difference Lorentz force equation, using the 'Leap Frog technique' [100] for the Buneman-Boris particle push scheme, incorporating the calculated nodal electric field values and imported magnetic field data. The Buneman-Boris scheme uses a half-timestep \vec{v} update using the \vec{E} field that precedes a full-timestep \vec{v} update using the \vec{B} field, followed by another half-timestep \vec{E} field update [100, 106]. Since

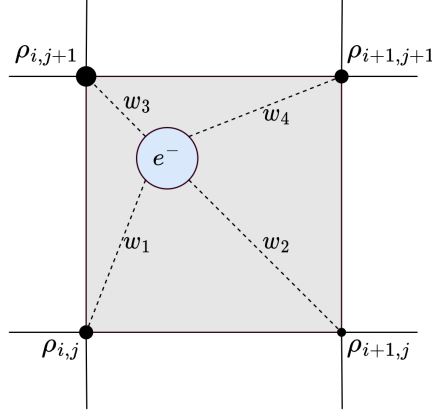


FIGURE 1.5: Nodal charge density ρ interpolation scheme in terms of weightings w_i for each node of the simulation grid.

the simulation setup is assumed to be electrostatic, the magnetic fields are generated using the magnetostatic simulation software FEMM and then interpolated and imported into VSim as static fields [107].

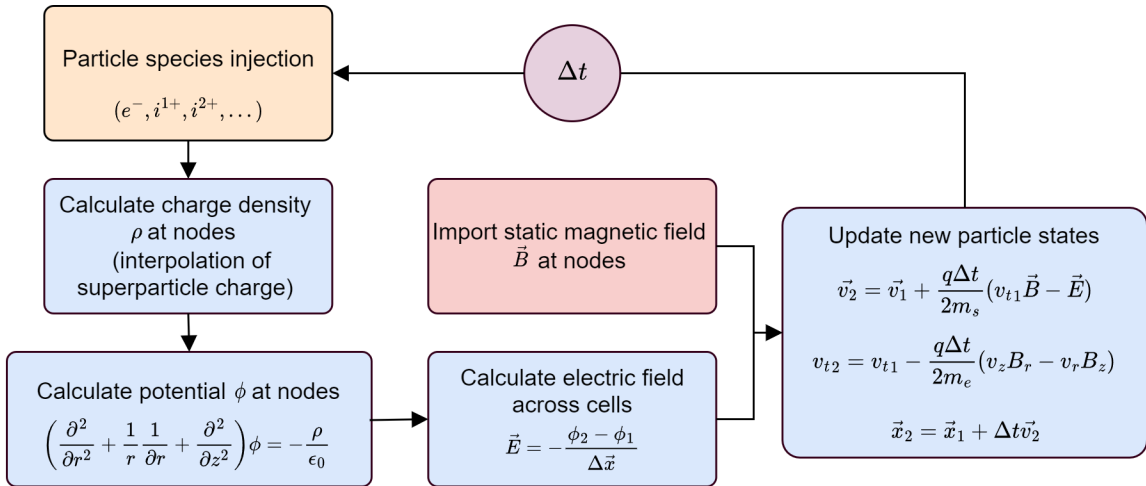


FIGURE 1.6: The simplified electrostatic PIC process for the axisymmetric domain simulated in this thesis.

A process that is often incorporated into PIC models is the effects of collisions on plasma behaviour, including ionisation, recombination, and energy exchange. One way to achieve this is to pair super-particles within the simulation domain that are positioned close to one another relative to their cross-sectional areas, and then simulate a Coulombic collision based on their charge states [108]. Doing this for all particle pairs can be computationally expensive, so often a Monte Carlo collision (PIC-MCC) approach is used whereby each particle within a domain cell undergoes a collision based on a sample from a probability distribution [100]. The expensive nature of particle collisions in PIC algorithms makes collisionless plasmas less computationally intensive as these effects are ignored.

1.4.1.1 Self-similarity Scaling

Particle-in-cell simulation times can be significantly reduced by utilising a method called self-similarity scaling. This method scales the length scale of a simulation with a scaling factor ζ , and re-scales all other physical properties such that the system reproduces the plasma dynamics of the original model [109–111]. The scaling relies on the definition of invariant order parameters such as thrust efficiency and the Knudsen number (ratio of the electron mean free path λ_{eN} to system length scale L), to derive relationships between scaled parameters and the length scale L of the thruster model. The performance increase for timesteps required for steady-state convergence $N_{\Delta t}^*$ are scaled by $N_{\Delta t} = \zeta^{1/2} N_{\Delta t}^*$, the number of cells required in the simulation domain $N_{\Delta r,z}^*$ scales according to $N_{\Delta r,z} = \zeta N_{\Delta r,z}^*$, and the number of real particles N_p^* scales with $N_p = \zeta^2 N_{\Delta r,z}^*$.

Research on particle-in-cell simulation of Hall effect thrusters in axisymmetric coordinates was used to test the self-similarity method by Tacconga et al. [109], and this has been extended for use for demonstration with other electrostatic propulsion device simulations [112].

1.4.2 Electromagnetic PIC

Electromagnetic (EM) PIC differs from PIC primarily by solving Maxwell's equations (1.19 and 1.18) at each timestep, as opposed to Poisson's equation in the previously discussed electrostatic case. Efforts to solve EM fields using finite difference methods date back to the work of Courant et al. in 1928 where they were used to solve the wave equation in two-dimensions [113]. The method for computationally solving Maxwell's equations for EM PIC is called the Finite-difference time-domain method (FDTD) or the Yee method, as described by S. Yee in 1966. The Yee method uses the relative locations of \vec{E} and \vec{B} fields on a three-dimensional lattice mesh to solve the curl operations required for the circuit and induction laws (1.19 and 1.18), as shown in Figure 1.7. If the cell in Figure 1.7 is shifted in space by $(\frac{\Delta x}{2}, \frac{\Delta y}{2}, \frac{\Delta z}{2})$ the \vec{B} vectors now lie on cell edges, and \vec{E} will lie on the faces. Furthermore, as the time-dependent change in \vec{E} and \vec{B} is dependent on the previously determined $\nabla \times \vec{E}$ and $\nabla \times \vec{B}$ [114].

The Lorentz force equation (1.17) is used to propagate particles in the same way as the method in Figure 1.6 if the Boris push method is used. Instead of the weighted nodal charge density ρ as determined using each particle position \vec{x}_i , the EM solver finds the current density \vec{J} as determined by particle position \vec{x}_i and velocity \vec{v}_i then interpolated to the simulation grid edges. Poisson's equation can still be used along with Gauss's law to test consistency at each timestep. If Equation 1.32 is not consistent during the simulation, then the current density is violating continuity, using 1.32 to then correct \vec{E} by applying the difference as a bias is called the Boris correction. While EM PIC can capture deeper physics than PIC, the light speed propagation of EM waves requires smaller timesteps that can lead to computational requirements far exceeding those available to researchers.

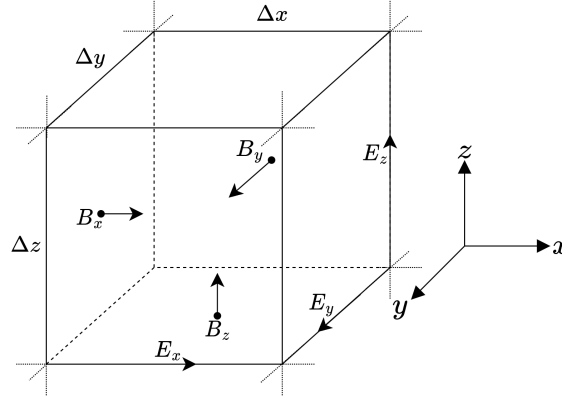


FIGURE 1.7: An element of the Yee lattice, showing \vec{E} vectors on cell edges and \vec{B} vectors normal to and at the centre of cell faces.

1.4.3 PIC Simulation of Vacuum Arcs

At present, the nature of many processes that comprise a cathodic arc discharge is not fully understood [18]. Simulation models can simultaneously provide a high-resolution examination of phenomena in energetic plasmas in space and time, producing a detailed view of processes that are not yet possible to study experimentally [115]. Simulation can therefore enable an improved understanding of the unexpected properties of the energy distributions of the ions in an arc discharge [116], and the propagation of ions against the applied potential difference [18], a dynamic that is uncommon for a normal glow discharge plasma [25, 117]. Additionally, the generation of broadband fluctuations (“multi-coloured noise”) in the arc burn voltage is not yet fully explained [118]. Furthermore, applying magnetic fields to arc discharges accelerates the ions (increasing the ion energies) for various cathode materials, and simulations can explore the mechanisms driving this effect [24, 119]. The simulation of dense energetic plasmas, including arcs, is an active research area. Attempts have been made to accurately capture the complex dynamics of vacuum arcs using Magnetohydrodynamic (MHD) simulations [120, 121] and of individual cathode spots using test-particle simulations [120, 122–126]. Full particle-in-cell (PIC) simulations are kinetic, so they can be used to study the development and properties of non-Maxwellian distributions (a limitation of MHD simulations). PIC simulations probe dynamics at a high level of detail, which requires more computational resources per particle than test particle simulations, and thus are limited by available computational resources [100].

PIC simulations performed by others have led to insights into fundamental questions in cathodic arc research. The small-domain test-particle simulations of Cooper et al. showed that spot expansion is caused by electron evaporation, followed by explosive ion acceleration driven by the mutual repulsion of a positively charged core [126]. Timko et al. and Kaufmann et al. simulated vacuum arc spots using the self-similarity of cathode craters to produce hybrid (fluid electrons and kinetic ions/neutrals), three-dimensional simulations that incorporate surface ablation and macroparticle formation [122, 127]. 2D axisymmetric hybrid simulations of the ion dynamics at

the cathode surface with and without an applied axial magnetic field were performed by Shmelev et al. [125, 128]. These simulations used a magnetised fluid model for electrons and a PIC model for ions and neutrals, to investigate the structure of the plasma jet from a vacuum arc spot. Of particular interest in the present study is the simulation of a cathodic arc with two successive spot generations, starting the investigation of spot combination into a jet [125]. Recent research by Yang et al. further demonstrated the applicability of electrostatic PIC modelling to small-gap vacuum arcs [123]. These simulations concern micrometre to millimetre scale vacuum arcs, and thus motivate the simulation of cathodic arc plasma jets in a larger domain.

Lusko et al. produced the longest timescale 2D PIC simulations of the down-channel discharge from a cathodic arc device under the influence of an axial magnetic field [22]. They modelled the ionisation of metal atoms ejected from the cathode and the Coulomb collisions of the ions with neutrals and vapour following the initial arc trigger. The high-frequency instabilities present in this model reflect those observed experimentally; however, the physical processes that generate these instabilities require further investigation [118]. The dynamics of spot generation at the cathode surface were not explored in their study, resulting in the omission of the highly collisional initial discharge state. Furthermore, multiple ion charge species were omitted, precluding the study of the effects of an applied axial magnetic field on the energy distributions of each charge state.

1.4.4 Simulation of magnetised RF plasma jets

The use of PIC simulation to characterise RF plasma sources can be split into two categories. The first is the electromagnetic simulation of the RF antenna and the interactions with gas propellant to create a plasma breakdown and maintain a discharge [129]. The computational requirements of the simulation of RF plasma breakdown and interaction are currently computationally prohibitive for optimisation of RF plasma thrusters with an MN, with successful demonstrations of RF breakdown simulation requiring three-dimensional EM simulations (at least one degree of freedom in position and three in velocity, 1D3V) due to the rotating fields involved [130, 131].

The second method of simulation concerns the interactions of the plasma discharge created by the oscillating RF field, with the externally applied magnetic field used to drive and direct the acceleration of charged particles. As discussed in Section 1.2.4, the diverging magnetic field applied to RF plasma sources such as thrusters forms a magnetic nozzle (MN). The MN converts low-energy thermal ions into a directed jet of high-energy kinetic ions, thus the design of the specific magnetic field topology that comprises the MN is a key issue when improving RF thruster performance. For this reason, the use of PIC simulation to characterise the effect of the MN on thruster performance has seen a recent increase in the investigation.

The earliest study using PIC simulation to investigate the effects of an MN on an RF plasma discharge is the 2002 work of Ilin et al. on the determination of ion detachment from the VASMIR thruster. The axisymmetric

electrostatic PIC model successfully predicted plasma density, plasma potential and ion energy throughout the plume, validated against experimental results on the VX-10 VASMIR thruster. By observing changes in axial ion energy, as well as the plasma β throughout the plume, they determined the ion detachment location given the VASMIR MN field topology and initial assumptions on generated plasma based on experimental data. An agreement between the condition $\beta > 1$ and the plateau in a test ion's axial energy predicted the ion detachment location. The study opened up the possibility of performing a parametric optimisation given future increases in computing power [132].

A hybrid PIC approach, with electrons behaving as a fluid, has been used by Cichocki et al. to perform simulations of an MN applied to a helicon RF thruster that was validated against experimental ion current data at a distance of 40 cm from the plasma source. The results supported the viability of a hybrid simulation for developing PIC models of similar discharges [133]. Further validation is needed to demonstrate the code used for a broader array of helicon thrusters, however, the study demonstrates a significant optimisation of helicon PIC models.

A fully-kinetic electrostatic PIC study of the magnetised mesothermal plasma jet from the USC micro-ion thruster was undertaken by Hu et al. successfully demonstrating the effects of an MN on microscopic plasma plume structure. The study concerned a micro-ion thruster, however effectively showed the prediction of ion and electron behaviour in a 2D3V PIC model of an MN [134]. More recently, Hu et al. have developed a fully-kinetic axisymmetric PIC model to characterise the effect of MN nozzles on propulsion performance more generally. The behaviour of an ECRT with a solenoid MN using collisionless PIC simulations (as compared to experimental data) was characterised, showing ion acceleration due to the plasma potential created by the MN and the drop in electron pressure as plasma expands through the diverging magnetic field [135]. The study supported the stance that the majority of plasma transport is due to electrostatic behaviour, as EM effects and collisions are omitted.

Research by Di Fede et al. has also demonstrated 2D3V electrostatic PIC simulations of the magnetically enhanced plasma thruster (MEPT), a type of helicon thruster. As the model uses the two-dimensional PIC software Starfish, their simulations are in 2D3v. In the study, both electrons and ions are treated as particles (fully kinetic) and are generated at a surface that is normal to the plume direction, sitting at the exit of an RF plasma source. The magnetic nozzle is generated using a solenoid with a peak magnetic flux density of 300G [136]. The model does not simulate particles inside the plasma source, omitting any effects of the initial electrostatic potential field and confining magnetic field in this region. The MEPT model was further developed into an axisymmetric simulation and was successfully bench-marked against experimental data on electron density and plasma potential profiles for a 50W MEPT [137]. Both studies analyse the effect of a solenoid MN with a relatively low peak magnetic field strength, and a deeper investigation of more unique MN topologies, and larger peak magnetic field strengths.

A similar PIC model was also recently demonstrated by Chen et al. for the investigation of ion acceleration mechanisms in an MN, and assuming an ambipolar discharge they found that two-thirds of the ion acceleration were attributed to electrothermal processes [34]. The remaining third was due to electromagnetic particle transport mechanisms such as diamagnetic drift (as emphasised by Merino and Ahedo et al. in Section 1.2.4), as well as $\vec{E} \times \vec{B}$ drift and other minor effects. They also found that electron thermal conversion to ion acceleration was not positively correlated with $|\vec{B}|$, with a decrease in conversion efficiency at larger values. The study has implications for optimisation efforts, considering the maximisation of $|\vec{B}|$ approach to increase helicon source density and thus thrust.

1.5 Inverse Design

Broadly put, inverse design is the iterative optimisation of a device to achieve the desired performance with minimal prior intuition about the ideal solution, leading to non-intuitive outcomes and a deep exploration of design spaces. The iterative process of inverse design is computationally expensive, especially when considering designs with many degrees of freedom, and so despite strategies using traditional optimisation strategies it has only recently gained momentum with improvements to computer processing speeds.

The application of inverse design to develop electromagnetic devices has gained recent attention, with the demonstration of the technique by Piggott et al. to create a demultiplexer that splits $1300nm$ and $1550nm$ electromagnetic radiation on a μm scale device [138]. They showed that a device that would originally require expertise and tuning by hand with only six degrees of freedom could be substantially improved on with an algorithm that explores a significantly greater design space, and thus can find a more optimal solution with little prior knowledge.

1.5.1 Metaheuristic optimisation

The goal of metaheuristic optimisation methods is not to find the ‘best’ solution to a design problem, but a sufficiency improved or close to ideal solution (where sufficient is defined by the user based on the context of a problem), thus it is the process of finding a heuristic. The algorithms used are stochastic and iterative, typically inspired by natural processes such as evolution or annealing. The lack of global solution requirement allows these methods to exceed standard analytical or gradient-based methods in terms of both speed and a larger exploration of possible solutions. Techniques can be sorted into single search and population-based methods, such as simulated annealing and evolutionary algorithms respectively.

Evolutionary algorithms have demonstrated promise in the optimisation of complex multi-objective design problems with no prior assumptions [139–141]. These algorithms have shown superiority over Gradient descent

optimisation and other metaheuristic methods such as simulated annealing for problems with many inputs, multiple objectives, and discontinuities. Generally, evolutionary algorithms iterate over the steps outlined in Figure 1.8 until a pre-defined objective function threshold is met [141, 142].

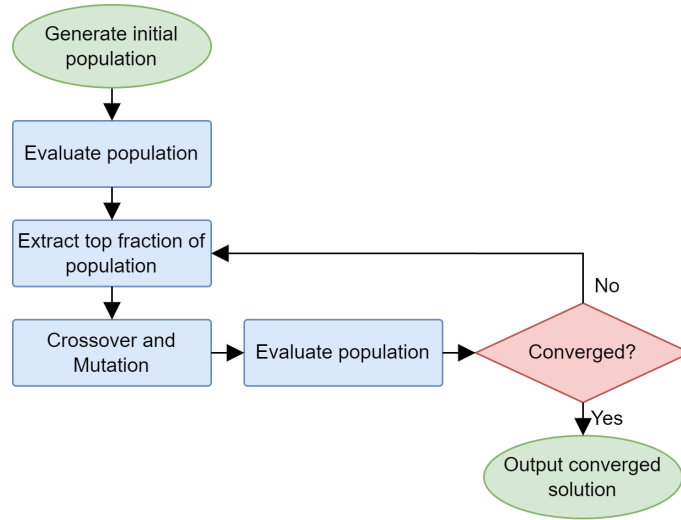


FIGURE 1.8: Flowchart overview of the iterative evolutionary algorithm process from an initial population sample to a converged solution.

The key steps within the flowchart in Figure 1.8 are the mutation, crossover, and population evaluation with an objective function. The mutation is typically a random addition or reduction to a population member, such as a binary flip of an element of the array. The crossover of two promising configurations consists of the swapping and combination of the characteristics of two separate members. If implemented correctly, these two methods of searching the solution space led to convergence on an optimised solution [142]. Each member of the population is evaluated by its resulting difference to an ideal solution, and the function used to implement this mathematically is known as the objective function. Objective functions need to be tuned to ensure the algorithm can converge on an ideal solution, given an efficient search of the solution space. It is critical to define an objective function that does not converge on edge case solutions that do not fit optimisation goals. For problems in physics and engineering, objective functions will incorporate the behaviour of physical quantities such as electromagnetic fields and heat [141].

Genetic algorithms, a subset of evolutionary algorithms, were applied by Cheng et al. as an approach for optimising the configuration of permanent magnets to develop a magnetic field topology that improved the efficiency of a magnetic refrigerator [143]. The genetic algorithms method selected random traits from successful members of a previous population to generate a new population rather than use the standard parent-child approach. Following a convergence, the discrete regions of magnetic material were refined, and the process was repeated, allowing for solutions with high granularity.

1.5.2 Inverse design of magnetic circuits

The increases in available computing power are accelerating the use of topology optimisation techniques to arrange electromagnets or magnetic material in a lightweight configuration that produces an optimal field topology. Inverse design of field topologies can be utilised to leverage plasma phenomena such as magnetic mirroring to improve unidirectional plasma flow or ensure ions leave the thruster region so that they impart momentum to the spacecraft.

Improved magnetic field topologies are challenging to determine analytically and the potentially complex geometries require additive manufacturing processes to be constructed. Broadly put, inverse design is the iterative optimisation of a device with minimal prior intuition about the ideal solution, leading to non-intuitive outcomes and a deep exploration of design spaces. Inverse design techniques including machine learning and metaheuristic methods (Deep learning and Genetic algorithms respectively) have successfully been applied to the optimisation of magnetic devices such as those used in magnetic fusion, Magnetic Resonance Imaging, and magnetic refrigeration, as well as demonstrations on Hall effect propulsion devices [143–146].

Optimisation of magnetic fields can be performed with both electromagnets and permanent magnets. Given the ability of permanent magnets to retain a substantial magnetisation within the lifetime of any propulsion device's use, the complexity and energy requirements of devices optimised with these magnets can be reduced for convenient application in small spacecraft propulsion systems [53, 147]. Magnet geometries can also be optimised for minimisation of mass and volume, as well as conformity to specific dimensional constraints, a crucial application when considering the stringent design margins associated with spacecraft subsystems.

1.5.3 Inverse design of Electric propulsion systems

Previous designs for RF propulsion systems such as VASMIR have used an analytical trial and error approach combined with magnetostatic simulation to design a magnetic circuit configuration that produces a field topology that can efficiently propagate an ambipolar discharge. Attempts to produce analytical solutions for permanent magnet arrays can suffer from an inaccurate representation of nonlinear effects and self-magnetisation [87].

Success in treating the optimisation of a Hall effect thruster as an inverse design problem and applying gradient descent methods to find a solution has been shown by Sanogo et al. They considered the manipulation of a magnetic circuit to find a topology that improved Hall current to optimise ionisation efficiency. The solution space was formulated as a distribution of ferromagnetic material within the magnetic field applied by the coils. The applied objective function was the error between the simulated and desired magnetic vector potential at a series of measurement locations for each iteration. The Hall effect thruster design was optimised using the Solid Isotropic Material with Penalisation (SIMP) approach, whereby ferromagnetic material exists as a continuous

relative density distribution that converges to a binary solution, and therefore a physical design (regions of either no material (0) or all material (1)) [90, 148]. While this technique seemed effective and found an optimised design, there was no validation performed using experimentation or simulation, and given the use of a gradient descent algorithm, there may have been a convergence to a local solution, potentially a result of the algorithm's inability to account for discontinuities in the solution space. Furthermore, the algorithm's applicability for permanent magnet configurations instead of initially unmagnetised ferromagnetic material was mentioned but not explored. More recently Adjoint Topology Optimisation has also been applied to Hall Effect thruster magnetic circuit design, but this demonstration also requires performance verification and validation [147].

There have been efforts to directly optimise the magnet configurations for a cusped-field thruster (HEMP-T) using evolutionary optimisation and surrogate modelling. These studies demonstrated improvements in thrust performance and reductions in weight over competing systems, further demonstrating the growing utility of the metaheuristic design of plasma propulsion devices. While the studies by Yeo et al and Fahey et al. successfully demonstrate the viability of this strategy, the optimisation methods used are low fidelity and concern the geometry of only a few magnets (a small input space, due to the cusped field thruster geometry) [139, 144].

1.6 Thesis overview

The thesis is structured to begin with a broad introduction to the concepts required to understand the physics and motivations behind the work undertaken in Chapters 2 to 4. The first chapter includes a review of the current state of electric propulsion, including the complexities associated with the development of RF propulsion systems such as the function of magnetic nozzles. Additionally, the use of PIC simulation to simulate plasma is discussed in detail, along with a review of the application of PIC to simulate the magnetised electrostatic plasmas that are explored throughout the thesis. Finally, the growing utility of inverse design to solve complex problems in electrodynamics is covered, together with the process of optimisation with an evolutionary algorithm, as used to solve magnetostatic design problems.

Material within the second chapter was published in the journal of Plasma Sources Science and Technology and concerns the PIC simulation and analysis of the physics involved in cathodic arc plasmas [149]. Content within the second chapter demonstrates the validity of the use of an axisymmetric and electrostatic PIC simulation model to explore complex plasma phenomena in both unmagnetised and magnetised modes of cathodic arc operation. In addition to providing new insights, and conforming to existing theories about cathodic Arc behaviour, a comparison of simulation results to previous experimental data solidified the use of the PIC software and model assumptions to analyse the magnetised RF discharges in the latter chapters.

Development of two variants of an RF propulsion system using permanent magnets is covered in the third chapter, and includes research presented at the 68th and 70th International Astronautical Congresses, as well

as the 17th Australian Space Research Conference. The primary novelty of this study is the use of a Monte Carlo sampling method to develop the required annular magnet geometries to produce a desirable magnetic field topology for an RF plasma source. The final design was also modified to include the novel use of a μ metal magnetic shield to further modify the field topology, resulting in the creation of two design variants. In addition, the study includes PIC models of both design variants to explore the ion and electron behaviour in each, providing further insights into the physics of magnetised plasma. The PIC models were validated against experimental results of density and ion energy for each constructed design variant with a helicon plasma source, further validating the electrostatic PIC method explored in the thesis.

The fourth chapter is a culmination of the research so far, exploring the use of an evolutionary algorithm to optimise a complex geometric array of cubic permanent magnets to produce a magnetic field topology with few prior assumptions. The chapter also comprises a paper, undergoing review. The methodology presented in chapter three is a novel application of a metaheuristic strategy for the optimisation of an RF propulsion system. The core of PIC models that have been validated in the preceding chapters is also used to confirm a positive correlation between the objective function of the optimisation strategy and simulated thrust. Both the method used to design the magnetic field geometries and the PIC models of an RF thruster than uses them to magnetise the plasma jet is validated against the density and ion energy plasma diagnostic for two designs constructed using additive manufacturing.

Kinetic Simulation of a Cathodic Arc

2.1 Introduction

A cathodic arc is an electrical discharge consisting of a localised region of hot plasma on a cathode surface, called a cathode spot, that streams towards a passive anode. Cathodic arcs produce highly ionised metallic plasmas useful for thin-film deposition [18] and electric propulsion [150]. The dynamics of cathodic arcs is an active area of research, in part due to the fractal-like propagation of transient micro-scale cathode spots. The initial generation of metal plasma occurs when the cathode spots rapidly heat up, ablate, and ionise the cathode surface material. There is a direct correlation between the properties of cathode spots and those of the resulting collimated plasma discharge as the arc progresses [18, 20].

In this study, existing experimental and analytical derivations are used to build a fully kinetic simulation model, with no fluid species, of a cathodic arc discharge. The Miniature Arc Gun apparatus was selected for modelling and direct comparison with published experimental results of ion energy distributions for different charge states [116]. The computational model includes a simplified axisymmetric geometry and repetitive spot generation on the cathode surface, to better understand the resulting ion energies for different charge states and materials. The key developments include the simulation of the full source-to-substrate length scale and the evolution of a continuous injection of spot emissions into a plasma jet. Electrons are treated as particles, as are the ions, and thus the effects of escaping energetic electrons such as the development of ambipolar electric fields and super-thermal particles can be captured. Additionally, the model includes applied magnetic fields to explore the acceleration mechanisms driving the resulting increase in ion energies.

Amongst the prior experimental work used is that of Ryves et al. and Meysyats et al. for determining spot frequencies using burning voltage noise spectra [151, 152]. The simulation of plasma dynamics present in the late spot expansion and the interaction between the plasmas of successive spots can in turn address the origin of noise in the arc current. Analytical and experimental results from Anders et al. concerning ion energies and derived spot densities at the Saha freezing point are also used to tune the model parameters [18]. Furthermore, by resolving the plasma parameters close to the cathode surface through simulation, the relevance of the potential

hump theory for ion acceleration [117] is numerically evaluated, including the relative acceleration of different ion charge states [116].

The numerical model presented here can be used to probe the plasma dynamics of cathodic arcs early in the life of the discharge, which is of specific interest when considering elevated plasma temperatures [20, 24]. With the modification of the input parameters, the performance of most cathodic arc devices can be explored in the collisionless regime with more granularity than is currently possible through experimentation. The model input and output parameters were benchmarked against all relevant experimental and theoretical observations to confirm the validity of the model.

2.2 Model description

The overall model can be summarised as an axisymmetric, electrostatic, and fully kinetic 2D3V (two degrees of freedom in position and 3 in velocity) particle-in-cell simulation. The core assumption of the model is that the system geometry, and the geometry of the dynamics and evolution, can be approximated as axisymmetric. Simulations are performed using the VSim 11 software package developed by Tech-X. The PIC process used is covered in detail in Section 1.4.1.

The experimental apparatus selected for modelling was the arc miniature gun used in the research of Zohrer et al. [116]. This allows for a direct experimental comparison of the ion energy distributions for the selected cathode materials, *Nb* and *Al* [116]. The results from the Mevva V ion source with an applied magnetic field used by Anders et al. were used to further validate the results in the case when an axial magnetic field was applied [24].

2.2.1 Cathodic arc model

A simplified characterisation of the time evolution of a cathodic arc was developed to perform an accurate simulation with the available computational resources. Given that the model is concerned with the generation of multiple cathode spots, the size and density of spots require careful definition. Spot size is still an area of research, as there have been differing approximations using crater size and brightness intensity [118, 153]. The largest distribution of crater sizes demonstrated by Juttner et al. has a mode of $10\mu m$ in radius. This is in contrast with the leptokurtic spot brightness results spanning $0 - 100\mu m$ by Siemroth et al. [154], who asserted that sub-spots are in the bright peak of these distributions. These results support an upper bound for sub-spot sizes of $10\mu m$ radius which is in line with the characterisation of sub-spots in crater data. For convenience, in our model a sub-spot, also known as a spot cell or fragment, is defined as a spot.

The geometry of each spot is limited by cell width within the simulation grid. Spot density was thus extrapolated by scaling the volume of experimental determinations of the cathode spot sub-cell length ($10\mu m$ radius) to the

annular volume about $r = 0$ created by each 1mm^2 cell, within which spots are initialised in the axisymmetric simulation. As a result, particles are generated past the Saha freezing point, the point in a spot's lifetime beyond which ion charge states are effectively fixed [18]. This size is reasonable when considering the order of atomic spacing ($< 1\text{nm}$) prior to the spot explosion.

Prior analytical and experimental research by Anders et al. indicated an electron temperature of 3.1eV for Al and an ion number density of $1.4 \times 10^{25}\text{m}^{-3}$ at the Saha freezing point [18]. In the current work, the simulated time of spot expansion begins at a spot volume of $10 - 20\text{mm}^3$, corresponding to an extrapolated peak density of $5.8 \times 10^{18}\text{m}^{-3}$ (Figure 2.1). The initial ion temperature at the Saha freezing point is not measured experimentally, and stationary ion injection would not reflect the high potential energy experienced in a cathode spot. Therefore, ions were injected using a Maxwell-Boltzmann distribution with a v_{rms} equivalent to the local sound speed, assuming that the ions and electrons are in thermal equilibrium [119].

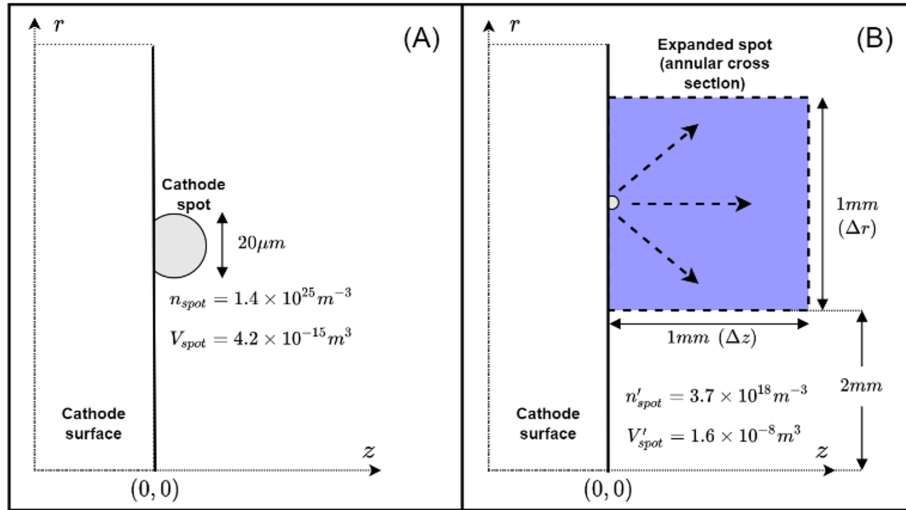


FIGURE 2.1: Diagram showing the process of spot initialisation using an initial assumption of spot density n_{spot} (A) to extrapolate simulated starting spot density n'_{spot} within a simulation cell (B).

The period of spot generation is set to 16ns , motivated by observations of cyclical variations of arc voltage noise spectra in prior experimental work, including Meysyats et al. and Ryves et al. [151, 152]. These independent experimental results confirm the existence of frequency peaks between 10MHz and 100MHz superposed on power-law noise spectra. We attribute the spectral peak to sub-spot generation. The simulation assumes creation of a spot periodically every 16ns for simplicity based on the aforementioned trend in the noise spectra [151, 152, 155].

To conform to axisymmetric symmetry, as required by our model, each spot is an annulus. This is supported by experimental results showing that the fractal propagation of spots toward the anode approximates a ring of

subdividing spots centred on the cathode axis [25, 118]. The total energy and charge density of these spots is proportional to the arc current, so the ring of subdivided spots at radius R_s at time τ in Figure 2.2 can be defined as a single annular spot with equivalent charge density.

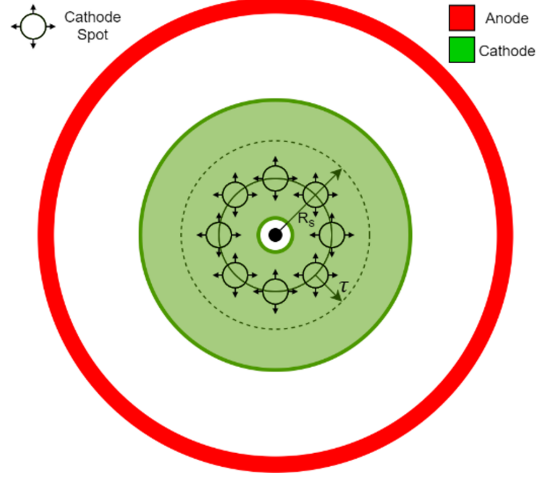


FIGURE 2.2: Annular simplification of fractal spot propagation showing radius R_s for each spot generation period τ .

The system is modelled on the design parameters of the Miniature Arc Gun and associated apparatus used in the experimental work of Zohrer et al. [116], as this work offered a direct experimental comparison when investigating the charge state energies of cathodic arcs [116]. The model uses the axisymmetric geometry between the cathode surface and the pinhole filter situated at the fore of the detector, as shown in Figure 2.3.

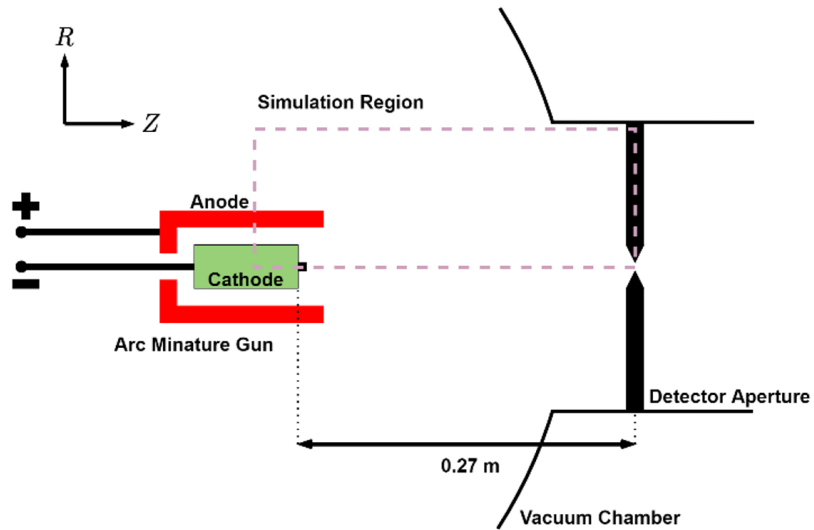


FIGURE 2.3: Miniature Arc Gun experimental apparatus showing the locations of the cathode (green), anode (red), the simulation region, and the location of the pinhole detector aperture.

As outlined earlier, the Miniature Arc Gun apparatus was selected to evaluate the effectiveness of the numerical model in simulating the relative ion energy distributions for different charge states. The resulting simplified model configuration and simulation domain boundaries are shown in Figure 2.4.

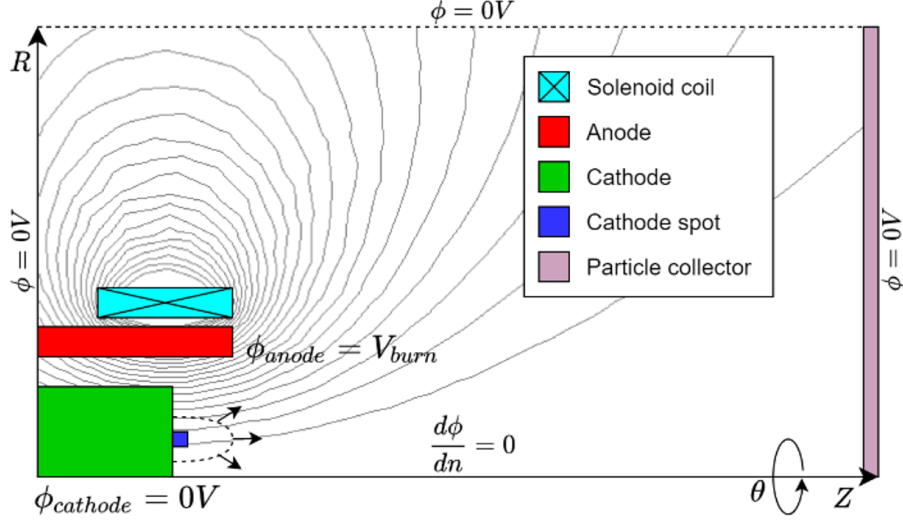


FIGURE 2.4: Cathodic Arc PIC model setup showing electrostatic boundary conditions and an applied magnetic field (black flux lines).

The simulation model domain boundaries are Dirichlet boundaries at a fixed potential of $0V$, representative of an encompassing vacuum chamber with a collection plate in the path of the plasma jet. The cathode and anode are at fixed potentials of $0V$ and V_{burn} respectively for simplicity. The burn voltage V_{burn} and charge state distributions are set to the characteristic values of each cathode element, taken from previous experimental work by Zohrer et al. and Anders et al. [18, 116]. In detail, these previous experiments grounded the anode rather than the cathode and the effect of this difference is addressed explicitly at the end of Section 2.3.1 below. There it is demonstrated that there are minimal changes within the uncertainties of the datasets.

To maximise the statistical information collected on the ion energies, the aperture detector was substituted with a planar collector at the right-hand side of Figure 2.4. To ensure that the results were equivalent to those collected by the aperture in the experimental apparatus, only the z -component v_z of each ion velocity is considered below (put another way, the radial velocity v_r of each incident ion is not analysed).

2.2.2 Modelling the effect of an applied magnetic field

To predict the experimental effect of an applied magnetic field, a solenoid of fixed current was simulated using FEMM, and the corresponding fields are included in the simulation, as shown by the magnetic flux lines in Figure 2.4. The field strength can be adjusted using either a fixed or pulsed power supply. For this research,

a fixed-current solenoid was used, to ensure that the axial field strength is constant in the simulation and is consistent in magnitude with the experiment. The field strength is measured at the cathode surface, coinciding with the midplane of the solenoid.

Due to its direction, the applied magnetic field acts as an insulator in the sense that it impedes electron propagation from the cathode to the anode. Theoretically, this is expected to increase the burn voltage and shift the charge state distributions of the spot plasma. Experimental results from Oks et al. confirm changes in charge state fractions for different elements and suggest fixed values to be used in the simulations below for an axial magnetic field of 1.2 T [119]. The burn voltage values are adjusted using the Mevva V source experimental results of Anders et al. [24] for different applied fields and cathode materials.

2.2.3 Model accuracy

The primary concern for model accuracy is that the simulation parameters and grid are appropriate for the modelled discharge. The peak theoretical density determined in section 2.2 of $5.8 \times 10^{18} m^{-3}$ translates to a Debye length λ_D of approximately $5.4 \times 10^{-6} m$. The grid width required to minimise numerical heating is then $\Delta x = \pi \lambda_D \cong 17 \mu m$ [156].

The large length scale of the models, where $L \cong 0.5 m \gg \lambda_D$, necessitated the use of self-similarity scaling to prevent unrealistic computational requirements. This process can improve PIC runtimes by many orders of magnitude, while maintaining accurate representations of plasma discharges. To achieve this model parameters such as potential, length, and density are scaled relative to a factor ζ to retain accurate plasma dynamics. Scaling was performed using the unscaled potential method presented by Tacconga et al. with a ζ of 0.01 [109]. Using this scheme, the length, current, and mass flow rate are multiplied by ζ , whereas density, electric field, and magnetic field are multiplied by ζ^{-1} . In this case, the velocity and potential remain unscaled. The required grid spacing was inflated to $10 \mu m$ ($1 mm$ unscaled), with the acknowledgement that localised numerical heating would occur if the ion or electron number density exceeds $1 \times 10^{19} m^{-3}$, since the associated Debye lengths would violate the grid spacing condition outlined above. Effects from this inflation were not observed to impact results in initial test simulations of similar dynamics; this is due to the simulation having typical peak mean number densities of approximately $1 \times 10^{17} m^{-3}$ in the anode mouth region, so that numerical heating is not expected from the self-similarity scaling.

To accurately simulate plasma dynamics, the number of real particles in a super-particle must be tuned such that each cell in a region of interest contains a suitably large effective number of super-particles at each time step. In our models, the rule of thumb used was at least five particles per cell in the region between the cathode surface and the anode mouth. Values exceeding this limit created a negligible change in results at the cost of a quadratic scaling in computer time.

The time-resolution limit is dictated by the electron gyrofrequency when a magnetic field is applied. Given that the Buneman-Boris particle push method is used, the required timestep size follows the inequality [109].

$$\Delta t < \frac{0.35m_e}{q_e B_\perp} \quad (2.1)$$

Assuming an upper bound for B (and by extension B_\perp) of 0.5 T, the timestep was set to $1 \times 10^{-11} s$ for consistency. When coupled with the self-similarity scaling used, the timestep is reduced to $1 \times 10^{-13} s$. Alternatively, given that we are also considering plasmas without an applied field, the plasma frequency is used to constrain the time step via,

$$\Delta t \leq \omega_p^{-1} \quad (2.2)$$

The plasma frequency for the density determined in Section 2.3.1 is $7.7 \times 10^{10} Hz$. Therefore, the timestep remains set to $1 \times 10^{-11} s$.

2.3 Results and Discussion

The VSim particle-in-cell simulation model produced the spatial, velocity, and energy distributions of the particles and the corresponding electrostatic potential field data at multiple times after the first pulse is initiated (the time origin). This paper presents these data and related parameters of interest, such as the ion number density n_i in Figure 2.5, at a time of $15 \mu s$. These simulations are performed for both unmagnetised and magnetised domains, and for several different cathode materials (and thus plasma ions). Additionally, time-series data on particles incident on the simulation boundaries were collected to calculate the energy distributions. Since a focus of this study is to validate the simulation results against observational data, a future study will address the physics and temporal development of multiple subsequent cathode spots into the plume plasma.

As discussed in the methodology (Section 2.2.1), the input parameters for the models were taken from prior experimental data as well as prior theoretical calculations [18, 24, 116, 119]. The parameters used in the simulation models are listed in Table 2.1.

2.3.1 Results for the Miniature Arc Gun

The number density distribution of Al ions shown in Figure 2.5 offers immediate insight into the simulated behaviour of the plasma ejected by the Miniature Arc Gun. The results show that the plume density is maximised along the domain axis ($r = 0$), and that the Al ions start diverging radially once they leave the $30mm$ diameter

TABLE 2.1: Simulation model parameters for *Al* and *Nb* cathode materials, and the Al cathode with an applied magnetic field.

Cathode material	Al		Nb
Solenoid current (A)	0	300	0
Burn voltage (V)	23.6	60	27
1+ ion fraction	0.38	0.05	0
2+ ion fraction	0.51	0.11	0.194
3+ ion fraction	0.11	0.84	0.608
4+ ion fraction	0	0	0.198
Te (eV)	3.1	5	4

anode mouth that extends axially past the cathode working surface by 16mm . The absolute peak density of $1 \times 10^{18}\text{m}^{-3}$ is located at the cathode spot, 1mm off the cathode surface and 2.5mm from the domain axis. A backflow of ions is observed (see the ions at $z < 0$ between the anode and cathode), occurring from the cathode working surface to the side of the cylindrical cathode. Additionally, ions are incident on the anode surface, being absorbed in the process.

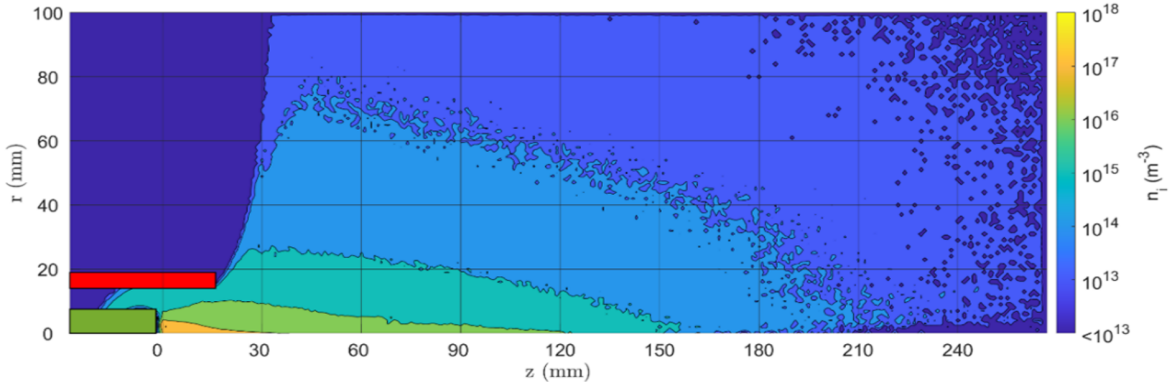


FIGURE 2.5: *Al* ion number density n_i distribution in axisymmetric (r, z) coordinates $15\mu\text{s}$ from the pulse start for the unmagnetised simulation with the anode and cathode shown in red and green, respectively.

The velocities of *Nb* or *Al* ions incident on the rightmost boundary of the simulation domain were processed to produce kernel density estimates of the probability distribution functions of the normal velocity component (v_z) exiting the domain. These normalised probability distributions (obtained by normalising Zohrer et al. data from ion flux as a function of speed to ion probability distribution functions of speed, such that their total integrals are unity) for each ion charge state, and for each cathode material are compared in Figure 2.6 with experimental results from the arc miniature gun at $15\mu\text{s}$ from the start of the pulse [116].

The locations of the peaks in the distribution functions in Figure 2.6 can be quantitatively compared. There is good agreement between the observed and simulated values of v_z . Specifically, the peak values differ only by between 1.6% (for Nb^{3+}) and 10% (Al^{2+}). Thus, the simulation results for peak v_z match the experimental

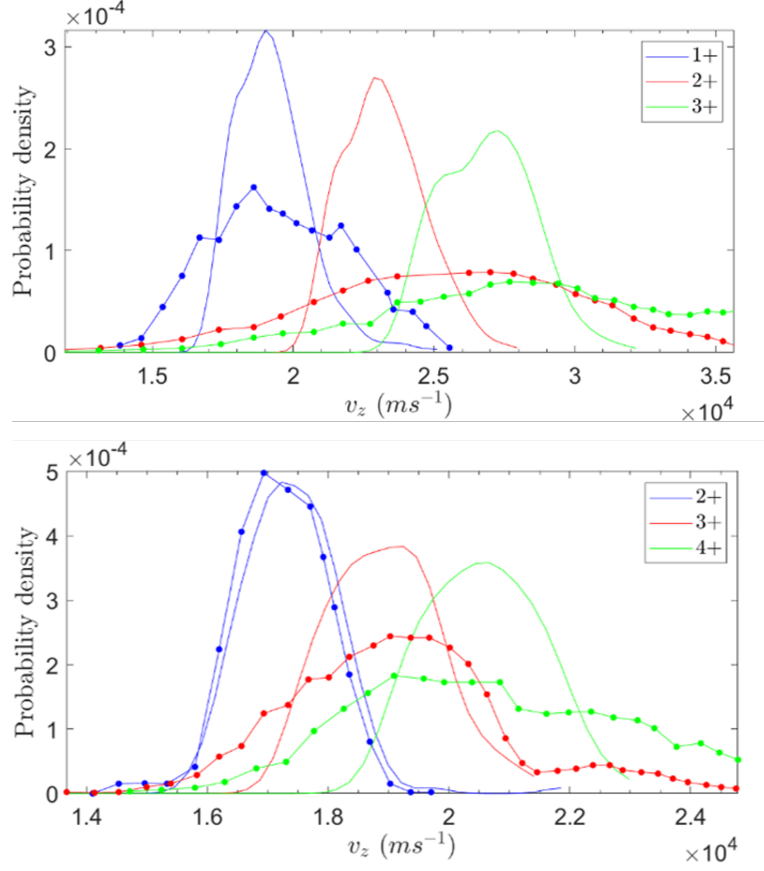


FIGURE 2.6: Simulated ion velocity (v_z) distributions (solid lines) and corresponding experimental results at $15\mu s$ (dotted lines) for *Al* (top) and *Nb* (bottom)[116].

results within the error margins ($\pm 1 \times 10^3 m s^{-1}$). Notably, the *Nb* distributions for each charge state exhibit a singular peak, consistent with the experimental data. The Nb^{2+} simulation data is of particular interest, as it fits the experimental results almost exactly. Detailed numbers for the peak ion axial velocity (v_z) and kinetic energy (E_k) in the far-plume region for both *Al* and *Nb* cathode working materials are summarised in Table 2.2, showing good agreement between the experimental and simulation results.

TABLE 2.2: Distribution parameters of ion axial velocity data from experiment (v_{zpeak}^*) and simulation (v_{zpeak}) for various charge states.

Cathode material	Z_i	v_{zpeak}^* ($\times 10^4 m s^{-1}$)	v_{zpeak} ($\times 10^4 m s^{-1}$)	$E_{kpeak}(eV)$
Al	1+	1.86	1.90	64
Al	2+	2.53	2.29	83
Al	3+	2.77	2.73	114
Nb	2+	1.69	1.72	154
Nb	3+	1.93	1.90	186
Nb	4+	1.99	2.06	223

It is apparent, however, that apart from the Nb^{2+} ions, the experimental distributions in Figure 2.6 are much more dispersed in v_z (to both smaller and larger values), and thus flatter than the simulated distributions. We note a smaller spread in v_z for the simulated distributions for all Al ion charge states as well as for the Nb^{3+} and Nb^{4+} ions in Figure 2.6. In Section 2.2.1, we propose features of the simulation, as compared to experimental data, that produce the discrepancy in the ion velocity spread.

The primary contributor to the high ion speeds along the z axis, and the physical origin of the associated ion acceleration presented in Figure 2.6, is the gradient in the steady-state electrostatic potential field along the z axis in the simulation domain (Figure 2.7). The spatially varying potential results from the potential difference between the anode and cathode, and the creation, evolution of the cathode spots, and the resulting plasma that expands into the simulation domain. The contour plot in Figure 2.7 shows a peak potential of 30V in the cathode spot generation cell. The large-scale electric field causes the density distribution shown in Figure 2.5 as ions accelerate along the radial potential gradient.

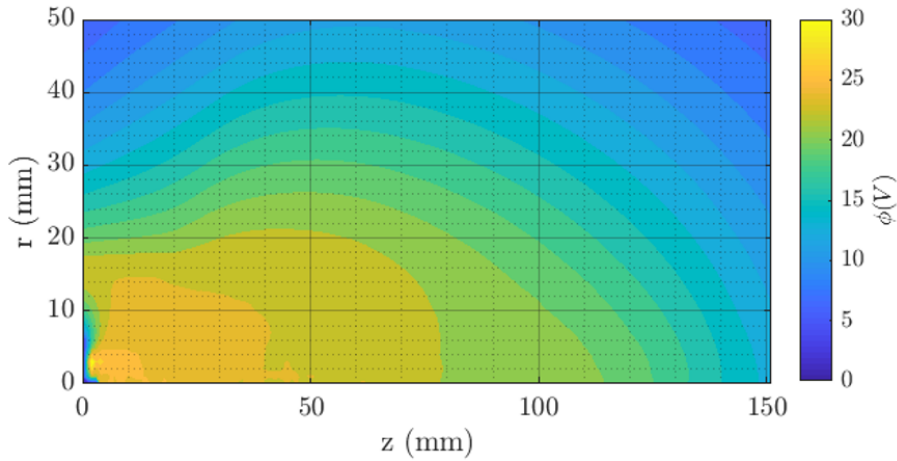


FIGURE 2.7: Electrostatic potential field of the simulated unmagnetised (Al) cathodic arc plasma jet at $15\mu s$.

The analysis in Figure 2.9 explores the ion behaviour by analysing the kinetic energy $E_k(r, z)$ of each ion super-particle as a function of z . The distributions of E_k for each charge state clearly vary significantly with z . For $30 < z < 150mm$, the distributions are very broad, but they become increasingly narrow as z increases above approximately $150mm$. This evolution may be partly due to differences in the electric potential with r for a given z , but a simple potential model would tend to preserve the range of E_k as a function of z . Alternatively, since the range of E_k at a given (r, z) depends on the particle distribution function, it is possible that wave-particle interactions act to vary the range of E_k with z .

Related to these points, Figure 2.9 shows that although there is an approximately linear relationship between the mean kinetic energy and z , it is not solely a matter of the electric potential. This is apparent because the kinetic

energies at a given z location are not in the ratio 1 : 2 : 3 for the three charge states, 1+ to 3+, as can be seen by comparing the mean kinetic energies at each z . Deviations of kinetic energy from those predicted by the change in electrostatic potential over the ion trajectories occur for ions with both large and small kinetic energies. The degree of deviation in kinetic energy seems to be influenced by the ion locations in the simulation domain at the timestep being analysed ($15\mu s$). This is expected as the electrostatic potential exhibits both spatial and temporal variations throughout the domain. In this purely electrostatic simulation, the temporal variations in potential are likely due to a non-steady-state simulation and electrostatic wave-particle interactions, with plausible wave modes being ion/electron cyclotron, ion/electron plasma, and upper hybrid waves. Starting potential remained relatively static over the course of the unmagnetised simulation, ruling out inflated ion energies due to greater starting potentials that were not accounted for (Figure 2.8).

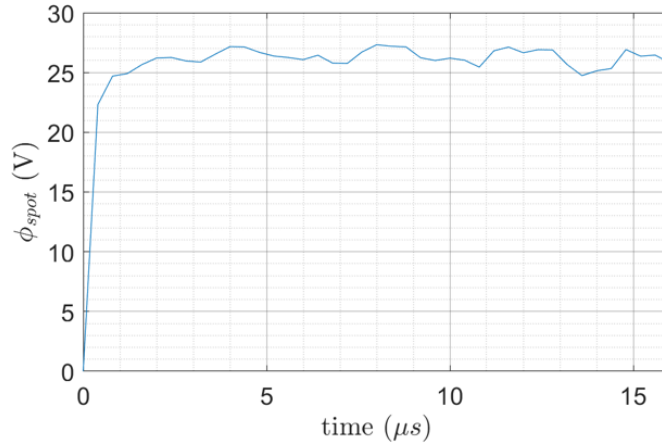


FIGURE 2.8: Electrostatic potential at the spatial location of the cathode spot over time (unmagnetised).

The results in Figure 2.9 show that the ion kinetic energies $E_k(z)$ are not proportional to the charge state of Al ions is also found for the Nb cathode (not shown), suggesting that it is a general phenomenon. Moreover, crucially, these findings match the experimental observations of Zohrer et al. for their Miniature Arc Gun [116].

This is further explored in Figure 2.10 by comparing the ion kinetic energy E_k with the product of the charge state and the difference $|\phi_i - \phi_0|$ in the potential between the measured ion location and the potential at the cathode spot at $15\mu s$. The results show a linear increase in the mean E_k with increasing potential difference for most ion locations. However, there are non-linear changes in the mean E_k at high and low potential differences. The study by Hohenbild et al. on axial changes in vacuum arc ion velocities also demonstrates acceleration of Al ions at a distance greater than $150mm$ from the cathode, further supporting this analysis [157].

Crucially, the results for the three charge states considered do not collapse onto a single line in Figure 2.10, demonstrating a dependence on charge state. Interestingly, at a given mean $Z_i|\phi_i - \phi_0|$ the mean E_k is larger for than that for $Z_i = 1+$ than for $2+$ which is larger in turn than that for $Z_i = 3+$. Moreover, the red line

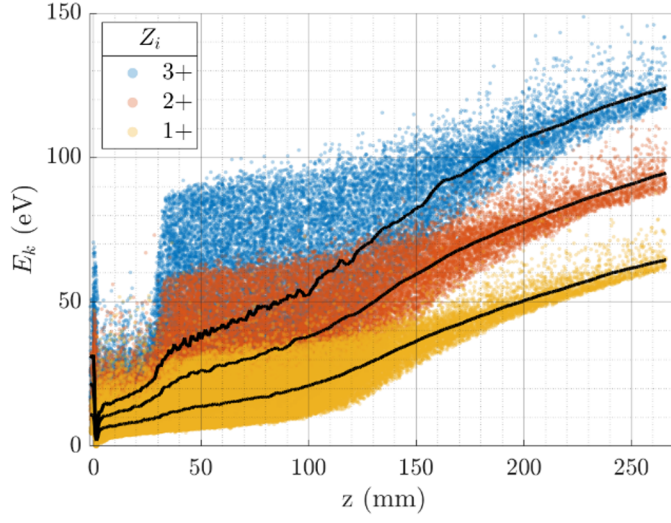


FIGURE 2.9: Phase-space plots of Al ion kinetic energy (E_k) and axial displacement from the cathode surface (coloured by Z_i). Mean values shown in black.

for $E_k = Z_i|\phi_i - \phi_0|$ shows that $Z_i = 1+$ is close to a state in which the kinetic energy equals the change in electric potential, whereas the curves for the higher charge states are increasingly below the line of equivalence for increasing Z_i . Put another way, the higher charge state ions have less E_k than expected from the electric potential drop they have fallen through. The missing energy may go into waves and the $Z_i = 1+$ ions, with the larger E_k at larger $|\phi_i - \phi_0|$ and larger z consistent with absorption of wave energy at larger z near the edges of the simulation domain. Conversely, energy may be gained through waves in cases when the mean ion energy for a specific charge state trends higher than the red line of equivalence.

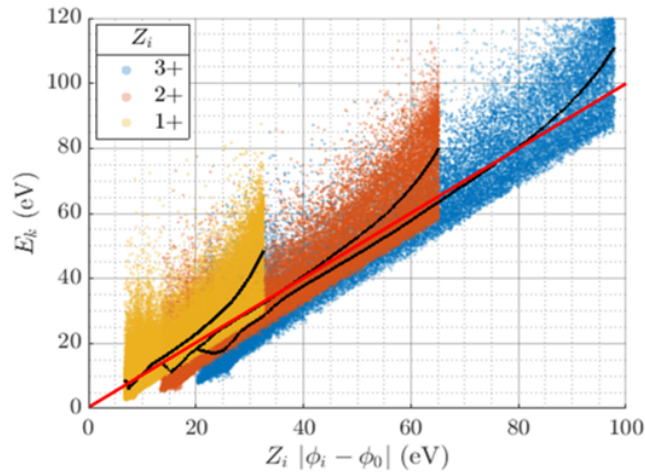


FIGURE 2.10: Plots of Al ion kinetic energy against the product of charge state and potential for all three unmagnetised simulated charge states. The mean trends are shown in black. The red line indicates the function $E_k = Z_i|\phi_i - \phi_0|$.

Figure 2.11 shows the results for $z < 10\text{mm}$, close to the cathode spot (near $z = 1.6\text{mm}$) and the start of the acceleration region at a larger z . The final mean ion energies when the ions flow backwards into the cathode surface near $z = 0$ are 11, 21, and 31eV for the Al^{1+} , Al^{2+} , and Al^{3+} ions, respectively. This is proportional to Z_i for a change in potential near 10V . However, at $z > 3\text{cm}$, Figure 2.11 shows clearly that the mean E_k is less than $Z_i|\phi_i - \phi_0|$ for $Z_i = 2+$ and $3+$, thus this decoupling effect starts at the beginning of the acceleration region.

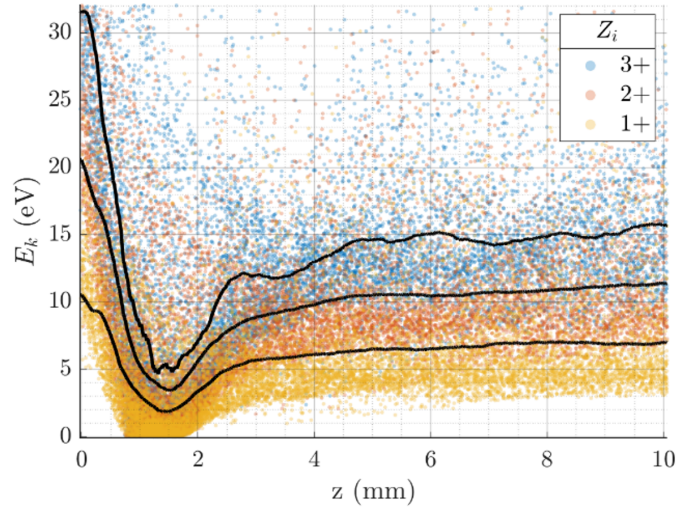


FIGURE 2.11: Phase-space plots of Al ion kinetic energy (E_k) and axial displacement from the cathode surface within 10mm (coloured by Z_i). Mean values shown in black.

A possible mechanism to the observed ion charge state energy coupling effect is the process of ion friction, demonstrated analytically by Krasov et al. [158]. Their analysis used a single-fluid hydrodynamic model to investigate the ion attenuation of different charge stages through Coulomb collisions, in contrast to our fully kinetic and collisionless model that omits Coulomb collisions. Our simulations present some evidence that this friction is due to instabilities (such as wave-particle interactions) present in the acceleration region, starting less than 5cm from the cathode surface and extending to a large z , as indicated by the regions of fluctuating density the axial phase-space between $z = 3\text{mm}$ and 25mm , as shown in Figure 2.12. This suggests that the decoupling effect occurs as the ions propagate away from the cathode surface.

The mean electron temperature moving axially from the cathode surface was measured and found to be almost constant as a function of z (Figure 2.13). There is weak evidence for a small increase of $< 20\%$ with increasing z with fluctuations between approximately 0.7 and 1.4eV . This shows a minimal change in the energy exchange between the ions propagating axially from the cathode and electrons.

It is of noteworthy that electrons are initialised in the simulation with a temperature of 3.1eV (Maxwell-Boltzmann). The lower mean temperature observed is a result of the loss of fast electrons to the anode, cathode,

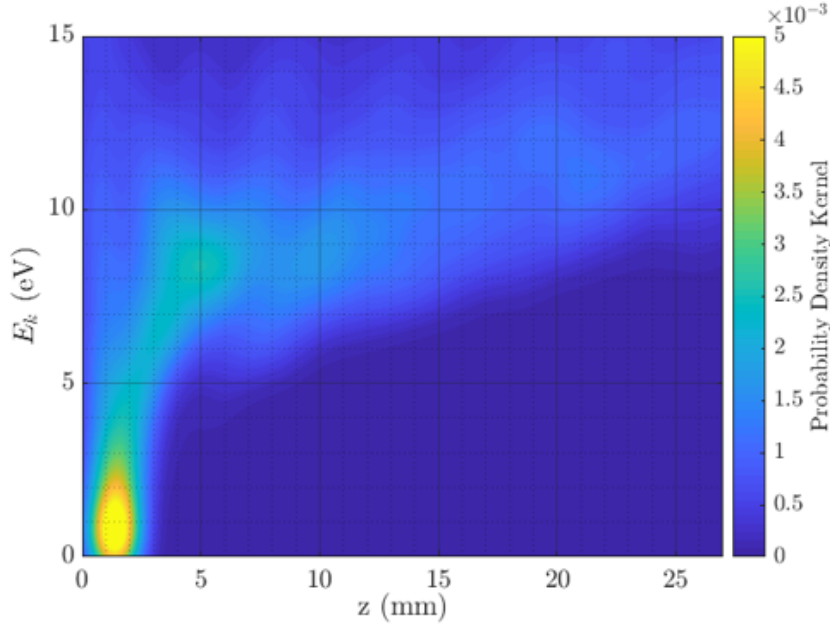


FIGURE 2.12: Unmagnetised Al^{2+} ion axial phase-space density plot $15\mu s$ from pulse start, colorised by particle probability density kernel.

to propagation out of the simulation domain, and ejection from the plume, whereas relatively slow electrons are trapped in the region of high potential close to the cathode.

The relatively constant electron temperature found is consistent with the assertion of the potential hump theory that ion acceleration is primarily attributed to the potential drop from the cathode spot, as shown for this case in Figure 2.7 [18]. This almost constant electron temperature profile is a constraint on the electrostatic wave-particle interactions suggested above, as indicated in Figure 2.12, since these must almost exclusively involve the ions and result in minimal electron heating.

2.3.2 Evaluation of the Miniature Arc Gun results

It can be observed in Figure 2.6 that while both the experimental and simulated results show an increase in the distribution spread with larger charge states, the spread in the experimental data is significantly more pronounced for both smaller and larger v_z . The simulations yield approximately Maxwellian distributions in v_z for the ions (Figure 2.6), as also assumed for the initial ion and electron distributions leaving the cathode spot, and the resulting peaks closely match the experimental data (Table 2.1). The simulated electrons also have approximate Maxwellian distributions in v_z (not shown), analogous to Figure 2.6. Therefore, the significant inconsistencies in the simulated distribution of ion v_z suggest that the simulation does not include effects that both accelerate and attenuate the axial ion motion.

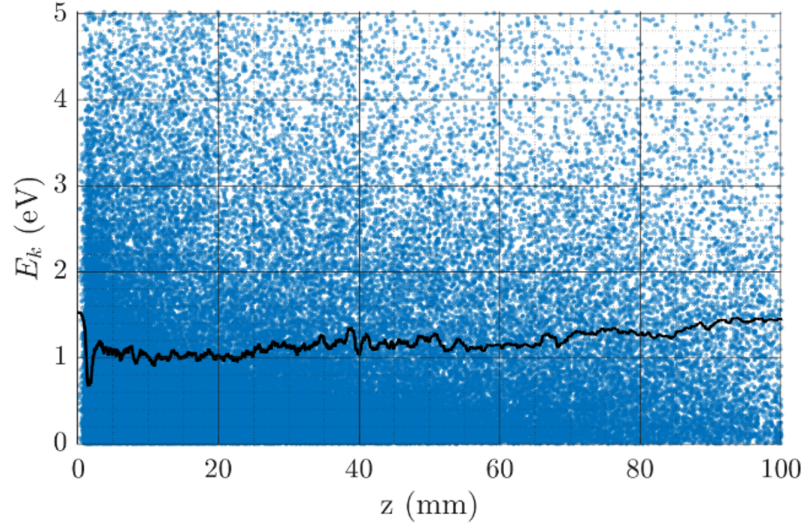


FIGURE 2.13: Electron axial displacement phase-space, blue dots represent individual super-particles in simulation. Mean value for electron temperature indicated in black demonstrating isothermal trend.

The model introduces cathode spots into the domain starting at approximately $1 - 3\mu s$ into their expansion. The model assumes that the starting charge state distributions, which are based on experimental data, are accurate to this time of spot expansion. However, given that the experimental data is derived from time-of-flight measurements, the relative fractions of higher charge states will be larger at earlier times than measured [18, 119]. A portion of high charge state ions will undergo recombination in the dense expanding cathode spot, after imparting kinetic energy to other ions through repulsion. This would create the fast tails in the experimentally observed ion velocity, explaining the discrepancy with the simulation model.

Furthermore, as the pulse progresses an actual physical, cathode arc device will accumulate metallic neutrals from the cathode and anode surfaces inside the device. These neutrals collide with plasma ions, a phenomenon that is not incorporated into the simulation model. This omission was justified by our focus on comparisons with early pulse experimental data, where we assume that the dynamics at the anode mouth are quasi-collisionless, and on starting with the simplest model. Including these collisions would be expected to broaden the ion distributions toward lower speeds v_z and energies, owing to energy transfer to the relatively cold and slow neutrals. Qualitatively, the comparison between the simulation and experimental results Figure 2.6 indicates that the experimental system begins to accumulate metallic neutrals immediately after arc propagation starts, and that the resulting collisions are important.

As outlined in Section 2.2.1, this simulation uses a cathode grounded to the vacuum chamber, chosen for simplicity, as this was used in earlier simulations. In the work of Zohrer et al. the anode is grounded to the

vacuum chamber. The differences in energy distributions between the grounded anode case and the grounded cathode case were investigated by explicitly simulating both cases (Figure 2.14).

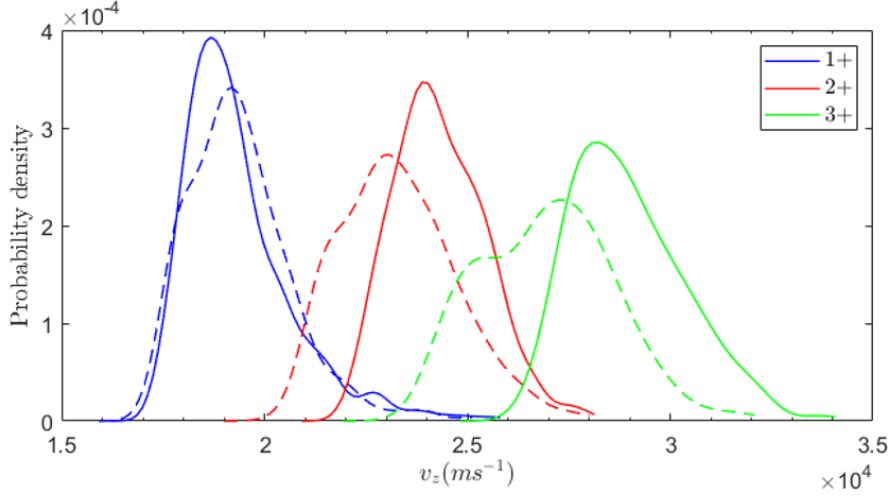


FIGURE 2.14: Comparison of *Al* ion velocity (v_z) distributions for the grounded cathode case (dotted lines) and grounded anode case (solid lines).

The results in Figure 2.14 present shifts of 4% in final axial velocity v_z , when using a grounded anode relative to the chamber walls, for both the 2+ and 3+ *Al* ion charge states. No shift is observed for the 1+ charge state. The relatively small shifts measured in our simulations predict minimal change in ion charge state energy distributions when comparing cathodic arc systems with a grounded cathode or anode.

2.3.3 Applied magnetic field effects

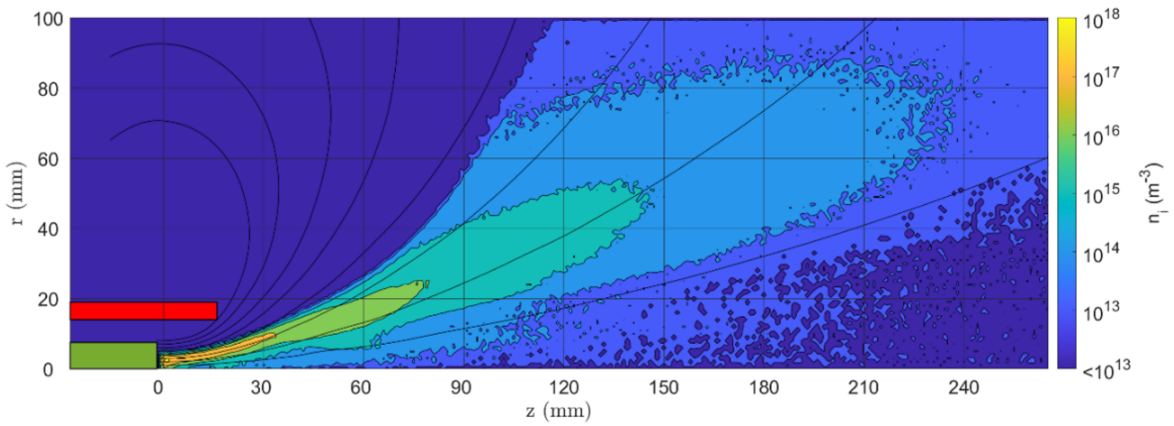


FIGURE 2.15: Magnetised *Al* ion number density n_i distribution in axisymmetric (r,z) coordinates $15 \mu\text{s}$ from pulse start with a solenoid field (black flux lines).

The simulation model was then used to predict the impact of the magnetic field applied by an external solenoid (shown in Figure 2.4), powered by a 300A power supply, on the relative ion energy distributions for *Al* and *Nb*.

As outlined in Section 2.2.1, the burn voltage and initial ion charge state distributions must be set in accordance with experimental observations. These differ for unmagnetised and magnetised arc systems. The burn voltage was changed from 23.6V (unmagnetised case) to 60V, and the charge state fractions were set to 0.05 for Al^{1+} , 0.11 for Al^{2+} , and 0.85 for Al^{3+} ions, in accordance with the published experimental data in Table 2.1 [119].

As with the unmagnetised case, the number density distribution (Figure 2.15) gives initial insight into the magnetised arc plasma behaviour. In this case, the ions are no longer as strongly concentrated along the z -axis but are now confined to the magnetic flux lines that fan radially outwards from the z -axis. If the axisymmetric simulation is viewed in three dimensions, the ion spatial distribution can be described as an annular jet, with an associated increase in ion \hat{v}_r relative to the unmagnetised case. Furthermore, due to the magnetic confinement, the ions no longer impact the anode surface or experience backflow toward the sides of the cathode.

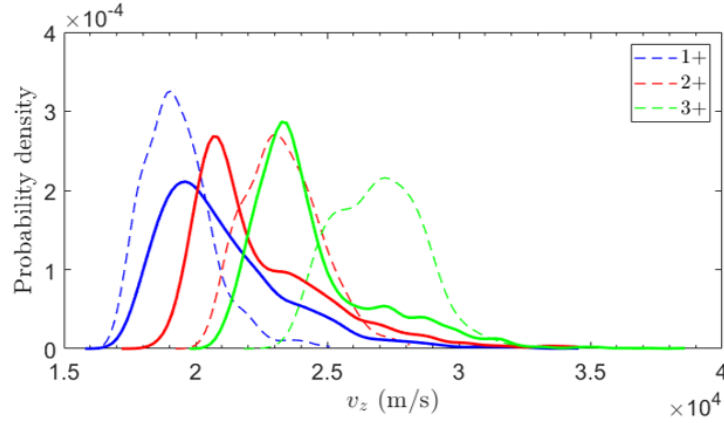


FIGURE 2.16: Simulated Al ion velocity (v_z) distributions for the unmagnetised (dashed lines) and magnetised (solid lines) cases.

The distributions in Figure 2.16 demonstrate a clear reduction in the velocity component v_z and kinetic energy for Al^{2+} and Al^{3+} ions for the magnetised case relative to the unmagnetised case, although the Al^{1+} ions peak at a slightly larger v_z and kinetic energy in the magnetised case. In detail, the peaks in the distributions in Table 2.3 show a decrease in V_{peak} of 2200 and 4000 ms^{-1} for Al^{2+} and Al^{3+} ions, respectively, corresponding to 10-20% reductions. This is in contrast with the experimental results and the theoretical consensus on the impact of magnetic nozzles (such as the magnetic field created by the short solenoid used in these simulations) on plasma discharges [36, 151]. This is also reflected in the difference in the E_k peak between the unmagnetised and magnetised results in Table 2.3.

The cause for this decrease in energy is a reduction in potential due to increased electron density n_e in the confined plume. This interpretation is supported by the n_e results in Figure 2.17, where the n_e in the plume increases in magnitude near the cathode when confined by the magnetic field. This confirms the effect of the magnetic field on electron confinement, as electron motion is inhibited across the \vec{B} -field lines, minimising

TABLE 2.3: Results for the peak in Al ion axial velocity v_z distribution as a function of charge state when a solenoid field is applied.

Material	Ion charge state	v'_{zpeak} ($\times 10^4 m s^{-1}$)	Δv_{zpeak} ($\times 10^4 m s^{-1}$)	E'_{kpeak} (eV)	$\Delta E'_{kpeak}$ (eV)
Al	1+	1.95	0.05	46	-18
Al	2+	2.07	-0.22	57	-27
Al	3+	2.33	-0.40	73	-41

propagation to the anode. This, in turn minimises ion impingement on the anode. The ultimate effect of this insulation due to the magnetic field is an arc pulse that, in a physical case, would be short-lived due to the short circuit between the cathode and anode.

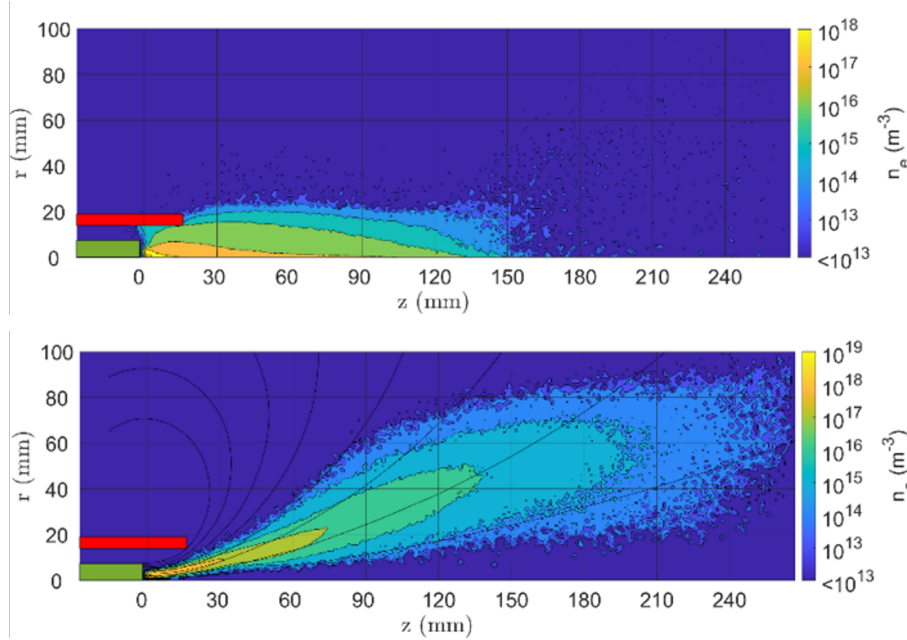


FIGURE 2.17: Al electron number density n_e axisymmetric spatial distributions at $15\mu s$ from the start of a pulse (top) without and (bottom) with a magnetic field.

The electrostatic field in the magnetised case, shown in Figure 2.18, supports this further. The valley of the low potential can be seen flaring outwards from the cathode surface, in contrast with the steep potential gradient observed in the unmagnetised case (Figure 2.7). The reduction in the potential gradient explains the decrease in the final v_z and E_k for the Al^{2+} and Al^{3+} ion charge states in the magnetised simulation model.

The analyses in Figures 2.9-2.10 of the relationship between ion E_k and the stationary electrostatic field were repeated for the magnetised case (Figure 2.19). The mean E_k for each charge state exhibited a linear trend for most ion locations. In contrast with the unmagnetised case, the gradients of the lines for the mean E_k differ significantly for each ion charge species, with the curve for $Z_i = 3+$ approximating the 1 : 1 relationship expected for purely electrostatic acceleration by a time-stationary electric field (at E_k less than $20eV$), with

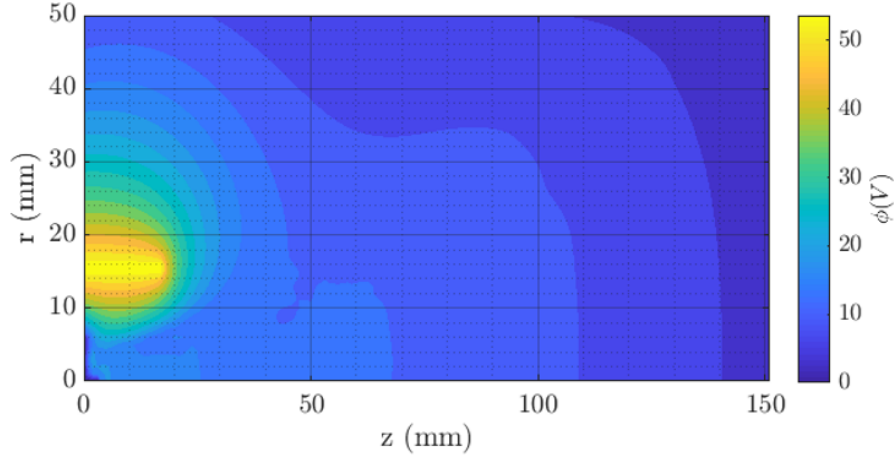


FIGURE 2.18: Electrostatic potential field of the simulated magnetised (*Al*) cathodic arc at $15\mu s$.

larger gradients for the $1+$ and $2+$ states. This increase in gradient is observed to be proportional to the charge state, with the change in E_k for the $1+$ ions, demonstrating an approximately 2 : 1 relationship. This explains why there is a slight increase in the Al^{1+} ion v_z ($500ms^{-1}$), despite attenuation due to the stationary electrostatic field gradient experienced by all of the ion species.

The analysis in Figure 2.19 also shows ion deceleration due to the smaller cathode spot potential in the magnetised case. This aligns with the demonstrated neutralising effects from increased electron confinement in the magnetised plume within the cathode/anode region. In the magnetised case there is no non-linear trend in mean E_k towards the end of the simulation domain, differing from Figure 2.11 for the unmagnetised simulation.

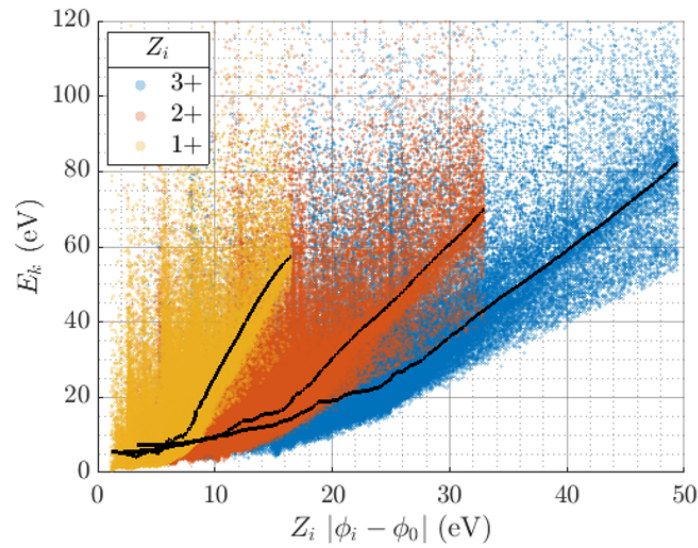


FIGURE 2.19: Plots of *Al* ion kinetic energy against the product of charge state and potential for all three magnetised simulated charge states.

The gradient of the linear trend at higher potential differences is larger than the 1 : 1 relationship expected. The increase in kinetic energy cannot be explained by the change in potential alone, and the explanation of energy exchange between the different charge states used for the magnetised case does not account for this increase in energy. The analysis of the potential near the spot over time in Figure 2.20 below shows that the potential is not stationary over the timescale of the arc simulation (a comparable timescale to the experiments, $15\mu s$), implying that ions at the edge of the domain have experienced a greater potential gradient and therefore exhibit higher energies.

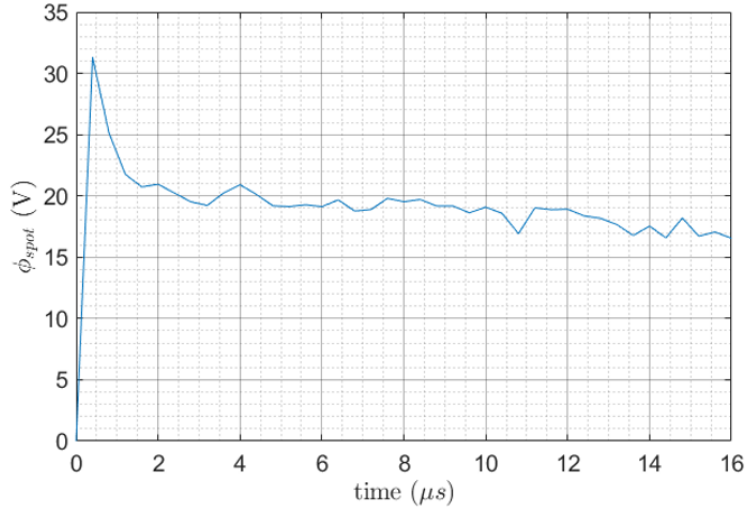


FIGURE 2.20: Electrostatic potential at the location of the cathode spot over time (magnetised).

The decrease in plasma potential at the spot location is due to the accumulation of electrons as they are generated by successive spots and are not absorbed by the anode (closing the circuit). The insulation of the electron beam from the anode in the simulation demonstrates a non-continuous arc, as a closed circuit is required to maintain an arc as it propagates along the cathode surface. This is in line with existing experimental considerations regarding the geometry of the anode and the effect of the applied magnetic field topology in the creation of continuous arcs [18].

The ion behaviour near the cathode was investigated further using the axial phase-space density (Figure 2.21). The figure shows that multiple, separate, regions of high phase density develop from a relatively continuous band for $z < 10cm$ as z increases. Spatially distinct regions are separated by approximately 5 to 7cm. These distinct regions with relatively constant spacing in z can be interpreted qualitatively in terms of electrostatic wave development, supporting the earlier finding and interpretation for the unmagnetised case, and suggesting that non-stationary electrostatic effects (e.g. wave-particle interactions) also occur in the magnetised case. The different appearances of the discontinuous structures observed in Figure 2.12 and Figure 2.21 suggest that different wave modes and different wave-particle phenomena may occur in the two cases, warranting further

investigation. The initial loss of acceleration due to the starting potential of ions in the magnetised discharge, and the subsequent effects of wave-particle interactions is the cause of charge state coupling observed in these simulation results (Figure 2.16).

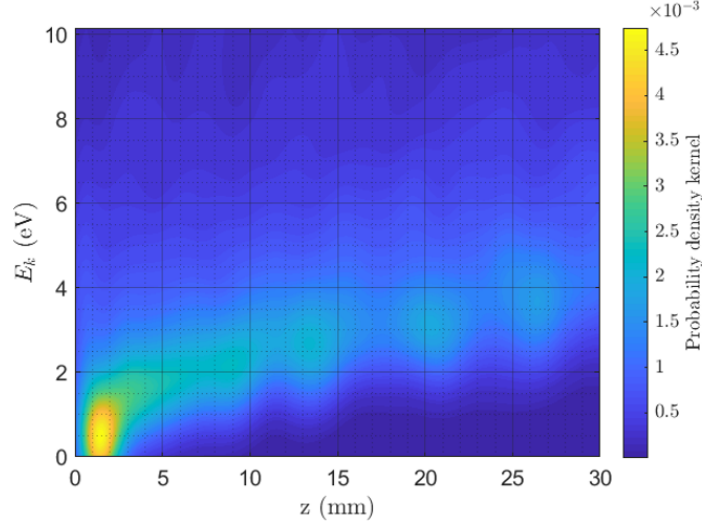


FIGURE 2.21: Magnetised Al^{2+} ion axial phase-space density plot $15\mu s$ from pulse start, colorised by particle phase density.

One utility of applied magnetic fields, as used in directed plasma sources such as propulsion and deposition systems [36], is to convert thermal plasma into a directed kinetic plume. Figure 2.16, upon initial observation, shows that application of a magnetic field can reduce v_z , E_k , and so (for the same ion number density) the thrust.

The v_z results from the magnetic field arc discharge simulation were therefore also compared to the experimental results later in the pulse ($> 90\mu s$), arguably following the proliferation of metallic neutral collisions, shown in Figure 2.22 and summarised in Table 2.4. Comparing Figures 2.6 and 2.21, the agreement and differences between the experimental and simulation results are qualitatively very similar for the magnetised and unmagnetised cases. This suggests that the same interpretations are appropriate.

Comparing the values of v_z for the peaks in the ion distributions between the late pulse experimental data and the simulation results in the magnetised case shows an increase in v_z for the Al^{1+} ions, and an indeterminate result for the Al^{2+} and Al^{3+} ions, given that the experimental uncertainty in the peak location is $2 \times 10^3 m s^{-1}$.

The increases in peak axial velocity shown in Table 2.4 are either smaller than anticipated or negative. The Mevva V experimental results from Anders et. al. measured increases in v_z at the detector of approximately $1.4 \times 10^4 m s^{-1}$, in contrast to the predicted increase of $400 m s^{-1}$ for Al^{2+} .

The radial ϕ profile of the plume taken at an axial distance $z = 25 mm$ from the cathode surface (Figure 2.23) shows a valley of low potential (11V) at $r < 10 mm$ for the magnetised case, as opposed to the constant potential

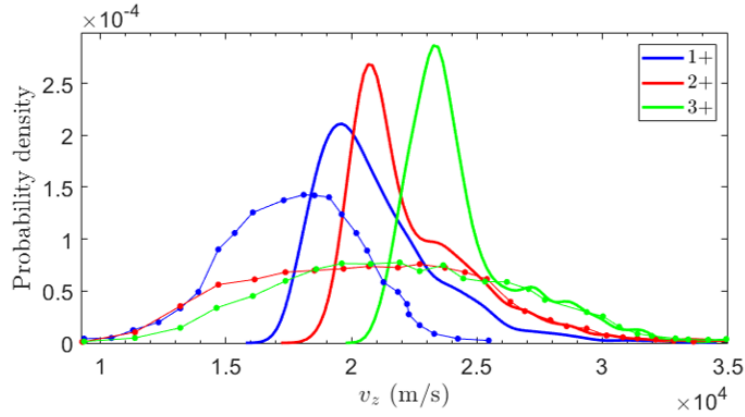


FIGURE 2.22: Simulated ion v_z distributions with an applied magnetic field (solid) and are compared with unmagnetised experimental results at $> 90\mu s$ (dotted) [116].

TABLE 2.4: Results for the peak in Al ion axial velocity v_z distribution as a function of charge state when a solenoid field is applied.

Material	Ion charge state	v'_{zpeak} $\times 10^4 ms^{-1}$	Δv_{zpeak} $\times 10^4 ms^{-1}$	E'_{kpeak} (eV)
Al	1+	1.95 ± 0.05	-1.8 ± 0.1	46
Al	2+	2.07 ± 0.03	-2.1 ± 0.2	57
Al	3+	2.33 ± 0.03	-2.2 ± 0.2	73

(22 to 25V) at the same location when no magnetic field is applied. This confirms that ion deceleration is due to the smaller potential gradient in the unmagnetised case, whereas in the magnetised case the potential structure concentrates the outgoing ions at low r for this value of z .

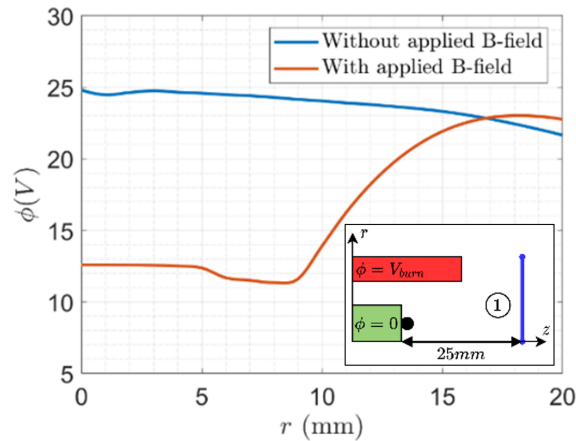


FIGURE 2.23: Radial profile of electrostatic potential at 25mm from Al cathode surface, with (inset bottom right) a diagram showing the measurement location (1).

2.3.3.1 Ion charge state filtering

The mean charge state throughout the domain was analysed to determine the relative impact of the magnetic field on different ion charge states. The unmagnetised simulation in Figure 2.24 displays a relatively spatially uniform distribution of ion charges, in contrast to the separation of different charge states radially across the plume when a magnetic field is applied (bottom panel in Figure 2.16). This can be explained by the positive radial potential gradient illustrated in Figure 2.18, as $F \propto Z_i(-\nabla\phi)$ so that higher Z_i will accelerate more readily towards larger r along the increased negative gradient found near the ridge in the potential near the plume's edge.

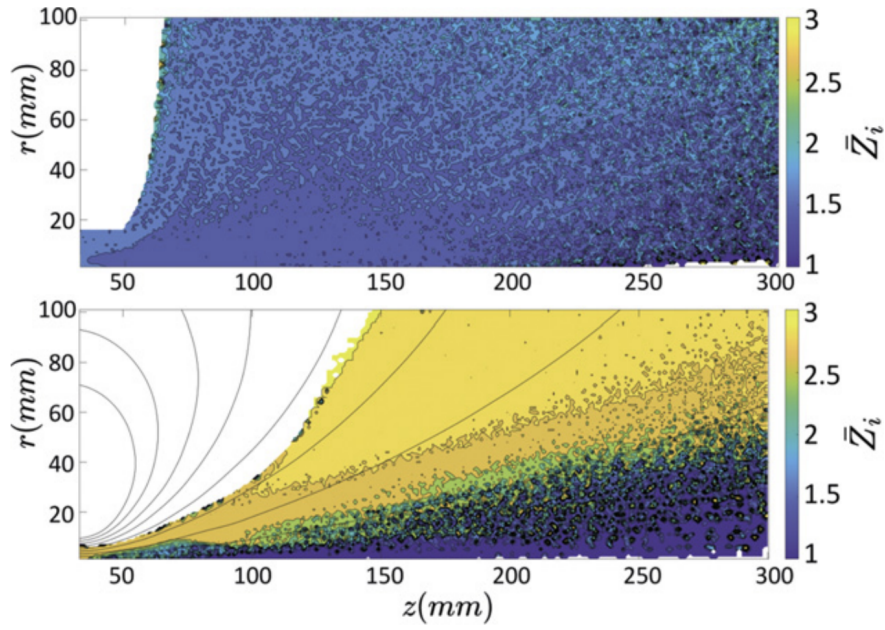


FIGURE 2.24: The mean value of the charge state Z_i (color bar) as a function of position (r, z) $15\mu s$ from pulse start (top) without and (bottom) with a magnetic field.

Figure 2.24 shows that experimental measurements of ion charge state distributions taken at the axis of the cathodic arc system will be skewed to lower charge states if a solenoid field is used to magnetise the discharge. The filtering effect is observed to increase with axial displacement from the cathode surface, due to the divergence of the magnetic field generated by the short solenoid.

2.3.4 Potential humps

Of additional interest is the investigation of a potential hump that may form between the cathode surface and anode [117]. The results in Figure 2.25 (see also Figure 2.22) show the formation of a potential hump situated 1-2 mm from the cathode surface for both the unmagnetised and magnetised simulation cases. The measurement locations are shown in the diagram in Figure 2.25. These results provide support for the basic ingredient (the

potential hump) of the potential hump theory, whereby ions are accelerated away from the potential maximum towards the cathode surface, as well as downstream.

This is also observed in the axial ion phase-space diagram in Figure 2.9, as well as the axial ion phase density shown in Figure 2.12, where there is a maximum in ion energy at the cathode surface. The maximum in ion phase density directly corresponds to the location of the cathode spot, depicted as the region of highest potential in Figure 2.7. Accordingly, with the changes in ion kinetic energy corresponding to changes in potential near the anode and cathode, the deviations from the expected 1 : 2 : 3 ratio in mean E_k for the various charge states found at larger z in Figure 2.9 and Figure 2.11 provides a strong argument that wave–particle interactions are occurring downstream in the arc plume. This is also supported by the wave-like spatial features found in Figures 2.12 and 2.21. These may result from the interactions between the plasma from successive spots, inferred from the observation of this behaviour starting within 10 mm from the cathode surface.

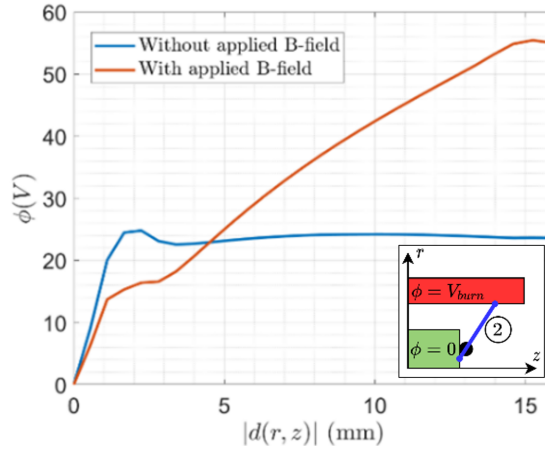


FIGURE 2.25: Profile of electrostatic potential from the Al cathode surface to the anode for the unmagnetised and magnetised cases, (showing a potential hump in the unmagnetised case) as a function of displacement magnitude $|d(r, z)|$. With (inset bottom right) a diagram showing the measurement location (1).

Experimental measurements of the bright region of the cathode spot plasma suggest that the potential hump should form at the scale of a typical crater diameter from the cathode surface [117]. The results in Figure 2.25 indicate the hump occurs $1 - 2mm$ from the surface, as opposed to the $10\mu m$ scale of spot craters. This is plausibly due to the simulation's limited spatial resolution ($\Delta r = \Delta z = 1mm$).

2.4 Conclusions

The dynamics of successive cathode spots and the resulting plasma jet were investigated using a fully kinetic collisionless simulation model of an early pulse cathodic arc plume in both the magnetised and unmagnetised regimes. The results of the unmagnetised simulations were tested and validated against the experimental results

of Zohrer et al. through comparing the relative peak *Al* and *Nb* ion v_z for three charge states. The model successfully predicts the location of the peaks in the axial ion velocity (v_z) for charge states $Z_i = 1+$, $2+$, and $3+$, with a mean error of 3% for the *Al* and *Nb* cathode materials.

The model was initially designed to simulate an *Al* cathode for validation, and was then further validated with a *Nb* cathode, with near-exact agreement for the Nb^{2+} ion v_z distribution. The observed energy distributions have significantly larger widths, extending to both smaller and larger v_z values, than the simulations. These differences are interpreted in terms of shortcomings in the assumptions of a quasi-collisionless state in the anode mouth at the start of the arc pulse, neglect of Coulomb collisions, and the initial ion charge state distributions (which are based on time-of-flight distributions observed at the end of the plasma outflow and not in the initial spot). Collisions are expected to cause ion energy loss, extending the tail of the distribution function to smaller v_z . Evidence is found for unspecified wave-particle interactions and related non-steady state effects moving energy between the various ion charge state components and extending the tails toward higher energy. The changes in ion kinetic energy for all simulated charge states were observed to be consistent with changes in electrostatic potential.

A peak in electrostatic potential was observed above the cathode surface, the start of an electrostatic gradient driving ion acceleration. This aligns with the potential hump theory, as opposed to the gas dynamic model proposed as a mechanism for the high ion energies observed in cathodic arc discharges. The acceleration of ions back toward the cathode surface exhibits final ion charge state energies that are proportional to charge state, further confirming that coupling between ions occurs downstream from the cathode surface.

The results of the simulation of the unmagnetised Miniature Arc Gun deepen the insight into the dynamics close to the cathode surface ($< 5cm$) that can currently not be probed experimentally. It was found that the ion coupling that leads to lower-than-expected relative energies for the peaks in the ion distributions for different charge states begins in this region. Furthermore, this effect is observed with a collisionless electrostatic simulation, confirming that the tendency toward equalisation of different ion charge state energies is due to non-stationary electrostatic wave-particle interactions, and not due to collisions. These interactions occur both near the cathode surface, and throughout the simulation domain, implying a variety of wave effects. The wave effects are driven, in part, by the accumulation of plasma outflows from successive cathode spots. They warrant further investigation using the simulation model.

Applying a magnetic field, produced by a solenoid with its mid-plane aligned with the cathode surface, decreased the ion energies relative to the unmagnetised case, consistent with the results of Mesyats et al. for a longer solenoid coil situated around the entire downstream plume. This effect was attributed to increased arc jet quasineutrality due to an accumulation of confined electrons, leading to the creation of a valley of lower potential and therefore a reduction in ion acceleration. Furthermore, the potential hump structure is less pronounced,

but spatially coincides with the hump observed in the unmagnetised case, as the cathode spot location also experiences an increased degree of quasineutrality and hence a lower peak potential. This effect contrasts with experimental observations of magnetised arc jets, where energy increases are observed [36]. These differences are a result of excluding plasma particle collisions with metallic vapour particles and uncertainties in initial charge state distributions.

Evidence for non-stationary electrostatic wave-particle interactions was observed in the magnetised case, causing an acceleration of ions to higher energies than predicted using the stationary electrostatic potential, and the increase in v_z for the peaks in the ion distribution for Al^{1+} and Al^{3+} ions. The simulation shows that the applied magnetic field affects the filtering of different charge states into varied spatial regions, as higher charge states accelerate more readily along the radial potential ridge created by the confined plume. The magnetised case also demonstrates a change in plume geometry, with the creation of an annular jet due to magnetic field confinement (in contrast with the axially focused plume in the unmagnetised case).

The simulation models can be used further to investigate the dynamics of the interaction multiple outflowing spot plasmas, from the near cathode region to great distances, as well as to characterise the electrostatic waves produced by the instabilities present. Furthermore, future simulations of other pulsed and continuous vacuum arc devices can be performed to investigate ion energies, ion fluxes, and overall performance, contributing to optimisation efforts. The validation of the electrostatic simulation models also offers the applicability for them to be efficiently adapted for other axisymmetric plasma devices such as RF thrusters.

Simulation and Development of an RF Plasma Thruster

Electrodeless thrusters use applied magnetic fields to create, confine, and direct plasma discharges produced without any contact with electrodes. As discussed in Section 1.3.2.3, RF thrusters are electrodeless and have an advantage over more mainstream propulsion devices such as gridded ion thrusters and Hall effect thrusters by removing the need for a hollow cathode for plume neutralisation, resulting in an improved operational lifetime by mitigating system degradation due to ion bombardment, and allowing for improved design scalability through minimisation of complexity. Design of the applied \vec{B} fields used to maximise performance such as ionisation efficiency and thrust efficiency is an active area of research, and the use of many statistical optimisation strategies remains unexplored. Further performance improvements can be made by using the magnetic energy stored inside rare earth magnets, instead of electromagnets, to create the required \vec{B} fields. The use of permanent magnets to produce a desired \vec{B} field topology is an ongoing problem, as the relationship between the relative geometry and magnetisation of magnets with the resulting \vec{B} topologies can be unintuitive. The ability to rapidly design and test configurations of available magnets to find useful solutions that can be built in a short period is of use for research exploring novel thrusters.

In this study, the novel use of Monte Carlo sampling and conditional filtering applied to optimise two annular NdFeB magnets as part of the design of a 50 – 100W helicon propulsion system is presented. The optimisation goal is to find a geometric configuration of two off-the-shelf annular magnets that (i) establish parallel field lines within a 3cm diameter helicon plasma source and (ii) maximise the diverging nozzle ratio of the MN used to create the energetic plasma jet. The conditional requirements for a design solution are formalised as a Boolean function F_s , where a value of unity indicates that all conditions are satisfied. A helicon plasma source is used due to the high plasma densities produced by the propagating EM waves (see Section 1.2.2.1) that are desirable for electric propulsion. Although the optimisation presented herein samples from a database of available magnets, the optimisation code has been developed to be agnostic to any arbitrary set of two rectangular annular magnets.

Furthermore, electrostatic PIC simulation models of the ion and electron outflows from an RF plasma source are used to test the performance of an optimisation solution by analysing plume directionality and density. Using fully kinetic PIC simulation, the predicted impact of a design produced using magnetostatic simulation can be determined before any experimentation, as hundreds of designs can be tested before components are procured.

To confirm the validity of the RF propulsion PIC model, and further validate the VSim PIC code used in this thesis the results are compared to the novel RF propulsion device constructed from the design produced through Monte Carlo sampling. Using the system as a test bed, the impact of μ metal, a high permeability nickel alloy, on plasma confinement and directionality can also be performed. The use of μ metal to adjust the \vec{B} field topology of an RF propulsion system is also a new method presented in the study. The work that was performed as part of this chapter has been presented at the 68th and 70th International Astronautical Congresses [159, 160].

3.1 Monte Carlo sampling design

Monte Carlo sampling was selected due to its ability to perform a broad exploration of possible design configurations with no prior assumptions about the relationship between a magnet geometry and the resulting \vec{B} field topology. The method is robust to local minima and solution discontinuities that may limit gradient-based optimisation methods. The method used was chosen over sophisticated space-filling methods such as Latin Hypercube sampling as these techniques make initial assumptions about the number of iterations, potentially missing solutions that meet all conditional requirements ($F_s \in (1)$) upon termination, whereas standard Monte Carlo can run until the desired number of solutions are found. The generation of multiple possible solutions means that the final selection needs to be performed by a human operator, considering other design characteristics such as weight, volume, and cost.

The physical magnet geometry was limited to two annular neodymium NdFeB magnets that are either axially magnetised in positive z or radially magnetised in negative r (towards the z -axis). The two-magnet limit was chosen to minimise the size of the design space, and therefore the number of inputs to be sampled, speeding up the run-time of the algorithm to find solutions. Each of the two separate magnets, however, can consist of a vertically stacked union of two identical magnets to create a single large magnet, conserving the commercial availability of the magnets used while increasing available geometries to sample. As a result of the possibility of sampling combined magnets, the real maximum number of physical magnets is four (when each on the sampled magnets is a combination of two from the database). The properties of each annular magnet are defined within an array \tilde{P}_M , including the magnetisation direction, magnet grade (remanence and coercivity), inner radius, outer radius, and height. The magnet properties can either be randomly generated or be based on a readily available commercial magnet, so to reduce cost and speed up development time a database was created of 41 'off-the-shelf' magnets found online. The process for randomly selecting two magnets \tilde{P}_{M_i} and \tilde{P}_{M_j} from the database, randomising their locations in the design space ($\tilde{P}_{M_i}^*, \tilde{P}_{M_j}^*$) shown in grey in Figure 3.2, performing magnetostatic simulations (covered in detail in section 3.1.1), and saving designs that fulfil the required topological conditions $F_s \in (1)$ is outlined in Figure 3.1.

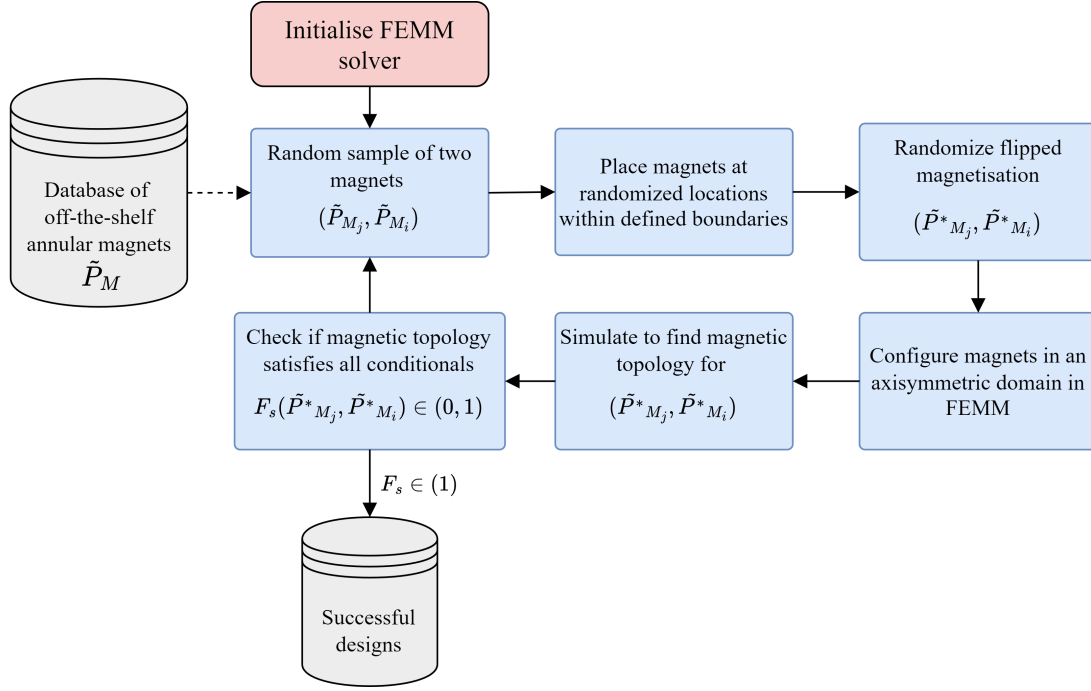


FIGURE 3.1: Overview of the Monte Carlo design space sampling for two annular NdFeB permanent magnets drawn from a database of off-the-shelf products.

3.1.1 Magnetostatic simulation

The Magnetostatic simulation software FEMM was used to determine the magnetic topology for each candidate magnet configuration, the same software used to simulate the solenoid in the cathodic arc apparatus in Chapter 2. The simulation, in this case, is still time-invariant, thus the stationary field can be formulated in terms of current density \vec{J} and magnetic potential \vec{A} where $\nabla \times \vec{A} = \vec{B}$, using Gauss's law $\nabla \cdot \vec{B} = 0$ and Ampere laws (Equation 1.18 in Section 1.2),

$$\nabla \times \left(\frac{1}{\mu(B)} \nabla \times \vec{A} \right) = \vec{J} \quad (3.1)$$

where permeability μ is a function of flux density B for nonlinear magnetic materials such as pure iron. For the isotropic case the formula reduces to,

$$\frac{-1}{\mu} \nabla^2 \vec{A} = \vec{J} \quad (3.2)$$

The simulation domain used in this study is axisymmetric, thus \vec{A} in Equation 3.2 is a scalar potential in the azimuthal direction A_θ . The boundary condition for the magnetic potential A_θ is also fixed at zero on the axis ($r = 0$). To best approximate “open” space a mixed Robin boundary was used to bound a semicircular

simulation region in the axisymmetric domain (green border in Figure 3.2). A Robin boundary is a combination of fixed potential A (Dirichlet) and fixed derivative $\frac{\partial A}{\partial n}$ (Neumann) boundaries. The constant c in Figure 3.2 is determined using the outer radius of the domain with $c = 1/\mu_0 r_0$, as the magnetic configuration is assumed to be a dipole at large r [107].

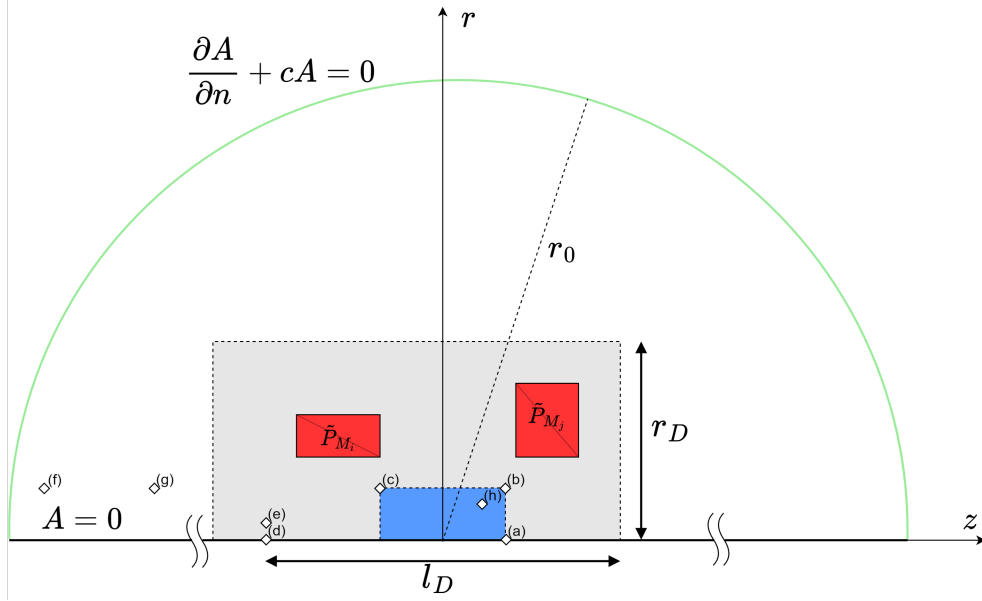


FIGURE 3.2: Axisymmetric simulation domain for performing magnetostatic simulations within FEMM showing the possible regions of magnetic material in red, the plasma source region in blue, the design space in grey, and the radial Robin boundary in green.

The magnetic field is solved in FEMM on an unstructured triangular mesh using the Newton-Raphson method for solving the finite elements that comprise the total field of differential equations described by Equation 3.1 [107, 161]. Simulations are typically fast, approximately 1s in duration, and as a result, many simulations can be performed with different geometric and magnetic properties, facilitating optimisation methods that require many runs such as Monte Carlo sampling.

3.1.2 Solution condition function

The enumerated reference locations within the magnetostatic simulation shown in Figure 3.2, also indicated locations within the modelled \vec{B} field. The precise location of each reference point in axisymmetric (r, z) coordinates are indicated in Table 3.1. The calculation of vector $\vec{B}(r, z)$ at each of these locations forms the basis for the calculation of F_s , as the majority of conditions are the ratio of B_r or B_z between two locations. The use of ratios between vector components at different locations tests the 'flow' of magnetic flux, and thus can be used to assess parallel, converging and diverging field lines.

TABLE 3.1: \vec{B} field reference locations within the magnetostatic simulation domain (Figure 3.2)

Location	r (mm)	z (mm)
(a)	0	40
(b)	15	40
(c)	15	70
(d)	0	100
(e)	5	100
(f)	15	190
(g)	15	150
(h)	10	35

To clearly outline each (B_r, B_z) ratio condition f_k the base format $\frac{\alpha}{\beta}$ for a direction \hat{z} or \hat{r} is used, corresponding with the entries in Table 3.2. There are seven conditions that comprise F_s , and the conditions (i) to (iii) are being applied to ensure flux lines move in a positive axial direction from the back of the plasma source region (blue in Figure 3.2) and into the downstream region, while conditions (iv) and (v) ensure that field lines are converging and then diverging to form an MN. Condition (vi) is used to ensure that there is a $|\vec{B}|$ of least $0.08T$ at the MN, as required for helicon EM wave propagation through the source plasma, based on an approximation by Longmier et al. and others on thrusters with similar dimensions and input power [90, 162, 163]. Finally, condition (vii) ensures a positive gradient in magnetic flux density between the plasma source and the throat of the MN, ensuring a converging-diverging magnetic topology.

TABLE 3.2: \vec{B} field reference locations within the magnetostatic simulation domain (Figure 3.2)

index	α	β	f_k
(i)	$\vec{B}_{(b)}\hat{z}$	$\vec{B}_{(c)}\hat{z}$	$\alpha/\beta > 0$
(ii)	$\vec{B}_{(b)}\hat{z}$	$\vec{B}_{(f)}\hat{z}$	$\alpha/\beta > 0$
(ii)	$\vec{B}_{(b)}\hat{z}$	$\vec{B}_{(e)}\hat{z}$	$\alpha/\beta > 0$
(iv)	$\vec{B}_{(g)}\hat{r}$	$\vec{B}_{(h)}\hat{r}$	$\alpha/\beta < 0$
(v)	$\vec{B}_{(c)}\hat{r}$	$\vec{B}_{(g)}\hat{r}$	$\alpha/\beta < 0$
(vi)	$ \vec{B}_{(e)}\hat{z} ^2$	1	$\alpha/\beta \geq 6.4 \times 10^{-3}$
(vii)	$ \vec{B}_{(d)} - \vec{B}_{(a)} $	$ z_{(a)} - z_{(d)} $	$\alpha/\beta > 0$

The Boolean function F_s can be mathematically described using logical conjunction notation as $F_s = \bigwedge_{k=7}^n f_k$ thus, $F_s \in (1)$ if all conditions $f_k \in (1)$. The open-ended formulation of F_s allows for additional conditions to be added for more explicit \vec{B} field requirements at each location. For example, the study in Chapter 4 includes axial \hat{B} requirements within a small tolerance to ensure parallel field lines in the plasma source region. The \hat{B} requirements can be retroactively added to the method presented here to improve performance for future studies.

3.1.3 Design solutions

Running the Monte Carlo design sampling loop for 5000 iterations resulted in ten magnet configurations that satisfy $F_s \in (1)$ as shown in Figure 3.3. The blue rectangle in 3.3 indicates the cylindrical plasma source when considering the axisymmetric coordinate frame, thus it can be observed that for all solutions there is a confining magnetic field followed by an MN as required by F_s .

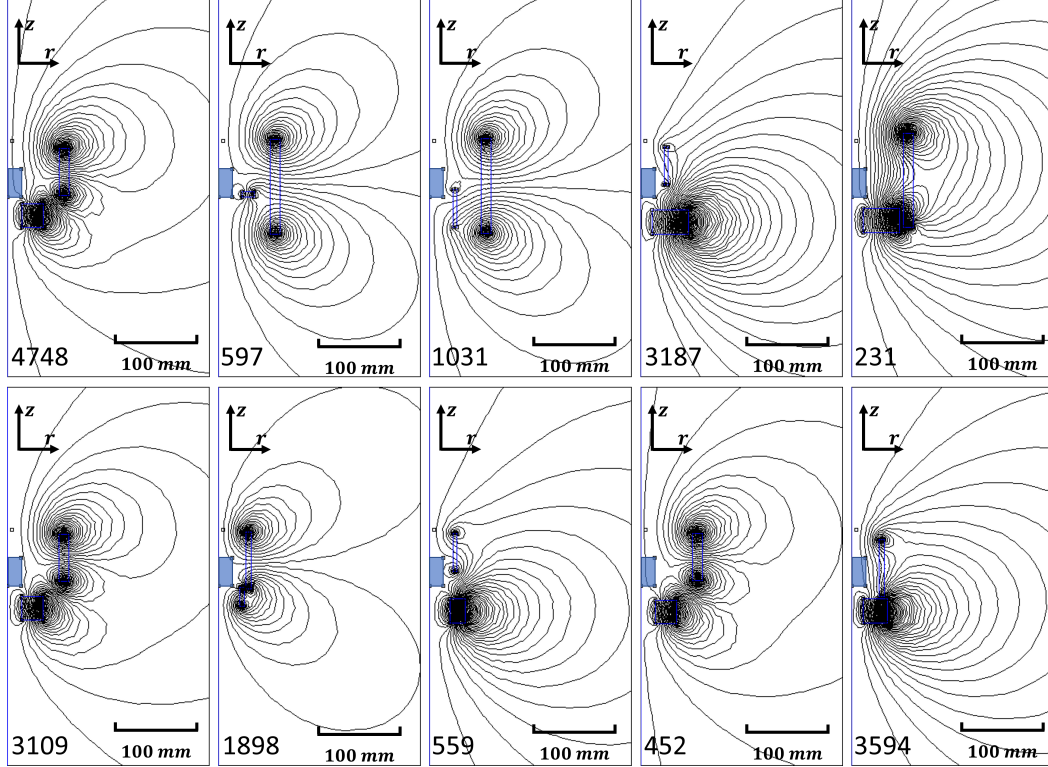


FIGURE 3.3: Magnetisation simulation results for ten magnet configuration solutions ($F_s \in (1)$) found using Monte Carlo sampling, stacked vertically in axisymmetric coordinates, with blue region corresponding to out of bounds region for plasma generation as shown in Figure 3.2 and the magnetic flux lines in black.

Solution 3594 was ultimately chosen after accounting for other practical design considerations such as volume and mass, thus minimising potential system specific impulse I_{ssp} . Through visual analysis of Figure 3.3, solutions 3187, 1898, 559, and 3594 have the smallest masses. The final choice 3594 was made based on the visually apparent parallel field lines in the plasma generation region (blue in Figure 3.3) as compared with the other three low mass/volume choices. The human assessment limitation could be overcome by employing a more sophisticated metaheuristic technique such as simulated annealing or an evolutionary algorithm in future studies. The magnet configuration 3594 includes three magnets, as the thinner radial magnet shown in Figure 3.3 is a vertical stacking of two available magnets from the database. A detailed simulation of the magnetic field topology for 3594 is shown in Figure 3.4.

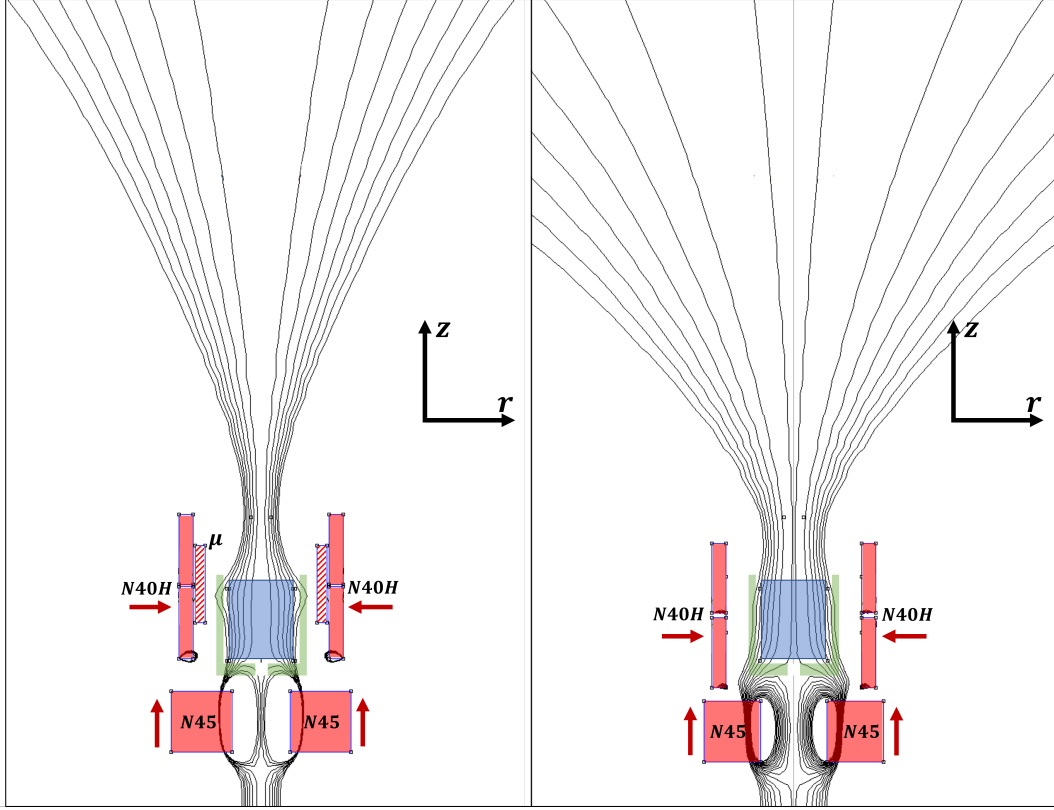


FIGURE 3.4: Cross sections through the centre of the simulated magnetic field topologies for solution 3594 with the inclusion of an annular μ metal shield (left) and without (right). Also shown are the locations of each magnet with magnetisation direction (red boxes and red arrows), the plasma source (blue rectangle), the physical plasma source walls (green), and the magnetic flux lines in black

It was observed through simulation (Figure 3.4) that the inclusion of an annular region of high permeability material such as μ metal can shield magnetic energy from the plasma source region resulting in increased parallelism of field lines in this region, as well as a more directional MN with a greater ratio for $|\vec{B}|$ at the throat and the source. As a result, the two distinct configurations shown in Figure 3.4 can be tested with minor modification to probe the effects of each \vec{B} topology on plasma behaviour.

3.2 PIC simulation model

The VSim simulation models developed as part of this thesis for RF discharges have been previously demonstrated on a similar simulation model that was validated against experiments of a cathodic arc deposition apparatus (Section 2) [106]. These simulations assume an axisymmetric structure for RF plasma discharges with magnetic nozzles. The electrostatic simulation method used is described in detail in the cathodic arc study, with the iterative electrostatic method used outlined in Figure 1.6 [106]. Simulations of different system designs were performed using electrostatic particle-in-cell (PIC) simulations, with the general process of this type of

simulation covered in Section 1.4.1. Similarly to the cathodic arc simulations, fully kinetic simulations are used with particle pushing in two axisymmetric spatial dimensions and three velocity directions (2D3V).

The required spatial and temporal resolutions for ensuring plasma simulation stability were derived based on existing data on similar RF discharges. An upper electron density of $2 \times 10^{18} m^{-3}$ and temperature of 10eV was chosen, equating to a Debye length λ_D of $1.7 \times 10^{-5} m$. Thus, the required grid size $\Delta r, \Delta z \leq \pi \lambda_D \approx 5.2 \times 10^{-5} m$ was used. Due to similarities in peak magnetic field strength with a previous study, a timestep Δt of $1 \times 10^{-11} s$ was set. The simulation domain was set up as shown in Figure 3.5, with Neumann boundaries at the far radial and axial walls, and a Dirichlet boundary of 0V at the wall to the rear of the source to represent the grounded chamber wall. As discussed in Section 3.1.1, the magnetic field data is provided by FEMM simulations, this is then imported into VSim through a python script written as part of the thesis to convert and interpolate the fixed \vec{B} field into the PIC simulation domain.

As with the cathodic arc study, similarity scaling is required to accurately resolve the plasma discharge with available computational resources [106]. The reduction in run-time is critical in this study due to the large number of simulations required to assess candidate magnetic configurations. The unscaled potential method demonstrated by Tacconga et al. is used, with the scaling factor ζ of 0.01 as validated in the study of an electrostatic plasma discharge of the same length scale ($L \cong 0.05m$) [106, 109]. As a result of the scaling factor used, the cell widths Δr and Δz are set to 1mm (lower than the limit of $\zeta^{-1} \pi \lambda_D \cong 5mm$), keeping the values from the previous study (Chapter 2). The maximum timestep is $\zeta \Delta t \cong 2 \times 10^{-13} s$, determined after inclusion of similarity scaling, using Equation 2.1 in Section 2.2.3.

Argon ions and electrons are generated in the region bounded by the physical plasma liner and the RF antenna (grey rectangle in Figure 3.5) with Maxwellian energy distributions. Ions are assumed to be a single charged species that are ‘cold’ with initial velocities determined from the room temperature thermal speed, whereas the electrons are assumed to have a temperature of 10eV, of the order commonly measured for similar discharges [104, 164]. The ion/electron generation rate of $\dot{n}_p = 5.4 \times 10^{18} particles/s$ in region shown in dark grey in Figure 3.5 is derived from a flow rate of 15sccm Argon propellant and an ionisation efficiency of 80%. The existence of Neutral particles is omitted along with Coulombic and physical collisions, which fits with the prevailing knowledge that plasma jets within magnetic nozzles are effectively collisionless, and also leads to a reduction in simulation run-time [28].

3.3 PIC simulation results

PIC simulations were run until the plume reached a quasi-steady state with an approximately stationary density distribution. The simulations for both design 3594 and the modified design with μ metal plume confinement were both run past a quasi-steady state until $6.4\mu s$ from initialisation to ensure a direct comparison can be made

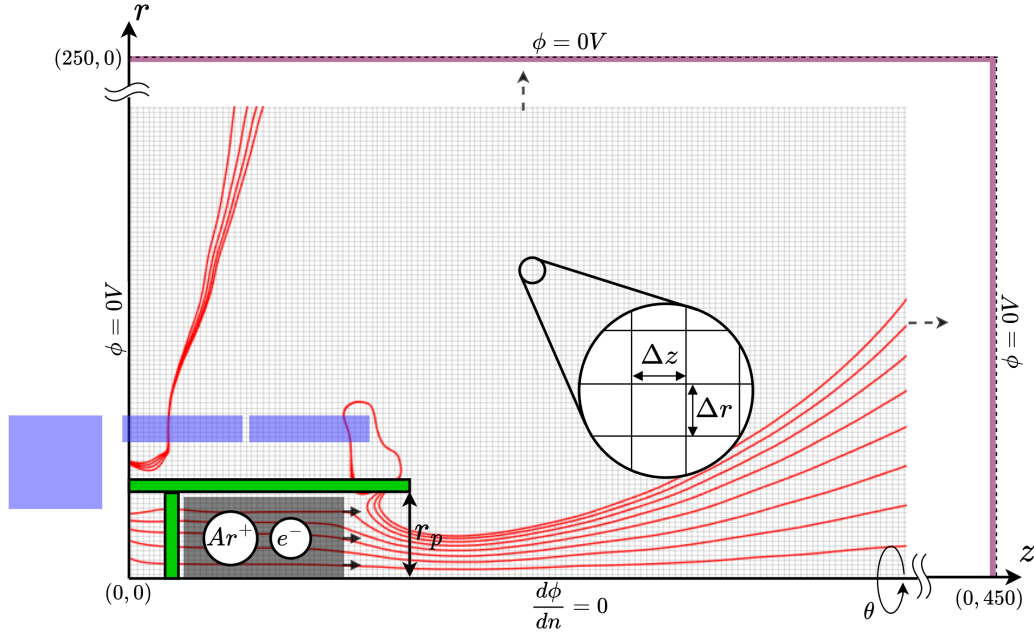


FIGURE 3.5: RF plasma source located within the PIC simulation domain, defined in axisymmetric coordinates with the indicated boundary conditions indicated. Also shown are a magnetic element configuration (blue) (example shown is solution 3594 without μ shielding), the magnetic flux lines (red), the plasma generation region (dark grey), and the physical confining boundary (green). Axes units are in mm.

between them. The number density distributions in (r, z) coordinates for argon ions and electrons with both designs are shown in Figure 3.6, demonstrating confinement to magnetic field lines (red) in the near-source region ($< 150\text{mm}$) and a quasi-neutral plume. The n_i and n_e results in Figure 3.6 reflect the results for the cathodic arc simulations in Figure 2.15. As anticipated, the plasma jet divergence has been significantly reduced through the addition of the annular μ metal magnetic shield, demonstrating through simulation the efficacy of using μ metal to manipulate MN geometry and therefore plasma behaviour. The increase in the magnitude of the ratio of the magnetic flux density at the source and the throat $B_t/B_0 = R_m$ of 1.6 to 3.3 (a twofold increase in R_m), could result in a doubling of the number of reflected particles through magnetic mirroring (Section 1.2.3) and thus a reduction in ion flux, assuming helicon wave propagation is primarily within the source region. The predicted reduction in ion flux is supported by Figure 3.6, as the sum number of particles shown is lower in the μ case.

Qualitative analysis of the ion and electron confinement in Figure 3.6 indicates that the plasma jet for design 3594 starts to diverge from \vec{B} field lines at an axial displacement from the rear source wall ($z = 0$) between 150mm and 250mm , whereas the more tightly confined jet when μ metal shielding is added does not visually diverge from \vec{B} , suggesting possible detachment at a much greater z than is simulated. The μ shielding creates

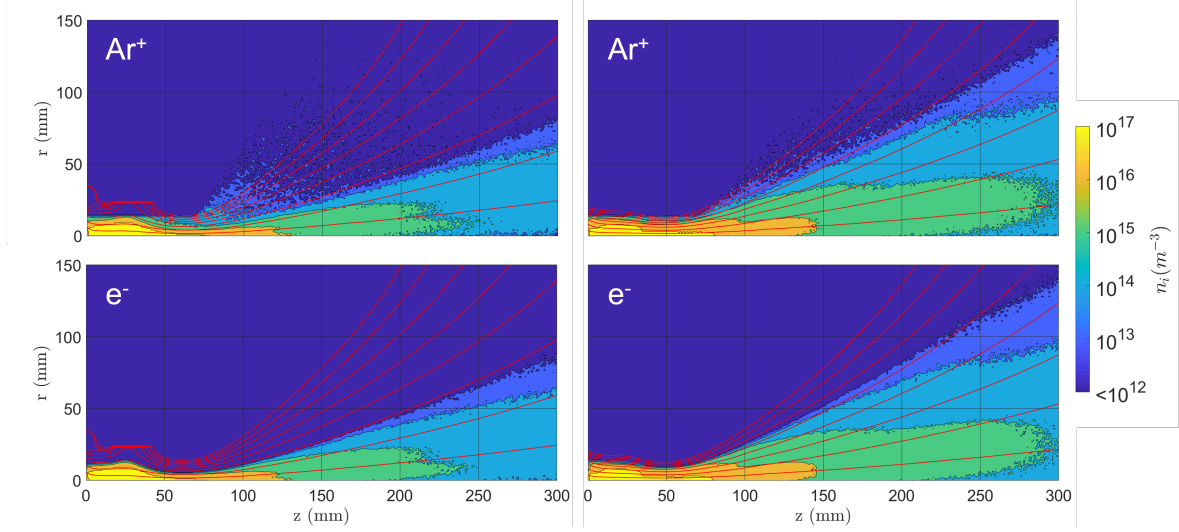


FIGURE 3.6: Number density distributions at $6\mu s$ from simulation start for Argon ions n_i (top row) and electrons n_e (bottom row). Results are for the μ metal shielded variant (left column) and the base design (right column). Magnetic flux lines indicated in red.

\vec{B} field lines that have a turning point at a much larger axial position than the default design, and as a result, the detachment location is also expected to be at a larger z than in the default case as suggested by previous research [28, 40]. Furthermore, the slight separation of the electron and ion jets, with electrons moving outwards towards field lines supports the work of Merino et al. who assert that ion and electron 'stream-tubes' are not aligned due to outward electron detachment from the MN (Section 1.2.4) [48].

The ion velocities distributed throughout the simulation domain at $6.4\mu s$ were analysed relative to the local \vec{B} to find the velocity components v_\perp and v_\parallel , with mean values as a function of the axial location shown in Figure 3.7 (a) and (b). The axial \bar{v}_\parallel trend illustrates the acceleration and confinement of ions to the applied \vec{B} field, plateauing at $z > 300mm$. The acceleration of ions occurs primarily in the source and MN throat region, in line with prior experimental and analytical observations by others [27, 28, 165]. Results for \bar{v}_\perp confirm the confinement of ions to magnetic field lines between $0mm$ and $150mm$ in the converging region of the MN for both design versions. The trend in \bar{v}_\perp also shows ions beginning to move transverse to field lines beyond $300mm$, demonstrating the possible start of detachment for a portion of the ion population in the jet. The increase in \bar{v}_\perp while \bar{v}_\parallel plateaus at $z > 300mm$ suggests there is still a degree of far field acceleration, as expected due to the potential ϕ gradient created by the expanding jet. The ion kinetic energy E_k trend in Figure 3.7 (e) confirms the axial increase in ion energy at far field ($> 300mm$) for both designs.

Each design version exhibits similar trends in v_\perp and v_\parallel , however, an increased v_\perp near the source and an increased v_\parallel past the MN throat is observed with the addition of the μ metal shield. This suggests greater ion acceleration with the μ shielded MN, as well as the reflection of ions with large v_\perp at the MN throat, thus increasing \bar{v}_\perp relative to the default design.

To confirm that the ion jet is created by the electrostatic field generated by magnetised electrons and unmagnetised ions the mean gyroradius \bar{r}_g for both ions and electrons was determined as a function of z , as presented in Figure 3.7 (d). Gyro-radii that are significantly larger than the length scale of the changing magnetic field $\bar{r}_g \gg |B/\nabla \vec{B}|$, implies demagnetisation as after one full rotation the particle will have moved significantly further away from the magnetic source [166]. The ions are demagnetised with a \bar{r}_g of $1 \times 10^4 \text{mm}$ for both designs, whereas the electrons are magnetised with a \bar{r}_g of 10mm .

An effect of the μ metal shield that is not demonstrated using PIC simulation in this study is the improvements in performance by increasing the axial directionality of \vec{B} in the plasma source region, as parallel field lines are a prerequisite for effective helicon wave propagation (Section 1.2.2.1).

A common strategy used to predict ion detachment is to assess the relative effects of the pressure supplied by the magnetic field of the MN and the plasma pressure [132]. Plasma β is the ratio of plasma pressure to magnetic pressure, so a value greater than unity implies that the force of the plasma on itself is greater than the force from the \vec{B} field. Mathematically, β is equivalent to $(nm_i v_i^2 \mu_0)/|B|^2$, where n is the local plasma density, v_i and m_i is the ion velocity and mass, and $|B|$ is the local magnetic flux density. By extrapolating the trends for β in Figure 3.7 (f) the condition for ion detachment presented by Ilin et al. of $\beta > 1$ will be achieved prior to 500mm and 550mm for the default and μ shielded designs respectively [132]. As the MN turning point locations for the default design and the μ shielded design are $(r, z) = (280, 310)$ and $(280, 420) \text{mm}$, the $\beta > 1$ condition at a larger z than the turning point is confirmed for both designs.

3.4 Experimental validation

To validate the PIC simulation model and confirm the overall design strategy, the determination of ion energy and plasma jet density is required. Experimental analysis of the two designs explored in the previous sections was undertaken in stages, starting with the development of the thrusters themselves including holding and protecting the permanent magnets, and the creation of a helicon source that could be inserted into each design. Following the development of the devices, they undergo an initial operation in a vacuum and are analysed using plasma diagnostic equipment.

3.4.1 Thruster development

The magnets selected in Section 3.1.3 for the RF thruster require a vessel to ensure structural integrity, as the axially magnetised magnet has a peak \vec{B} field magnitude of 1.5 at the surface. Teflon was selected as the vessel material due to its tensile strength, machinability, and dielectric properties such as strong electrical insulation. The two housing units that comprise the magnetic vessel were designed to shift axially for assembly

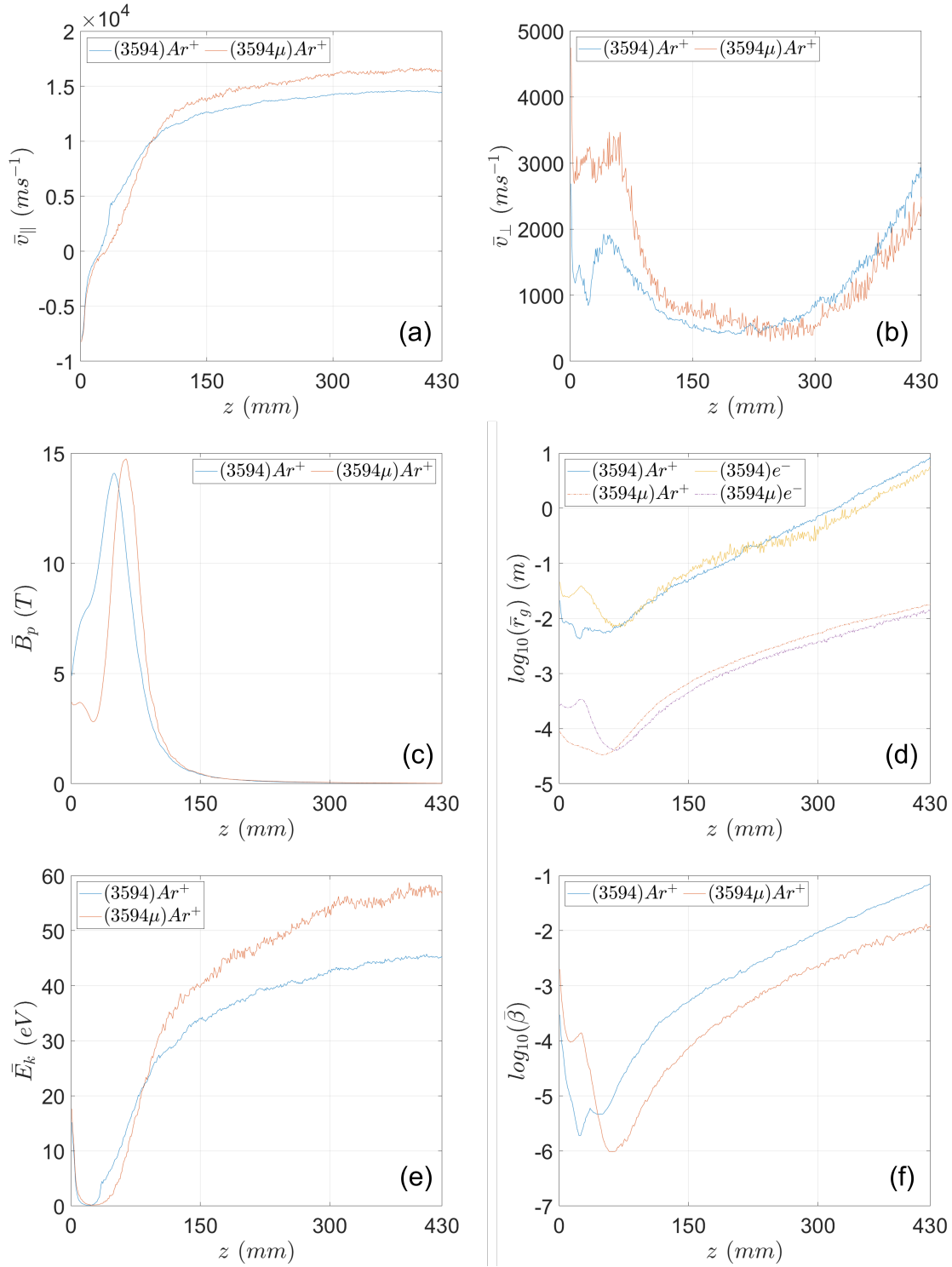


FIGURE 3.7: Analysis of PIC simulation model data as a function of axial location for both designs, showing parallel (a) and perpendicular (b) Argon ion velocity relative to \vec{B} , mean local magnetic flux density of the plasma jet (c), Larmor radius for each plasma species (d), Argon ion kinetic energy (e), and plasma β (f).

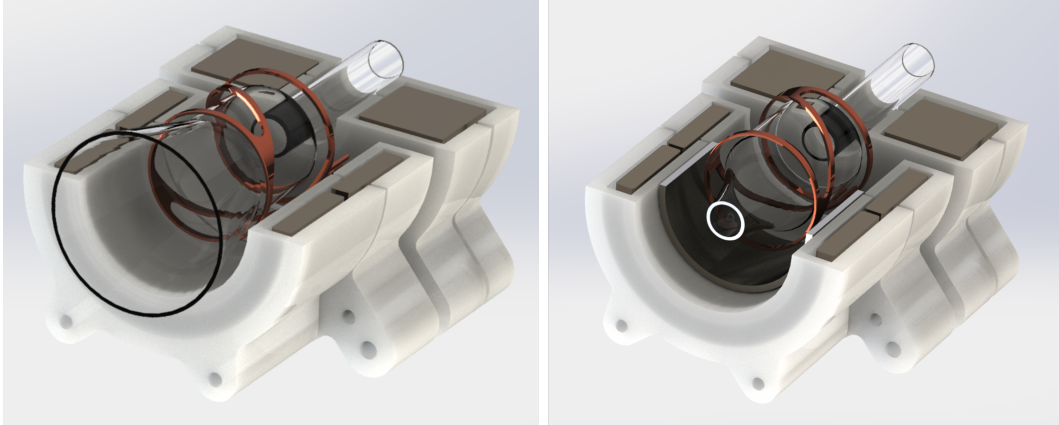


FIGURE 3.8: Render of design 3594 showing the magnet vessel, copper helicon antenna and physical plasma nozzle (left), along with the μ metal confinement version (right) with annular μ metal shield also shown.

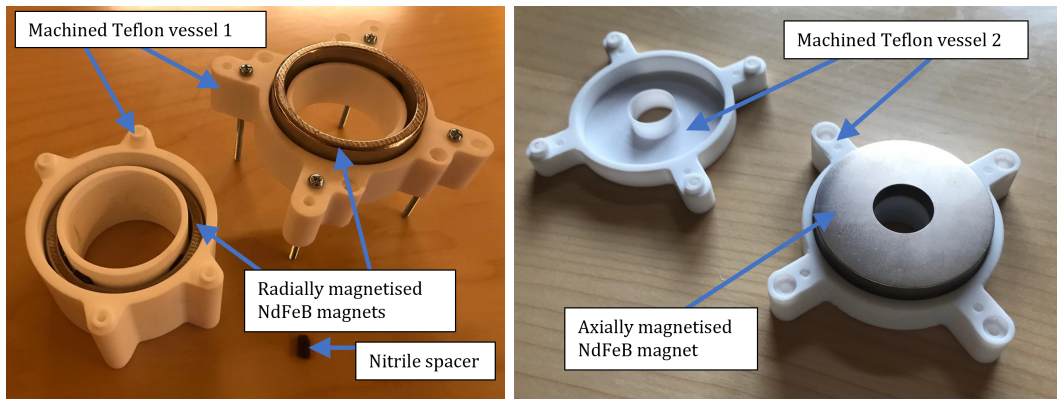


FIGURE 3.9: Physical annular NdFeB magnets sitting inside the machined Teflon housing prior to assembly.

and maintenance as shown in Figure 3.8, as the repulsion between each unit is dangerous when they are situated at the 5mm displacement required by the design.

The successfully machined Teflon vessel components are shown in Figure 3.9, along with the three NdFeB magnets (one large axially magnetised unit and two smaller radially magnetised units). More detail on general thruster dimensions and overall design for the μ metal shielded variant is provided in Appendix C. To ensure that the magnets did not move around a tolerance of 1mm was added to the vessel design so that Nitrile spacers (example shown in Figure 3.9) could be inserted.

Two antenna modules were constructed, with one built for the standard design mode, and the other for the design that incorporates a μ metal ring to confine the MN so that it is tightly converging-diverging. Each module shown in Figure 3.10 sits inside the hollow central region of the Teflon vessel shown in Figure 3.8, thus placing the helicon source at the required location indicated by the blue region in Figure 3.2. The modules are sized to be

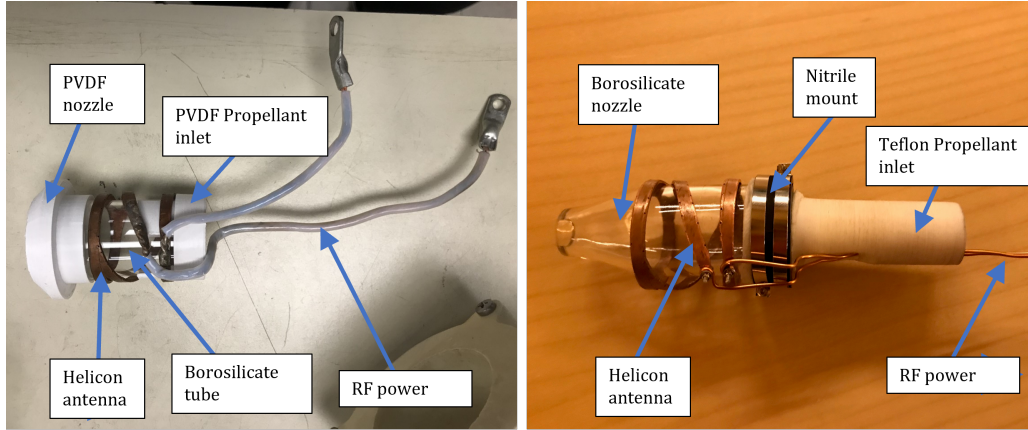


FIGURE 3.10: Base antenna module (left) and module for the μ metal variant (left), with both showing the borosilicate physical plasma vessel, RF power leads, and propellant inlets

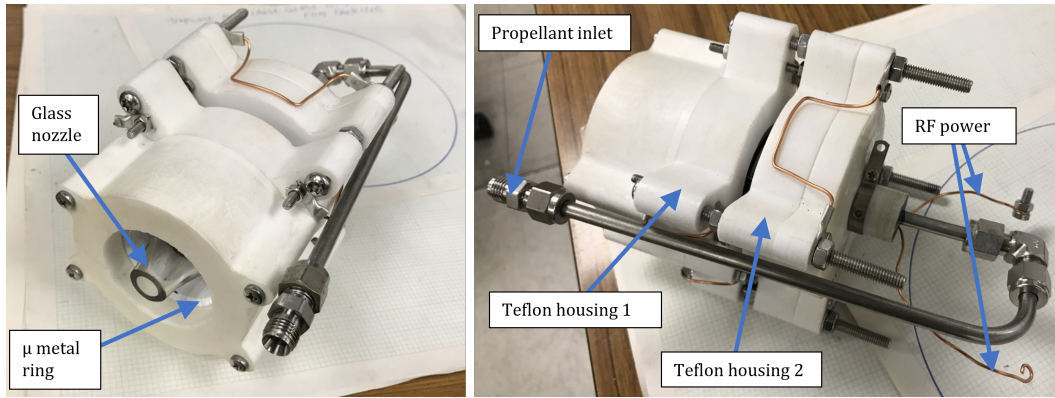


FIGURE 3.11: Fully configured thruster (μ version) with Swagelock propellant line, borosilicate glass nozzle, teflon magnet housing, annular μ metal, and RF power leads.

easily removed and swapped so that the thruster can be rapidly modified. A half-helix antenna, exhibiting a $m = +1$ mode of operation (see Section 1.2.2.1) was selected for the development of the initial thruster due to previous demonstrations of performance on similar thrusters [87, 90]. The antenna was constructed out of a single piece of copper pipe and power leads were brazed to the surface. The complete thruster configuration is demonstrated in Figure 3.11, including the Swagelok propellant line.

Power for the propulsion system is generated by a $1kW$ $13.56MHz$ supply connected to a manually adjustable matching network. The matching network was required to adjust the impedance of the helicon antenna from 29Ω at 87° to 50Ω at 0° phase to maximise forward power. Following plasma ignition, the impedance shifted, however, there was still enough forward power to maintain a discharge and collect data. Details on the previously developed matching network and modifications to the series inductor for this study can be found in Appendix A.

3.4.2 Plasma diagnostics

To validate the PIC models of the permanent magnet RF thrusters, the number densities n_i and energies E_k of Argon ions within the plasma jet at various locations were determined experimentally. Ion number density n_i can be found by employing a Langmuir probe at each location of interest, while ion energy can be determined by employing a retarding potential analyser (RPA).

3.4.2.1 Langmuir probe analysis

Langmuir probes operate by sweeping the potential of a conductor from negative to positive voltages. As the potential of the probe tip changes, different species within the plasma population will either be attracted or repelled. The resulting current at the probe tip can be analysed as a function of the applied potential to determine a range of plasma characteristics such as ion flux (related ion saturation current I_{sat} by probe projected area), plasma potential ϕ_p , and electron temperature T_e . At high or low voltages, the number of electrons or ions that can be attracted from the local plasma region will reach a maximum, and particles from outside the local region will also be attracted, this is known as electron and ion saturation.

As mentioned earlier, the ion number density n_i can also be determined using the current-voltage ($I - V$) trace that the Langmuir probe produces. To explain how this is achieved, it is important to first discuss the assumptions that are made about plasma dynamics at the probe tip due to the probe tip geometry. As discussed in Section 1.2, a surface of fixed potential within a plasma volume will create a sheath at its surface as a result of Debye shielding and electron thermal motion. For a planar probe, the plasma behaviour across the entire probe sheath is well understood and can be approximated as an infinite plane. Another common probe design uses a cylindrical tip, with the probe axis potentially transverse to the plasma current, creating complexity as particles begin to orbit the probe radius. Various theories have been proposed to build accurate analytical models for cylindrical probe tips such as Orbital Motion Limit (OML), Allen-Boyd-Reynolds (ABR), and Bernstein-Rabinowitz-Laframboise (BRL) theory [167, 168].

The Bohm criterion is a characteristic of sheaths, dictating that ions enter the sheath at a velocity greater than their sound speed $v_0 \geq v_s$ (Equation 1.22 in Section 1.2). The criterion can be used to determine the ion current at the edge of the sheath of a probe of area A , where $v_0 = v_s$, as follows,

$$I = n_s q_e A v_s \quad (3.3)$$

Here, n_s is the density at the sheath edge when ions transition to supersonic. To find the plasma density beyond the sheath, and thus the density of interest n , the electron temperature also needs to be known (from Section 1.2). By assuming a Maxwellian energy distribution for electrons the density can be determined using

$n_s = ne^{-\frac{1}{2}} \approx 0.61n$. Therefore, for the planar Langmuir probe case, the Bohm current I_B can be computed using,

$$I_B = 0.61nq_eAv_s \quad (3.4)$$

Experimentally, the Bohm current I_B is equivalent to the saturation current I_{sat} . The determination of I_{sat} is demonstrated in Figure 3.12, where the linear saturation region is extrapolated back to the plasma floating potential v_s to find I_{sat} . The remaining parameter aside from n in Equation 3.4 is the electron temperature T_e . Finding T_e using the I-V curve requires analysis of the electron transition region at positive potentials (in the 'knee' region of the I-V curve in Figure 3.12 between 30V and 60V). The 'knee' region is related to the Maxwellian electron energy distribution and will thus be linear if the natural log is taken of the current. Furthermore, the slope of the line is then related to electron temperature in eV T_{eV} by,

$$\frac{d(\ln(I))}{dV} = \frac{1}{T_{eV}} \quad (3.5)$$

Therefore, the flat region in Figure 3.12 gives the electron temperature required by Equation 3.4 and by rearranging the number density n can be determined.

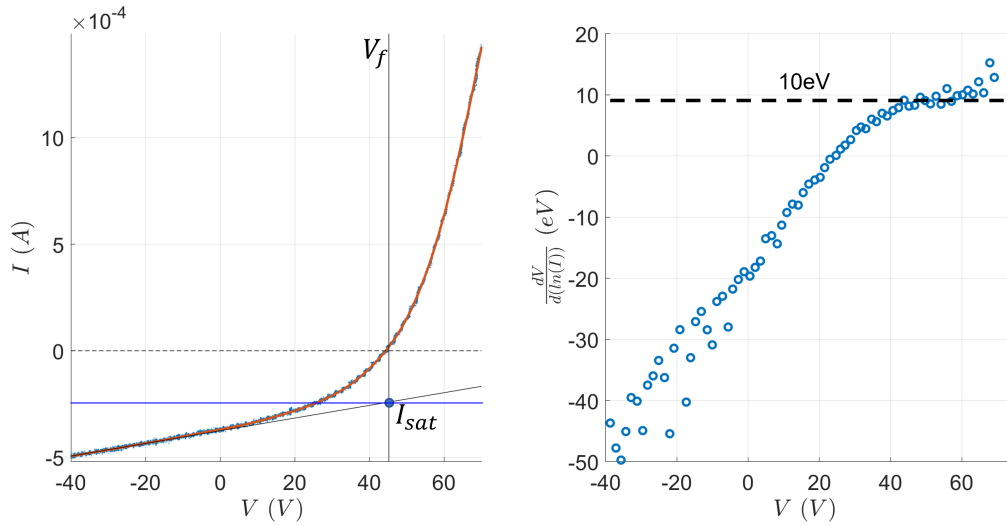


FIGURE 3.12: Example $I - V$ trace from a Langmuir probe measurement (left) with the linear fit to the ion saturation region shown in black, the plasma floating potential V_f , and intersection to extrapolated ion saturation current I_{sat} (blue). Also shown is the first derivative of the natural log of the I-V trace (right), giving the electron temperature (dotted line) via Equation 3.5.

In this study, a planar Langmuir probe is used (Figure 3.13), minimising the effects of arcing due to the RF coupled plasma and radiation within the vacuum chamber at the cost of limited spatial resolution and plasma

perturbation at large potentials, as compared to small cylindrical probes. RF compensation was also achieved using a toroidal inductor called an RF choke in line with the probe circuit [169]. Probe tip voltage was swept between $-80V$ to $80V$ using a triangular waveform at a frequency of $120Hz$. The 'L' shaped Langmuir probe was positioned so that the probe tip was in line with the thruster plume axis as shown in Figure 3.13, allowing for a rotation of the probe to physically sweep radially. By rotating and pulling the probe, measurements can be taken in r and z for direct comparison to the PIC simulation data. The Langmuir probe used has been previously demonstrated on an RF plasma source, however further modification was made to take radial and axial measurements [170].

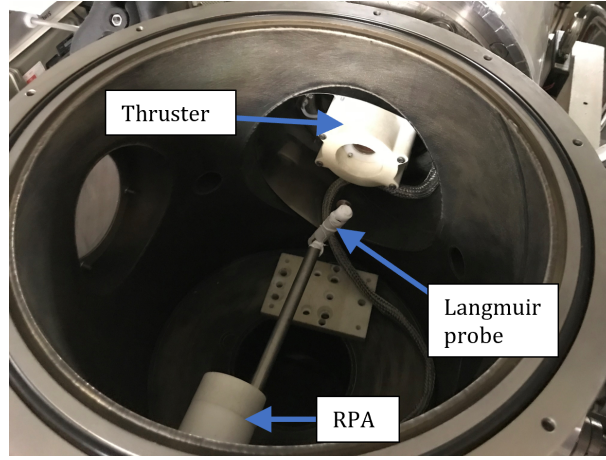


FIGURE 3.13: Locations of each probe within the vacuum system used for this study, showing Teflon coating and locations at an axial displacement from the thruster exit along its central axis.

3.4.2.2 RPA analysis

Ion energy E_k within the plasma jet was determined using a retarding potential field analyser (RPA) located close to the thruster axis. The fixed nature of the probe used reduced measurements to the z -axis only, although given the width of the probe ($2.5cm$) direct comparisons can be made with $\bar{E}_k(z)$ determined using PIC simulation. The RPA was also used for similar studies of RF plasmas and was modified to be used at differing axial locations [170].

The RPA works in a similar manner to the previously discussed Langmuir probe in that a conductive probe tip is swept between negative to a positive potential V_{probe} , repelling and attracting charged particles. The RPA differs from a Langmuir probe by screening out all electrons from the surface of the probe plate placed within an insulated vessel, thus only ion current is measured by the probe (aside from the creation of secondary electrons due to ion bombardment with the vessel and plate). Electrons are screened using a negatively biased grid of potential $V_{screen} < 0$ that is greater than the maximum electron energy at the entry to the RPA vessel, thus the effective area of the probe is the area of this grid. Ions are accelerated by the screening grid and then decelerated

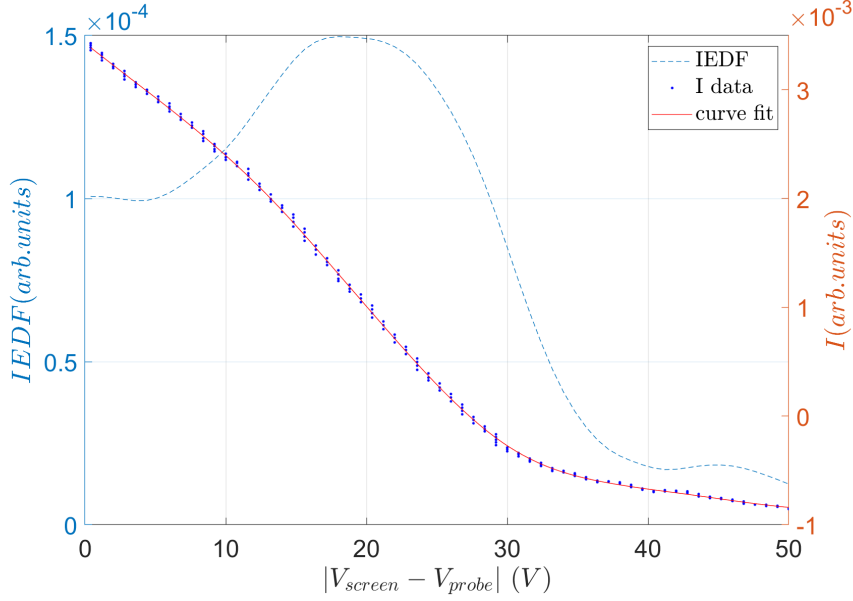


FIGURE 3.14: Example RPA probe data analysis with the cumulative ion current I raw data (blue dots), fitted curve (red), and the first derivative of I ($IEDF$) with respect to the magnitude difference between screen potential V_{screen} and probe plate potential V_{probe} . Both y-axes are in arbitrary units.

as they are incident on the probe plate at positive potential relative to the screen ($V_{probe} - V_{screen} > 0$). The cumulative distribution of ion current to the probe plate as a function of the difference in potential between the probe and the screen can be differentiated to find the ion energy distribution function (IEDF). The IEDF is thus defined as,

$$f_{IEDF} = -\frac{dI}{d\Delta V} \quad (3.6)$$

where, ΔV is the difference $|V_{screen} - v_{probe}|$. For the probe used in this study, a conservative screen bias was used of $-50V$ as electrons from RF plasma sources are typically well below this value ($T_e \ll 50eV$). The probe plate was swept linearly between $-60V$ and $60V$ at a frequency of $5Hz$. An example of a typical RPA trace as used for analysis in this study is demonstrated in Figure 3.14, showing the determination of ion energy of $20eV$ at a forward power of $50W$ at a displacement of $210mm$ from the back of the default design RF plasma source. The RPA used in this study and the study in Chapter 4 was previously developed and constructed as part of prior research work by Bathgate et al. at the University of Sydney [170].

3.4.2.3 Vacuum system

The full experimental apparatus is shown in Figure 3.15, and a core component of this setup is the vacuum chamber itself, consisting of two connected cylindrical vessels perpendicular to each other. The larger of the

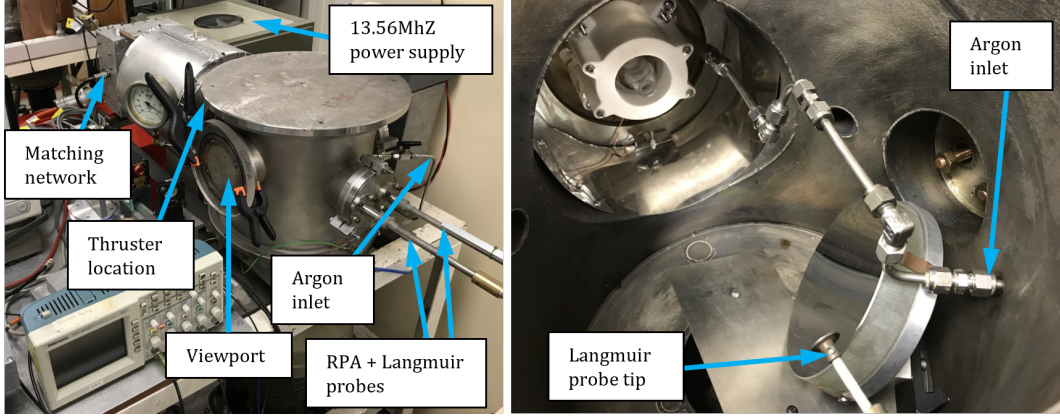


FIGURE 3.15: Experimental apparatus exterior showing stainless steel vacuum chamber vessels and the locations of the RF power supply, matching network, probe feed-throughs, and gas inlet (left). Also shown is the interior of the vacuum chamber with thruster mounting location and gas connection (right).

two vessels are in a vertical position and has an approximate volume of $0.02m^3$, and the thruster sits inside the smaller vessel pointed into the large vessel as demonstrated in Figure 3.15. A base vacuum of $0.02mTorr$ is achieved using a diffusion pump with a rotary vane backing pump.

3.4.3 Experimental results and discussion

Both designs underwent an operation at $50W$ and $100W$ forward power with a flow rate of Argon propellant of $15sccm$, and a chamber pressure of $2mTorr$ during operation in both cases. The breakdown occurred at between $20W$ and $40W$ at $2mTorr$ pressure for the base design and between $12W$ and $25W$ for the μ metal shielded version. The decrease in ignition power is expected as the μ modified design uses a physical borosilicate nozzle that converges three times more than the base design (Figure 3.4), increasing the pressure inside the source relative to the chamber. Each system operating at $50W$ forward power is shown in Figure 3.16, demonstrating plasma jets that conform to the diverging field lines of each MN close to the source and then begin to move in an expanding cone as predicted in simulation. Of note is the difference in illumination between each design, a result of the increased pressure and hence neutral density in the more confined μ design, as well as the use of an opaque nozzle for the base design, hiding the source itself from the observation port of the chamber.

Axial and radial measurements of ion number density n_i in the plasma jet produced by the base design were taken using a Langmuir probe as outlined in Section 3.4.2.1. The resulting trends for n_i illustrated in Figure 3.17 (left) show a diverging ion density distribution that forms an expanding valley of low density at the z -axis, matching the previous observations of Takahashi et al. on RF thrusters with magnetic nozzles [90]. The plasma jet geometry shown in black in 3.17 (right) aligns with the general structure predicted using the simulation model shown in blue (Figure 3.6), as the intersection point of the radial n_i trends at each axial displacement

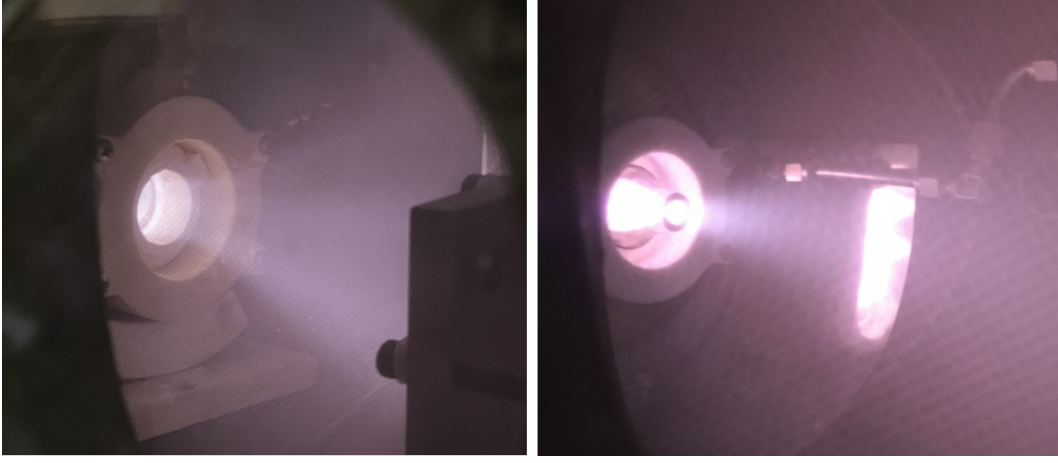


FIGURE 3.16: RF rocket operating at 50W forward power 15sccm Argon propellant (2mTorr chamber pressure) for both standard mode (left) and design with μ metal confinement (right).

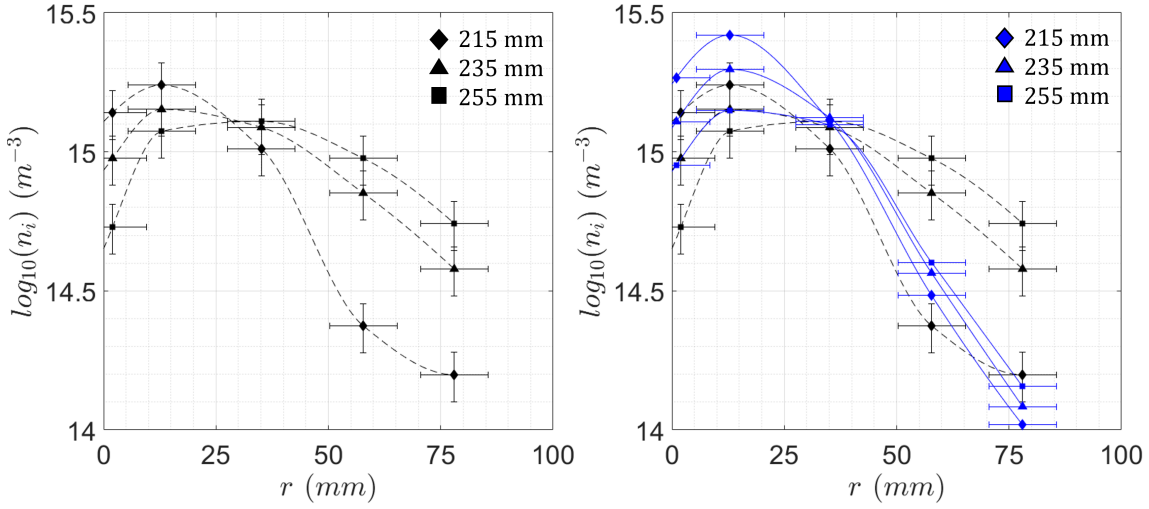


FIGURE 3.17: Argon ion number density n_i results at different radial and axial locations for the base design at 100W forward power and 15sccm flow rate (left), and overlayed with the corresponding PIC simulation results in blue (right). Dashed black lines indicate the curve fit to experimental results.

occurs at the same radial location within uncertainty ($r = 26\text{mm}$). The dashed line fits in Figure 3.17 were performed using shape-preserving piecewise cubic Hermite interpolation.

The experimental results for ion energy (IEDF) along the centre of the plume axis ($r = 0$) as a function of axial displacement z from the back of the plasma source are presented in Figure 3.18. The results show a difference between the experimental data and the data collected from the simulation model at a quasi-steady state.

TABLE 3.3: Summary and comparison of the Argon ion number density results determined experimentally with uncertainty ($n_i \pm \Delta n_i$) and with PIC simulation (n_i^*) for the default design 3594, at different locations in z and r from the origin at the centres of the back of the plasma source (matching Figure 3.17).

z (mm)	r (mm)	n_i	Δn_i	n_i^*	$ \log_{10}(n_i/n_i^*) $
215	1	1.4	0.7	1.8	0.13
	13	1.7	0.9	2.6	0.18
	35	1.0	0.5	1.3	0.10
	58	0.24	0.12	0.3	0.11
	78	0.16	0.08	0.1	0.18
235	1	0.9	0.5	1.3	0.13
	13	1.4	0.7	2.0	0.14
	35	1.2	0.6	1.3	0.03
	58	0.7	0.4	0.4	0.29
	78	0.38	0.19	0.1	0.49
255	1	0.5	0.3	0.9	0.22
	13	1.2	0.6	1.4	0.08
	35	1.3	0.6	1.3	0.01
	58	0.9	0.5	0.4	0.37
	78	0.6	0.3	0.1	0.59

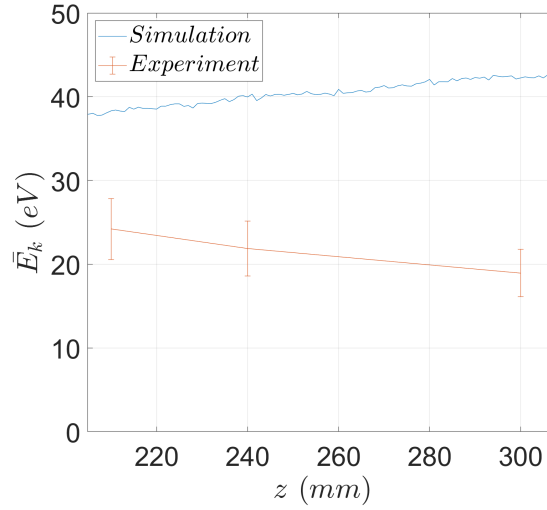


FIGURE 3.18: Axial ion energy results E_k for both the PIC model (blue) and the experimental analysis using an RPA (red with errors)

As with the density results, the difference between experiment and simulation derives from the omission of neutrals and background plasma, in this case, an attenuation of mean ion energy due to Coulombic or physical collisions with these species. The decreasing trend in IEDF data (Figure 3.18) indicates that ion attenuation is a function of displacement from the source, supporting this assertion. There is still a good agreement with the PIC simulation model at closer axial displacements to the source, as it predicts ion densities within 15eV . Future

studies will need to explore RPA data closer to the source to determine where predictions begin to deviate in experimental conditions, as the RPA used in this study was fully extended and will require lengthening.

3.5 Conclusions

Monte Carlo sampling and conditional filtering were successfully applied to the rapid design of two annular NdFeB permanent magnets, ultimately selected from a database of available products. A design was found that exhibited desirable \vec{B} field features, such as parallel field lines in the source region, a large peak magnetic flux density, and a converging-diverging MN. The novel use of μ metal to shield and thus manipulate magnetic field topology was also demonstrated for RF thrusters, increasing field parallelisation in the source region and the magnetic nozzle ratio. The addition of a magnetically shielded design variant effectively resulted in the creation of two distinct thrusters that were analysed to compare the effects of different magnetic field topologies.

An axisymmetric and fully kinetic electrostatic PIC model was developed to assess the behaviour of plasma flow within the differing magnetic nozzle designs for RF thrusters used in the study. Analysis of the PIC model data for each design demonstrated a series of effects that are key to ensuring thruster performance including increases in density, axial velocity, and ion detachment. The simulation data for the magnetically shielded (μ metal) design showed a more confined axial plasma jet as compared to the base design, however, there was also a decrease in total mass flow and thus thrust indicating that the converging-diverging MN acted as a magnetic mirror. The results suggest a trade-off between magnetic mirroring and jet divergence when developing effective MN designs. Furthermore, analysis of the plasma β each PIC simulation gave an insight into the point at which plasma pressure exceeds magnetic pressure that thus ions have detached from the MN based on early detachment models. The β results for the base design showed a predicted ion detachment location beyond $220mm$, and $300mm$ for the magnetically shielded design. In addition, the analysis of ion velocity relative to \vec{B} , v_{\perp} and v_{\parallel} as a function of axial displacement demonstrated the transition from the magnetically confined plasma jet to an independent jet as v_{\perp} increased for both designs $300mm$ from the back of the plasma source.

The PIC models were validated through the construction and testing of the two design variants in a vacuum chamber, using plasma density measurements from a Langmuir probe and ion energy measurements using an RPA. Analysis of density results for the base design showed good agreement with PIC simulation data (largest difference of 0.6 orders of magnitude), however, differences in ion energy were observed as the attenuating effects of collisions with background plasma and neutrals in the physical vacuum system at axial displacements greater than $200mm$ were omitted from the PIC models. Additionally, the general axial and radial structure of the number density distribution determined in simulation matched experimental data, as well as the data of Takahashi et al. Therefore, the experimental data supported the validity of the PIC models for plasma flow in an

MN for collisionless modes of operation such as those experienced in space or in larger vacuum systems with lower base pressures than the system used.

The presented study furthers the use of RF thrusters using permanent magnets and demonstrates effective strategies for developing complex \vec{B} field designs to maximise performance. The techniques presented can be refined by using metaheuristic methods for the magnetic design phase and intelligently configuring a larger number of smaller magnets to reduce mass (improving I_{ssp}).

Evolutionary Design of RF Plasma Thrusters

4.1 Introduction

With the rapidly increasing number of satellite missions and large constellations, highly efficient electric propulsion systems that provide cost savings and extend satellite lifetimes have become increasingly attractive. Thrusters utilising radiofrequency (RF) plasma sources avoid the issue of wall or electrode degradation by mitigating contact with the device and operational plasma as discussed in Section 1.3.2.3 [86]. This study is concerned with small satellite propulsion system optimisation, due to size constraints and diagnostic capabilities for larger devices, and the increasing popularity of small satellite platforms for space activities. RF propulsion systems generally exhibit lower thrust efficiency than Hall and Ion thrusters, and as a result their utility hinges on improvements to this critical measure of performance [53, 86].

Optimisation of RF propulsion systems to maximise their thrust efficiency is an ongoing problem, and an area that has seen minimal investigation is the use of inverse design methodologies to optimise the applied magnetic field that confines and directs the generated plasma (Section 1.2.4). The increases in available computing power are accelerating the use of topology optimisation techniques to arrange electromagnets or magnetic material in a lightweight configuration that produces an optimal field topology. Inverse design of field topologies can be utilised to leverage plasma phenomena such as magnetic mirroring and focusing to improve unidirectional plasma flow, or ensure ions leave the thruster region so that they impart momentum to the spacecraft (Section 1.2). Improved magnetic field topologies are challenging to determine analytically and the potentially complex geometries require additive manufacturing processes to be constructed. Broadly put, inverse design is the iterative optimisation of a device with minimal prior intuition about the ideal solution, leading to non-intuitive outcomes and a deep exploration of design spaces. Inverse design techniques including machine learning and metaheuristic methods (Deep learning and Genetic algorithms respectively) have successfully been applied to the optimisation of magnetic devices such as those used in magnetic fusion, magnetic resonance imaging, and magnetic refrigeration, as well as demonstrations on Hall effect propulsion devices [143–146].

Magnetic fields can be produced by both electromagnets and permanent magnets. Given the ability of permanent magnets to retain a substantial magnetisation within the lifetime of any propulsion device's use, the complexity

and energy requirements of devices optimised with these magnets can be reduced for convenient application in small spacecraft propulsion systems [53, 147]. Magnet geometries can be optimised for minimisation of mass and volume, as well as a conformity to specific dimensional constraints, a crucial application when considering the stringent design margins associated with spacecraft subsystems. Takahashi et al. have previously demonstrated improved performance for a helicon thruster using an array of permanent magnets, and the issue of optimising the arrangement of magnets to create ideal topologies was raised [95].

The RF propulsion devices optimised in this study use a helicon antenna to ionise Argon propellant in a strong magnetic field, the resulting plasma accelerates through a diverging magnetic field (aptly named a magnetic nozzle) with acceleration facilitated by a process known as ambipolar diffusion. There are many plasma rockets operating with this principle include VASMIR, a device under development at Ad Astra, the CubeSat Ambipolar Thruster (CAT), and the helicon double layer thruster. These experimental systems have demonstrated high specific impulses and promising thrust to power ratios for in-space propulsion systems [76, 87, 90, 148].

The study presented here demonstrates the novel application of evolutionary optimisation to the inverse design of a configuration of permanent magnets and magnetic field topology applied to an electrodeless plasma source. The optimisation goal in the study is to improve the thrust performance of an RF plasma source due to a magnetic nozzle and demonstrate the applicability of the presented methods to the design of plasma sources more broadly. The strategy involves a multi-objective objective function derived from an analytical model of RF plasma propulsion thrust performance (Section 4.2.3). The presented objective function allows for rapid analysis of many candidate solutions, and as a result a large region of magnet configurations can be explored to find magnetic field topologies that offer improved thrust. The more complete search of the design space results in improved optimisation over other methods such as gradient descent.

The two-dimensional magnetostatic simulations used to compute the objective function are validated using both three-dimensional simulation and measurement of a physical array using a Hall effect sensor in Section 4.3.2. The evolutionary algorithm used in this study incorporates a novel strategy for crossover as applied to two-dimensional binary configurations (or masks) of radially magnetised NdFeB material (1) or vacuum (0), for magnetic field solutions. Magnetic configurations determined using the presented algorithm are verified rigorously against fully kinetic and axisymmetric particle-in-cell simulations (Section 4.3.3). A successfully applied GA will produce monotonically increasing relationship between thrust performance and objective function score, as well as a convergence of the aggregate. The simulation and optimisation results are validated against the measured momentum flux for different magnetic configurations applied to the same RF plasma source in Section 4.4, as designed by the GA methods described herein (Section 1.5.1).

4.2 Methods

The process of undertaking the presented study is similar in structure to Chapter 3, flowing from design algorithm implementation, particle-in-cell simulation, physical thruster fabrication, and then plasma diagnostics. In this study the algorithm is evolutionary, and two objective functions are trailed for determine effectiveness, one is similar to what was presented in Chapter 3, and the second is based on an analytical model of plasma behaviour in a magnetic nozzle as well as other aspects magnetic field topologies such as magnetic mirrors. The complex physical array required further assessment to confirm that assumptions about the axisymmetric topology are valid, as a ring of cubic elements are used, as opposed to the complete annular units tested previously.

4.2.1 Evolutionary Algorithm Implementation

The evolutionary algorithm is applied in this study according to the process summarised in Figure 4.1, with the general strategy deriving from the method used by Boichot et al. as applied to a heat conduction problem [141, 142].

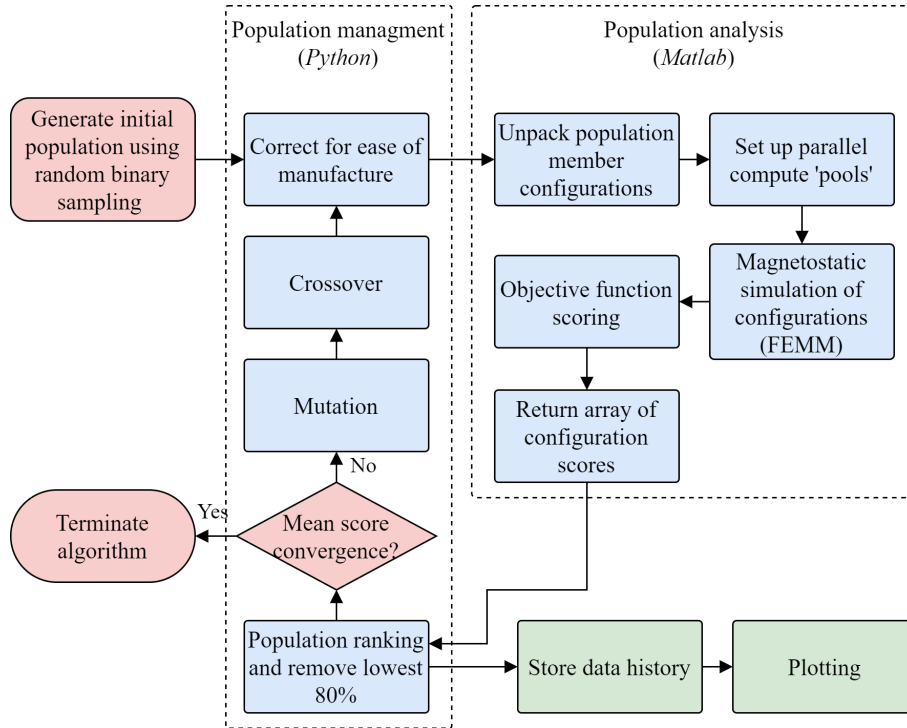


FIGURE 4.1: The general software architecture for the evolutionary magnetic topology optimisation loop used for this study.

Solution candidates take the form of discrete 2D axisymmetric binary masks Ω^* , where Ω^* is a sample of the total possible configurations within the design region shown in Figure 4.2 ($r_S \times l_S$). These binary masks are

interpreted physically as square regions in axisymmetric (r, z) coordinates, where one is radially magnetised NdFeB material and zero is empty space. In 3D space each solution is thus a configuration Ω^* of annular rings of radially magnetised NdFeB centred on the z -axis. Regions in which other vital components such as the RF antenna and device housing will reside (region bounded by l_p and r_p) are fixed as empty regions (to ensure a resulting configuration Ω^* will fit within a predetermined form factor).

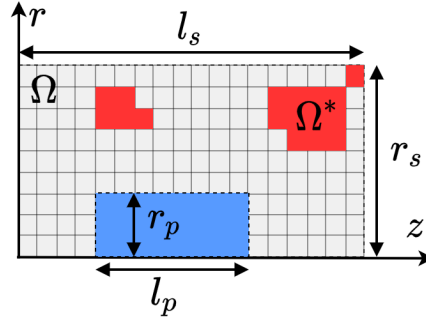


FIGURE 4.2: Overview of design space Ω (grey grid) including the exclusion region allocated for plasma generation (blue), and the regions of radially magnetised NdFeB material (red) that comprise a configuration Ω^* .

The algorithm begins with the generation of 1000 random 2D binary array samples Ω^* that are uniformly distributed. To avoid solutions that are difficult to manufacture the initial candidates are re-sampled until all 1000 samples do not contain any individual magnetic regions with no neighbours. All candidate configurations are then sent to a MATLAB function that calls FEMM in parallel and scores each candidate according to the objective function \mathcal{F} .

Scores from \mathcal{F} are returned, and the top 200 performing candidates are randomly crossed. The crossing process used in this study involves a random uniform sample between 25% and 75% in each dimension of a candidate Ω^* followed by subtraction and concatenation with the subtraction from another candidate. Each pair of candidates that are being crossed produce two ‘children’ that have been combined either vertically or horizontally. Once the 200 top candidates have been randomly paired and combined to produce a new population of 998 candidates a mutation step occurs. Mutation comprises a 4% probability ‘bitflip’ across each element in a candidate binary mask. However, it occurs only if neighbour elements are present to maximise manufacturability. The best two candidates from the prior population are propagated forward (elitism) for a total of 1000 candidates ready for the next iteration.

The sizing of each cell is $3 \times 3\text{mm}$, chosen due to the physical limitation of assembling a physical array, with this sizing resulting in solutions with up to 2000 individual cubic N52 NdFeB units. Furthermore, for efficient packing the wall thickness of the 3D printed material that holds the arrays in place reduces with decreasing unit

size, and at 3mm the limits of the 3d printer used in this study are reached ($0.6mm$). It is possible to run the optimisation outlined in this study with any cell size, and others such as Cheng et al. have used an iterative multi-resolution strategy that could be adapted and applied in future studies for this application [143].

4.2.2 Magnetostatic simulation

To determine the objective function metrics as required to calculate \mathcal{F} , efficient axisymmetric magnetostatic simulations using the open-source software FEMM were performed for each solution. The simulation domain shown in Figure 4.3 is similar to the setup presented in Chapter 3.

The simulation process involved converting the Boolean array that comprised a candidate design Ω^* into a geometric array of $3 \times 3mm$ N52 NdFeB regions within an FEMM simulation domain. As the speed of these simulations forms the biggest bottleneck in the optimisation loop, they were performed in parallel by calling multiple instances of FEMM through a Matlab script that translates large sets (typically 1000) of binary masks Ω^* into rectangular permanent magnetic regions Ω that could then be solved (following the process in Figure 4.1). Furthermore, mesh sizing was increased until consistent solutions were found. Magnetostatic outputs can be probed for magnetic field vectors at coordinates of interest and form the basis for data that is used to score a candidate using the objective functions outlined in Section 4.3.1.

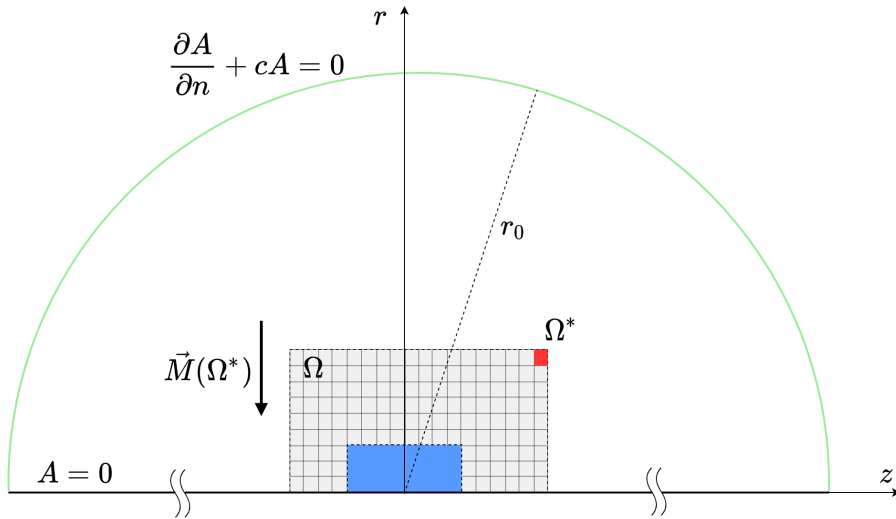


FIGURE 4.3: Magnetostatic simulation domain showing the boundary conditions, design space Ω (grey grid), and plasma generation region (blue) as in Figure 4.2. Also shown is the radial magnetisation direction \vec{M} for each magnet (red) in the configuration Ω^* .

4.2.3 Objective functions

The objective functions demonstrated in this study are derived from an analysis of solutions to magnetostatic simulations of each candidate configuration Ω^* (as described in Section 4.2.2). Objective function \mathcal{F}_1 scores configurations based on topological differences to desired magnetic field unit vectors \hat{B} and magnitude $\|\vec{B}\|$ at specified axisymmetric coordinates (r, z) . Objective function \mathcal{F}_2 scores configurations based on a series of five metrics derived from simplified analytical descriptions of magnetised plasma behaviour. These functions are now described in more detail.

4.2.3.1 Objective function method 1

The objective function \mathcal{F}_1 is a combination of differences in field values between the desired topology and a trial solution. A variety of objective functions were trialled to determine a function that repeatedly and rapidly allowed convergence to a design solution that fulfilled requirements. Objective functions that used a combination of absolute magnetic flux density, magnetic field directions, and volume of material proved to be the most successful for these systems.

The final objective function was developed using the following process. 1) A series of points are selected throughout the domain (see Figure 3.2 in Chapter 3 for an alternate example of this), tuned to the specific topology problem, such as placement in regions targeted for magnetic plasma confinement (such as the helicon source region, requiring parallel field lines). The strategy reflects that of the previously shown Monte Carlo based method in Chapter 3. 2) The magnetic field vectors are determined at these sample locations. These are predominantly converted into the unit vectors in the directions of interest so that each vector's displacement between the trial solution and the optimal can be quantified. Conditional statements are tuned to reward field directions that approach a desired topology (as set by the user) at the reference locations. 3) All of the conditional results for each reference location are multiplied. As the conditions are met, this value will approach unity, at which point the volume cost parameter will be incorporated into the final score.

The philosophy behind this approach is to prioritise conforming the solution topology to the desired topology with a certain sensitivity, and then to minimise the weight of the final configuration Ω^* . Method 1 is useful for optimising to pre-selected magnetic topologies, although it is not able to solve for thruster performance without pre-existing knowledge of an ideal topology. An example of the Matlab code used to implement method 1 \mathcal{F}_1 can be found in Appendix B.

4.2.3.2 Objective function method 2

A second objective function \mathcal{F}_2 was formulated to reflect the relative effects of a confining magnetic field on plasma momentum flux (equivalent to thrust, the measure of propulsion performance used in this study), while making minimal assumptions about magnetic field topology (contrasting with Method 1). This function incorporates the product of five distinct real valued metrics $\{\alpha_0, \alpha_1, \alpha_2, \alpha_3, \alpha_4\} \in (0, 1)$ that describe the magnetic field topology,

$$\mathcal{F}_2(\Omega^*) = \alpha_0(\Omega^*) \prod_{i=1}^4 \alpha_i(\Omega^*)^{\gamma_i} \quad (4.1)$$

Here, the exponent γ_i is a tuning parameter for adjusting the relative sensitivity of each metric relative to α_0 . The values for γ_i are initially set to unity and are changed according to meta-optimisation (simulated annealing is used in this study) to maximise the correlation between thrust and \mathcal{F}_2 based on either PIC simulation or experimentation.

The momentum flux metric α_0 is proportional to the ion momentum flux at an exit plane down range of the device, thus reflecting the thrust performance by describing conversion of radial electron pressure from the plasma source to axial electron pressure [40]. The exit plane S is presumed to be a good approximation to where the ions detach from the thruster's magnetic field (the detachment plane), as thrust is a result of the momentum exchange when ions detach from the magnetic field. The metric α_0 derives from the integral for the momentum flux \dot{Q}_S , simplified by assuming the plasma is axisymmetric,

$$\dot{Q}_S = \iint_S n_i m_i (\vec{u} \cdot \hat{n}) \vec{u} dA = \iint_S n_i m_i (u_z^2) dA \quad (4.2)$$

Here n_i is the plasma density, \vec{u} is the ion velocity, S is the plume exit surface shown in Figure 4.4, dA is an area element vector, m_i is the ion mass, and \hat{n} is the unit vector normal to S . By assuming that the ions are confined to the magnetic field lines at S (prior to detachment), and that $E \parallel B$, we can determine an integral proportional to \dot{Q}_S in terms of the magnetic flux density unit vector \hat{B} ,

$$\dot{Q}_S \propto \iint_S n_i m_i (\hat{B} \cdot \hat{n}) dA = \iint_S n_i m_i \frac{B_z}{\|\vec{V}(r, z)\|} dA \quad (4.3)$$

Reducing the integral to a discrete sum of test particles p_k moving in (r, z) incident on the test surface S of constant area leads to the following simplification,

$$\alpha_0 = \frac{\sum_k^N p_k \hat{B}_{zk}}{N} \propto \dot{Q}_S, \quad (4.4)$$

where N is the number of test particles, p_k is a Boolean array with values based on particle survival reaching S , and \hat{B}_{zk} is the axial magnetic field unit vector local to a test particle at the exit surface S (at r_e) in Figure 4.4. In the case that the particles do not reach the black exit boundaries $p_k = 0$ and thus they don't contribute to α_0 . The calculation of this metric is illustrated in Figure 4.4, where l_b is the length of the converging field region, l_p is the length of the plasma generation region, l_{mp} is their midpoint, r_b is the radius of the rear collection plane, r_p is the radius of the plasma generation region, z_s is the location of the exit plane S , and z_1/z_2 are used in the calculation of α_1 as described below. The test particles p_k shown in Figure 4.4 are removed from the simulation on contact with the loss boundaries shown in grey, or the edges of the simulation domain.

The performance metric α_0 is related to the magnetic nozzle divergence efficiency and thrust coefficient derived by Little et al., under the assumption that the plasma jet is quasi-aligned to the magnetic nozzle prior to detachment [40]. Furthermore, α_0 describes nozzle divergence and not a full description of electron pressure, required by the formulations of magnetic nozzle performance by the effect of magnetic nozzles on thrust by Takahashi et al. and others. The reformulation of α_0 and α_i to reflect state of the art descriptions of magnetic nozzle performance more closely will be performed in further studies [29, 43, 131]. Future studies will augment \mathcal{F}_2 to incorporate a more rigorous definition of the ion detachment plane, as well as extend the method's applicability to solenoid configurations in addition to permanent magnet arrays.

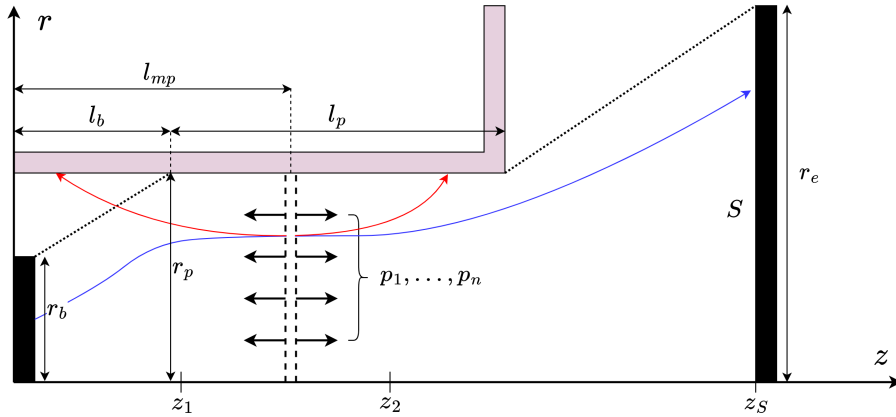


FIGURE 4.4: The Objective function setup for Method 2 showing successful (blue) and unsuccessful (red) particle tracks p_k leaving the injection plane (dotted). Exit boundaries are black and the loss boundary is the 'L' shaped region in grey/pink.

To capture the effect of plasma confinement within the magnetic nozzle, the confinement metric α_1 is used. The test particles used to calculate α_0 were used to determine the largest bounding area in (r, z) encompassed by a test particle's path through the magnetic field in (r, z) . Leveraging the non-intersection of magnetic field lines,

the particle with the largest radius at the exit surface was selected. The particle's radial location $r_{p_k}(z)$ was numerically integrated as a function of z to solve,

$$\alpha_1 = \frac{\int_{z_1}^{z_2} r_{p_k}(z) dz}{(z_2 - z_1) r_p} \quad (4.5)$$

Where the denominator indicates the maximum possible bounding area of a test particle, ensuring $\alpha_1 \in (0, 1)$ as required by $\mathcal{F}(\Omega^*)$.

To include the effect of magnetic mirroring in ensuring minimal plasma losses to the back of the device, the α_2 metric was calculated using test particle data of largest starting r as it propagated in the opposite direction. This was done to capture the change in magnetic flux from the starting location to the rear of the system, but also to confirm plasma confinement in this region. The mirror ratio r_{mirror} is proportional the ratio of test particle starting and ending radii. The metric is described by,

$$\alpha_2 = 1 - \frac{r_f}{\epsilon r_i} \quad (4.6)$$

where r_f and r_i are the final and starting radial positions of the test particle respectively, and ϵ is a factor added to allow for better convergence when test particles move to a larger radius than r_p (Figure 4.4) as they propagate backwards, set to 1.5. To ensure $\alpha_2 \in (0, 1)$ negative values were set to zero.

A second mirror ratio metric α_3 is also used to predict the impact of a converging magnetic flux region in the magnetic nozzle (creating a magnetic mirror) on ion-flux leaving the source. Unlike α_2 , α_3 is determined using the ratio of average magnetic field strength in the starting region (between z_1 and z_2 in Figure 4.4) to the peak B field magnitude, both taken along the z -axis ($r = 0$).

$$\alpha_3 = \frac{\frac{1}{(z_2 - z_1)} \int_{z_1}^{z_2} |B(z, 0)| dz}{|B_{max}(z > z_1, 0)|} \quad (4.7)$$

The metric α_4 tests for strong magnetic fields, a requirement for effective RF plasma breakdown and helicon operation (Section 1.2.2.1) [164]. This is defined as the average magnitude of magnetic flux density between z_1 and $z_2 + 30mm$, as described in Equation 4.8.

$$\alpha_3 = \frac{\frac{1}{(z_2 - z_1)} \int_{z_1}^{z_2} |B(z, 0)| dz}{|B_{max}(z > z_1, 0)|} \quad (4.8)$$

4.2.4 Particle-in-cell simulation

The PIC methodology used here is much the same as that used in Chapter 3, with a few modifications. The domain shown in Figure 4.5 has been modified from the domain in Figure 3.5 to accommodate the larger array of square regions of magnetic material. Furthermore, the back of the plasma source has been shifted to accommodate the rear magnetic mirror region that many of the presented design configurations have. Assumptions about peak density and therefore grid spacing, as well as timestep and superparticle sizing also remain unchanged from those selected in Chapter 3 (Section 3.2)

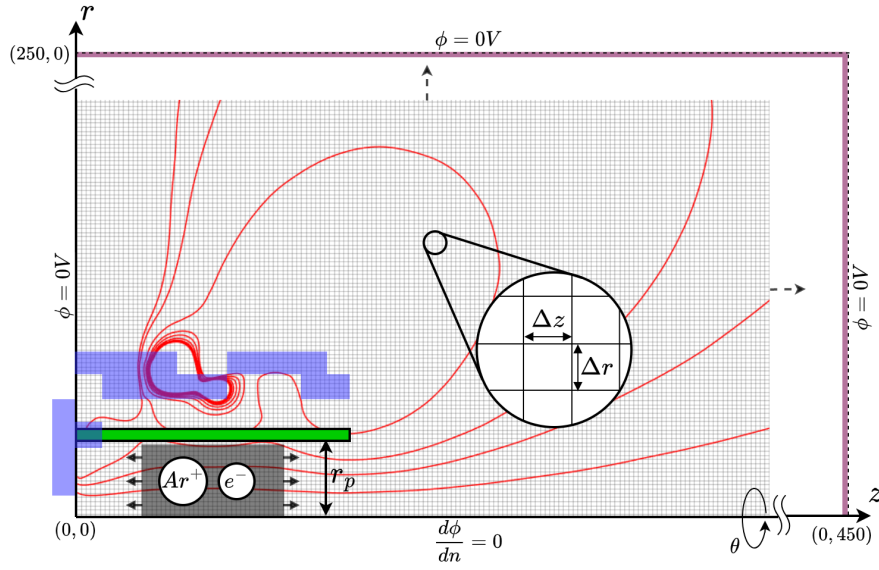


FIGURE 4.5: RF plasma source located within the PIC simulation domain, defined in axisymmetric coordinates with the boundary conditions indicated. Also shown are a magnetic element configuration (blue) (example shown is Ω_B^*), some magnetic flux lines (red), the plasma generation region (dark grey), and the physical confining boundary (green). Axes units are in mm.

4.3 Results and discussion

The study results are in four distinct sections. The first (Section 4.3.1) concerns the GA optimisation process and convergence on candidate's magnetic element configurations in axisymmetric coordinates. Section 4.3.2 outlines the experimental analysis of two physically constructed designs (3D printed out of Polyvinylidene fluoride (PVDF)) as well as a three-dimensional magnetostatic simulation to confirm that approximations made in the magnetostatic simulations covered in Section 4.2.2 are valid. Section 4.3.3 comprises the validation of object function \mathcal{F}_2 and the overall GA strategy used in this study, via particle-in-cell simulation of 8 configurations of differing score $\mathcal{F}_i(\Omega_B^*)$. The final section confirms the above methods with experimental measurements of ion

momentum flux for two configurations, with the physical magnet arrays Ω_A^* and Ω_B^* built in Section 4.3.2 added to an RF plasma source with Argon propellant.

4.3.1 Optimisation solutions

Using objective function two (\mathcal{F}_2), a solution was converged on after approximately 100 generations (Figure 4.6). Given available computation resources and the metaheuristic approach this solution was use for testing. As shown in Figure 4.6, the average population score over all 1000 candidates is analysed at each iterative generation step for both $\mathcal{F}_1(\Omega^*)$ and $\mathcal{F}_2(\Omega^*)$. Functions $\mathcal{F}_1(\Omega^*)$ and $\mathcal{F}_2(\Omega^*)$ stagnated for over 30 population sets indicating convergence. A new top solution was found in generation 105 for $\mathcal{F}_2(\Omega^*)$, suggesting that despite mean population score convergence there are incremental improvements that can be made stochastically with more compute time.

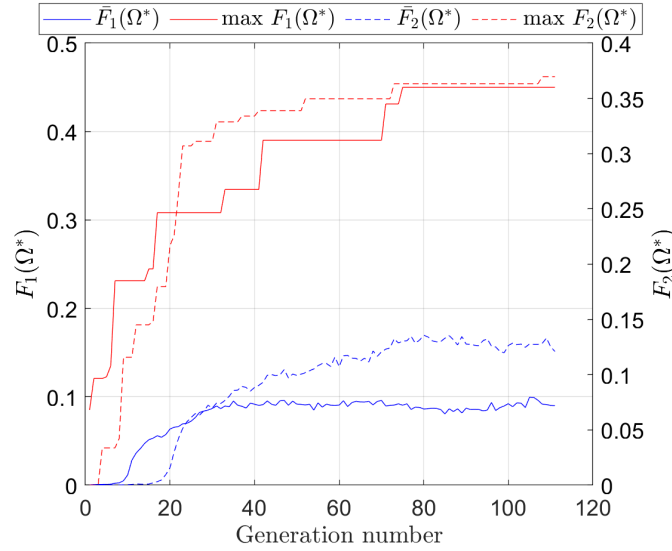


FIGURE 4.6: Iterative objective function scores $\mathcal{F}_1(\Omega^*)$ (method 1, solid lines) and $\mathcal{F}_2(\Omega^*)$ (method 2, dashed lines) for each generation, both average scores (indicating convergence) (blue) and maximum scores (red) are shown.

The convergence on a magnetic array configuration Ω^* for $\mathcal{F}_2(\Omega^*)$ is qualitatively shown in Figure 4.7, with a distinct shape emerging after 20 iterations. This was achieved by overlaying all members of each generation and finding the average density in each cell $\overline{\Omega^*}$, in a similar fashion to [141, 171].

The magnetostatic simulations in Figure 4.8 illustrate the converged distribution of radially magnetised material Ω^* shown in Figure 4.7. The results show the asymmetric magnetic flux outputs for solutions using both $\mathcal{F}_1(\Omega^*)$ and $\mathcal{F}_2(\Omega^*)$, with parallel field lines in the plasma generation region, and a converging-diverging magnetic nozzle of differing ratios. A difference between each method is made clear in Figure 4.8 through qualitative analysis of the parallel field lines in each solution, as method 2 produced lines that strictly fit the required vectors

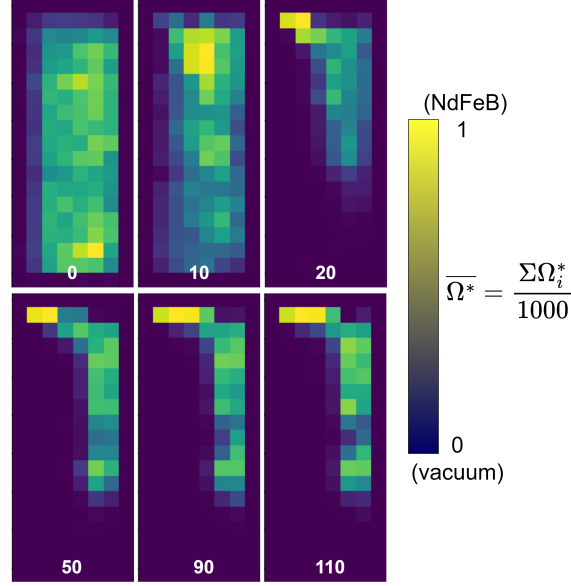


FIGURE 4.7: Average cell density $\overline{\Omega}^*$ for 1000 candidates at six population iterations as they converge from left to right (iteration indicated at the bottom), magnetised regions are indicated by yellow, empty regions are blue, and combined is in green. The population convergence for candidate Ω_B^* using $\mathcal{F}_2(\Omega^*)$ is shown.

and method 2 converges on field lines with more curvature. The topology for method two is a result of trade-offs between the metrics outlined in Section .

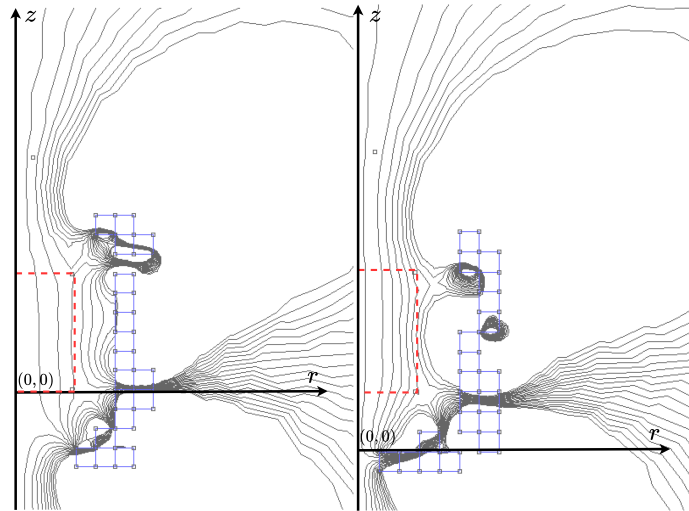


FIGURE 4.8: Magnetostatic simulation results for configurations (left) A (from $\mathcal{F}_1(\Omega_A^*)$) and (right) B (from $\mathcal{F}_2(\Omega_B^*)$), showing NdFeB elements (blue), magnetic field lines (black), and the plasma generation region (red dashed line).

4.3.2 Validation of physical magnet array

An assessment of the validity of using an axisymmetric simulation for the topologies is required, primarily due to the complexity of manufacturing thin ring magnets as opposed to mounting a circular array of inexpensive cubic magnets that approximate radial magnetisation. To ensure that the 2D axisymmetric magnetostatic simulations performed with rough meshes in FEMM were accurate to a physical array, 3D magnetostatic simulations were performed with individual cubic N52 NdFeB magnets. Physical measurements of the magnetic field of constructed devices were also used (supporting designs are shown in more detail in Appendix C). The construction of each candidate array is labour intensive, so for this study only two candidates A and B were selected for experimental comparison and validation of $\mathcal{F}_2(\Omega^*)$. Configurations A and B were chosen as each was originally developed with a different objective function (\mathcal{F}_1 for A and \mathcal{F}_2 for B), and each configuration could be assessed with \mathcal{F}_2 for future validation.

The arrays for the two test configurations A and B are exhibited in Figure 4.9. On the left the physical configuration in three dimensions illustrates the loss in material due to the packing of cubic elements. The magnetic flux analysis in Figure 4.9 (right) was performed using the python package Magpylib 3.0.1, and qualitatively demonstrates a similar structure to the 2D results in Figure 4.8. Magpylib is an analytical magnetostatic solver that can be used for three-dimensional problems [172].

Once the 3D simulation confirmed a similar field topology, the physical systems were assembled into the 3D printed PVDF (Kynar) holders (printed using a Flashforge Guider II with a PEI print bed at 100°C and extrusion nozzle at 242°C). The B_z and B_r fields were measured in (r, z) coordinates using a hall effect sensor, as shown in Figure 4.10.

By analysing test configuration Ω_B^* , all three sets of measurement results demonstrated similar magnetic field topologies (Figure 4.11 and Figure 4.12). The results validate the simplified axisymmetric FEMM simulation approach to optimising a magnetic array of small cubic magnetised elements. As shown in Figure 4.11, there are slight variations in the $|B(z, r = 0)|$ profile across all three sets of results. The variations are within the error of $\pm 1\text{mm}$ in z for the Hall effect sensor measurements. The differences between the 2D and 3D simulations can be attributed to differences in radial magnetic energy density as it becomes less efficient to pack magnets at smaller radii as compared to a perfect annulus (as seen in Figure 4.9). This is also supported by the similarity between the measured results and the 3D simulation, as they both comprise of cubic elements.

To further assess the differences in magnetic field topology for all three cases, the outer magnetic flux line encompassing the plasma generation region is compared in Figure 4.13. As with the z -axis flux density, there are small discrepancies in the flux path, however, these are similar when considering the position measurement

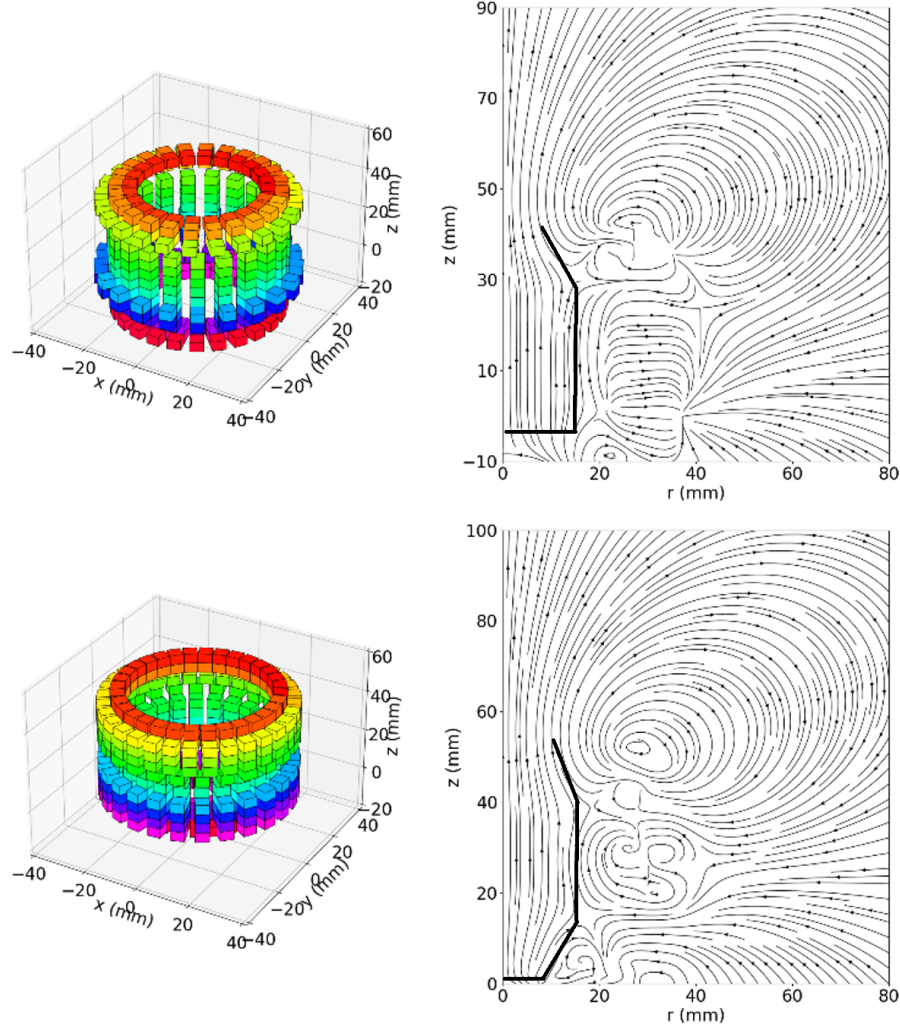


FIGURE 4.9: Demonstration of the positioning of the magnetic cube elements for test configurations Ω_A^* (top left) and Ω_B^* (bottom left). The magnetic flux lines for the 3D configurations of Ω_A^* (top right) and Ω_B^* (bottom right) are also shown to qualitatively illustrate the similarities to Figure 4.8 with overlays of the physical plasma vessel.

error for the physical array of $\pm 1\text{mm}$. The discrepancies between the 2D and 3D simulations are a result of the loss in magnetised material due to the packing of the cubic magnets shown in Figure 4.9.

4.3.3 Simulated performance predictions

Particle-in-cell simulations of the magnetic field topology for eight different NdFeB cube configurations (with different scores) labelled A to H were combined with the RF plasma source to predict the thrust performance. As shown in Figure 4.13, the distribution of ion density conforms to the magnetic field lines in the near source region ($< 100\text{mm}$) for all designs A through H. These results offer an initial qualitative insight into the performance of each configuration Ω_i^* in terms of plume directionality and mass flow. Configuration A exhibits good

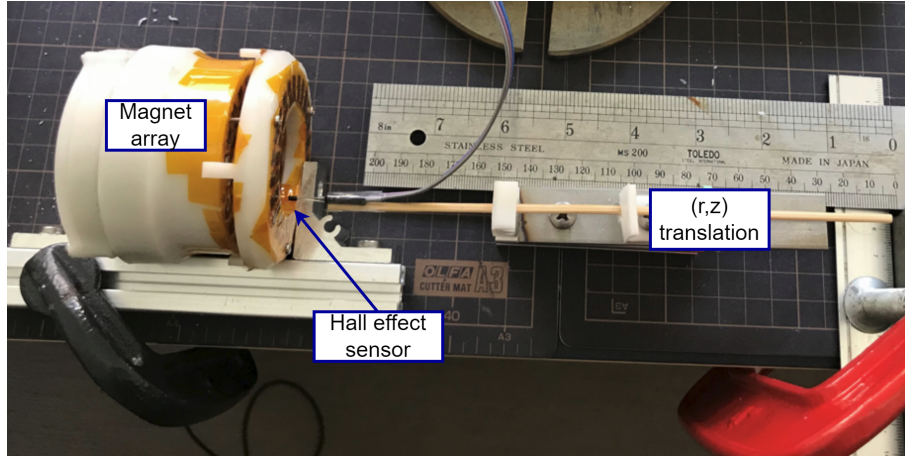


FIGURE 4.10: Magnetic field-testing apparatus for measuring B_r and B_z in (r, z) using a Hall effect sensor. In this demonstration the magnetic array Ω_A^* is being tested (left).

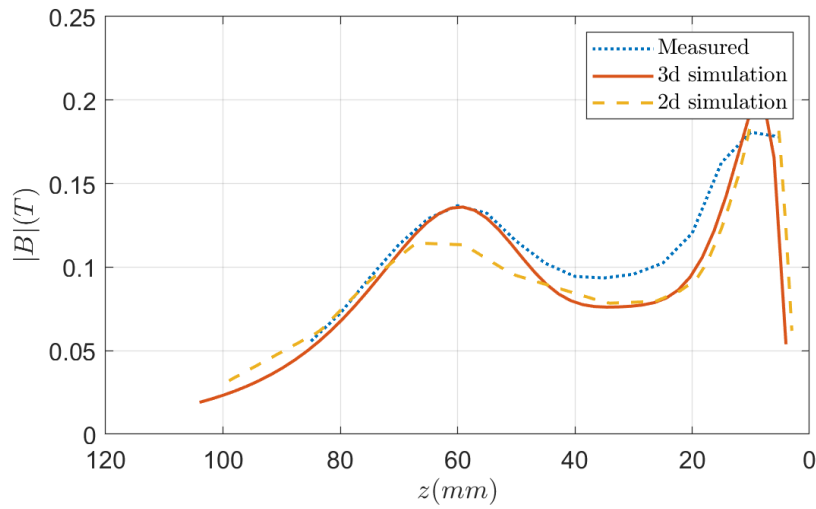


FIGURE 4.11: Magnetic flux density $|B|$ along the magnetic array z -axis showing 2D and 3D simulations in dashed orange and solid red lines respectively, as well as the measured results (dotted blue).

directionality, however there is a significant deficit in ion density compared to the other seven configurations. The simulations of configurations A, C, D and H show relatively confined plumes, with H being the most directional in z . In contrast, E, F, and G are broader, with ions reaching the top of the simulation domain before 200mm .

In addition to the ion density distribution n for each configuration Ω_i^* , the mean velocity \bar{v}_z as a function of z was determined using the simulation results. The comparison of $\bar{v}_z(z)$ between candidates is presented in Figure 4.14. As shown, there is a maximum difference in \bar{v}_z results between 200 and 250mm of $1.5 \times 10^4 \text{ms}^{-1}$. Furthermore, when the quasi-steady \bar{v}_z is compared with the ion density distribution $n_i(r, z)$ for each configuration Ω_i^* in

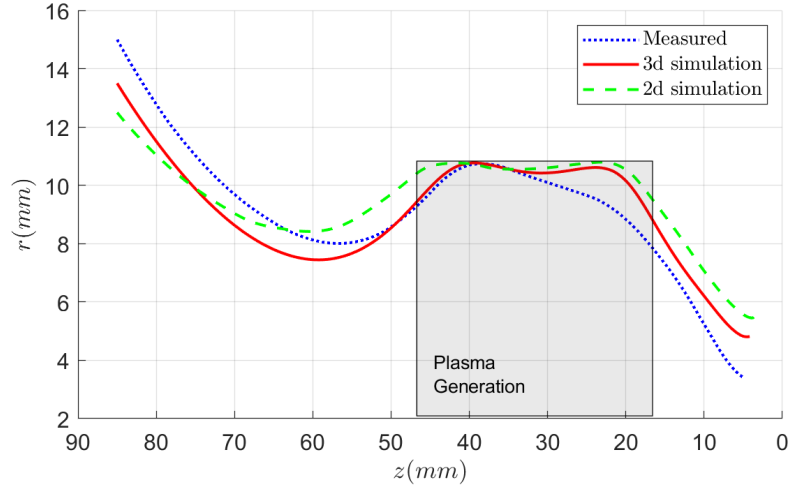


FIGURE 4.12: Magnetic flux lines $|B|$ encompassing the cylindrical plasma generation region (grey rectangle) for 2D and 3D simulations in green and red respectively, as well as the experimentally measured results (dotted blue).

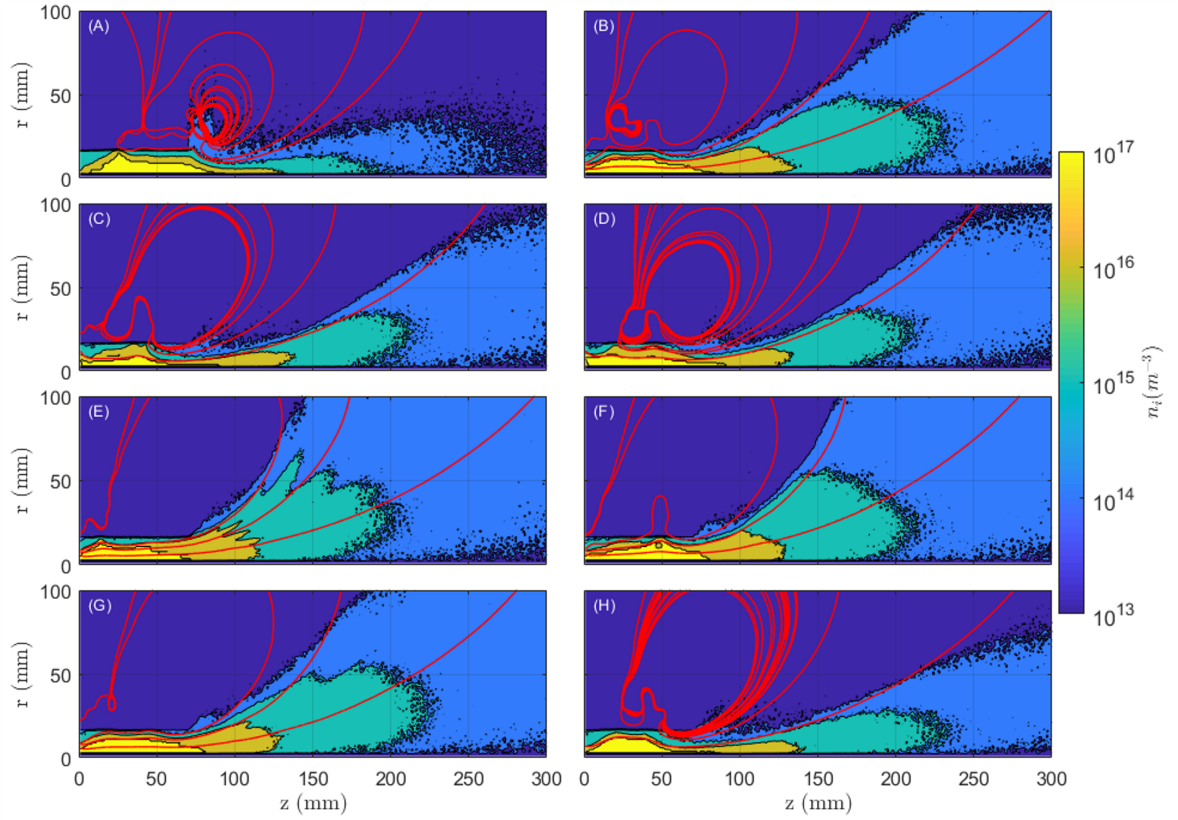


FIGURE 4.13: Ar ion distributions of $n_i(r, z)$ determined by simulating eight different magnet configurations (A to H) Ω^* in axisymmetric (r, z) coordinates during a quasi-steady state discharge ($5.6\mu s$). Magnetic flux lines are shown in red.

Figure 4.13 it is apparent that there is a positive correlation between plume confinement and \bar{v}_z . The more confined results (A and H) have the largest \bar{v}_z , and the results with lowest confinement (G and E) have the smallest \bar{v}_z .

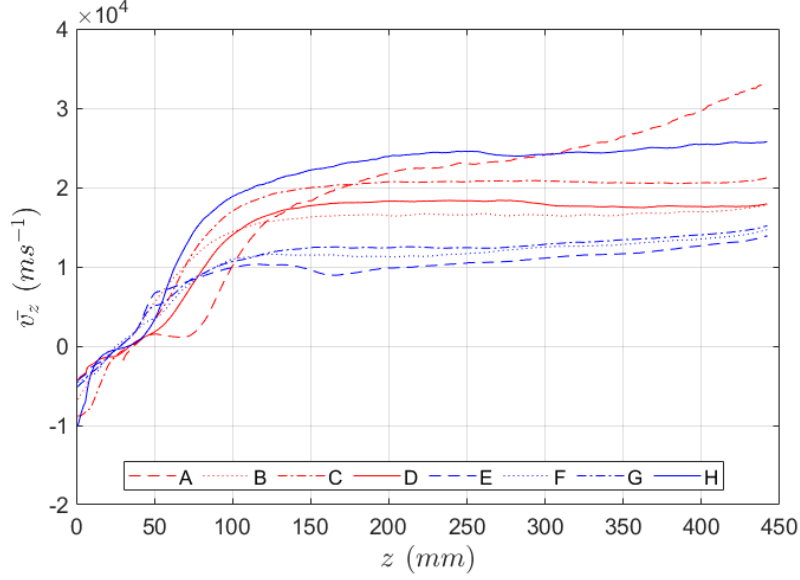


FIGURE 4.14: Comparison of \bar{v}_z determined from simulation results for all eight tested configurations Ω_i^*

To get a qualitative measure of performance for each configuration Ω_i^* , the thrust is calculated. The total thrust of each configuration as a function of z can be approximated in simulation as,

$$T(z_k) = \frac{\bar{v}_z^2(z_k) \cdot \sum m_i(z_k)}{\Delta z} \quad (4.9)$$

Here $\bar{v}_z(z_k)$ is the mean axial velocity of ions taken between each discrete axial cell (of width Δz) location in the simulation domain z_k , and $\sum m_i(z_k)$ is the total mass of ions at z_k (within Δz). It is critical to measure thrust at the correct location to predict the thrust from a real propulsion system. As each solution produced magnetic field magnitudes of a similar order of magnitude (0.1T) and the ion flux into the system is the same for all simulations (there is a discrepancy in flux loss due to wall losses and mirroring), relative ion detachment is related to magnetic nozzle curvature [30]. By using a reference plane S prior to the ion detachment plane ($> 150\text{mm}$, supported by plateaus in the v_z results in Figure 4.14), a consistent comparison could be made across each candidate. We assume an upper bound for thrust in the cases where v_z decreases due to non-detached ions and magnetic curvature (as observed in Figure 4.12 (E)). We assert that this is an effective strategy for a relative comparison between candidates, considering the currently unachievable computational requirements for accurately determining the ion detachment plane in the optimisation loop using PIC simulation.

TABLE 4.1: Analysis of simulation results for each configuration Ω_i^* including mean ion speed \bar{v}_z , mean ion kinetic energy \bar{E}_k and total thrust $T \pm \Delta T$ with 3σ uncertainty.

Ω_i^*	$\mathcal{F}_2(\Omega_i^*)$	\bar{v}_z ($\times 10^4 m s^{-1}$)	\bar{E}_k (eV)	T mN	$\Delta T(3\sigma)$ (mN)
A	0.131	2.03	121	0.30	0.09
B	0.496	1.65	68.7	1.5	0.1
C	0.326	2.04	100	0.96	0.11
D	0.237	1.81	80.5	0.88	0.08
E	0.311	0.93	27.5	0.82	0.12
F	0.346	1.14	37.1	1.01	0.09
G	0.437	1.24	42.6	1.21	0.11
H	0.313	2.31	122	0.9	0.2

There is a direct correlation shown in the results in Figure 4.15 between the squared objective function score $\mathcal{F}_2(\Omega^*)^2$ and the thrust T determined through simulation.

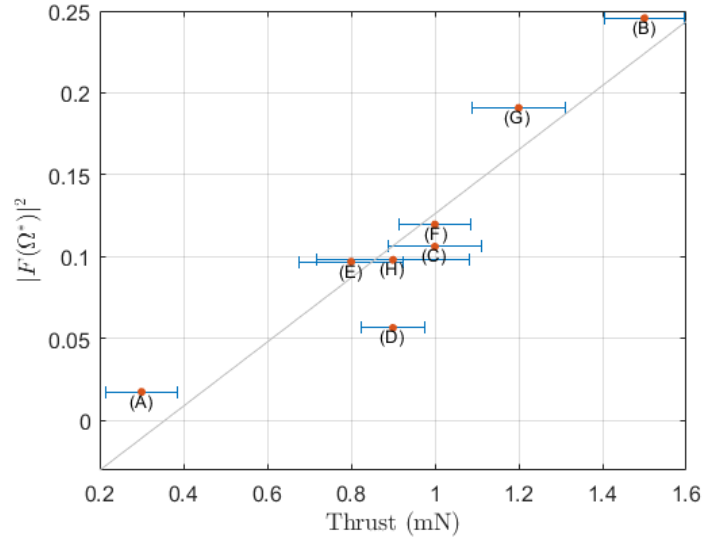


FIGURE 4.15: Comparison of $\mathcal{F}_2(\Omega^*)^2$ and thrust T measured in simulation showing positive correlation, thus validating \mathcal{F}_2 against PIC simulation (post \mathcal{F}_2 tuning).

The \mathcal{F}_2 tuning parameters γ_i (see Equation 4.1) found in this study are [0.8,0.02,0.7,3], fit using the eight candidates A to H presented in this section. The values for γ_i are determined using simulated annealing with an objective score equivalent to the Pearson correlation coefficient between simulated thrust and objective score \mathcal{F}_2 for prior simulations. Prior to tuning, when all γ_i are unity as outlined in Section 4.2.3.1, the Pearson coefficient is 0.7, and after tuning it is 0.9.

Further insight into the performance of the RF plasma sources using these particle-in-cell models will be covered in a separate study. As previously shown in a study of cathodic arc discharge jets that used similar models, these

fully kinetic axisymmetric models can be used to determine wave-particle interactions, ion energy distributions, and higher ion state behaviour [149].

4.4 Experimental validation

To confirm the validity of the evolutionary optimisation strategy and objective function \mathcal{F}_2 used in this study, the momentum flux for candidates $\Omega_A^* \Omega_B^*$ was measured experimentally. Using the magnetic configurations developed to validate the magnetic field approximation in Section 4.3.3, two thrusters were built by inserting a copper helicon antenna, borosilicate plasma boundary, and opposing flow propellant injector (shown in Figure 4.17). Design aspects for each thruster were kept consistent, aside from the magnetic configuration, and the physical confinement of plasma to percent plasma impingement for each configuration. All components were additively fabricated out of PVDF aside from the antenna and the central part of the plasma boundary. To hold the three-dimensional array of cubic NdFeB magnets (Figure 4.9) in place, additive manufacturing was required. PVDF (also called Kynar) was chosen due to its strength, low outgassing, ability to flex so that magnetics can be secured with tight tolerances, and ease of extrusion. PVDF can be printed on a traditional Fused Deposition Modelling (FDM) printer at comparable extruder and print bed temperatures to Acrylonitrile Butadiene Styrene (ABS), a common filament used in additive manufacturing. The NdFeB magnetic elements (example shown in Figure 4.16) fit into the PVDF vessel is shown in Figure 4.18. Each element of the final configured thruster using the magnetic field design Ω_A^* is also shown in Figure 4.18. More details on the thruster designs for Ω_A^* and Ω_B^* including overall dimensions can be found in Appendix C.

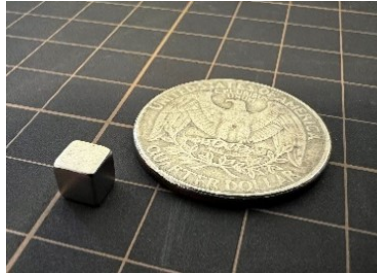


FIGURE 4.16: Example of one of the $3 \times 3 \times 3\text{mm}^3$ NdFeB magnets, shown next to a US quarter on a 1cm^2 grid for size comparison.

A diagram of the apparatus used to test each configuration is shown in Figure 4.19 along with the apparatus itself in Figure 4.20. To effectively test the difference performance of each magnetic configuration, the same plasma source was used. This source is a half-helix helicon antenna that surrounds a borosilicate tube, and there is a PVDF nozzle and backing at the front and end of the tube respectively. The physical PVDF nozzles are designed to conform to the outer magnetic flux lines leaving the plasma source (for example the line of flux shown in Figure 4.12 between 50mm and 80mm will be bounded by the physical nozzle). The purpose of the

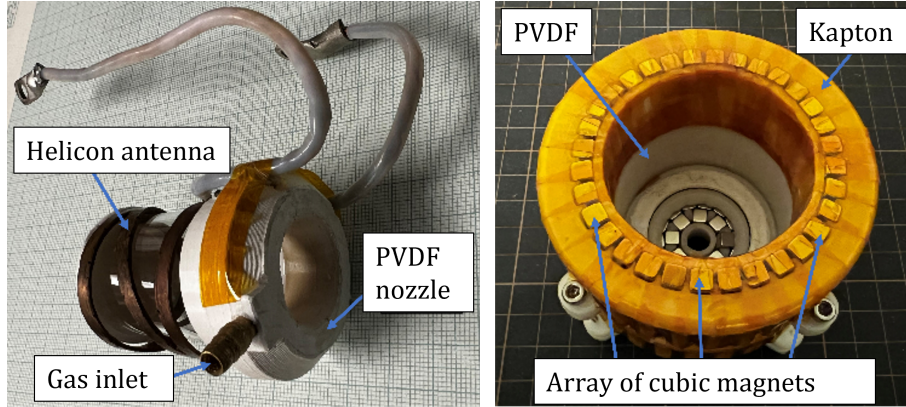


FIGURE 4.17: Plasma source components including copper helicon antenna, propellant injection, and plasma confinement (left) as well as the fabricated PVDF and NdFeB array for Ω_B^* (right).

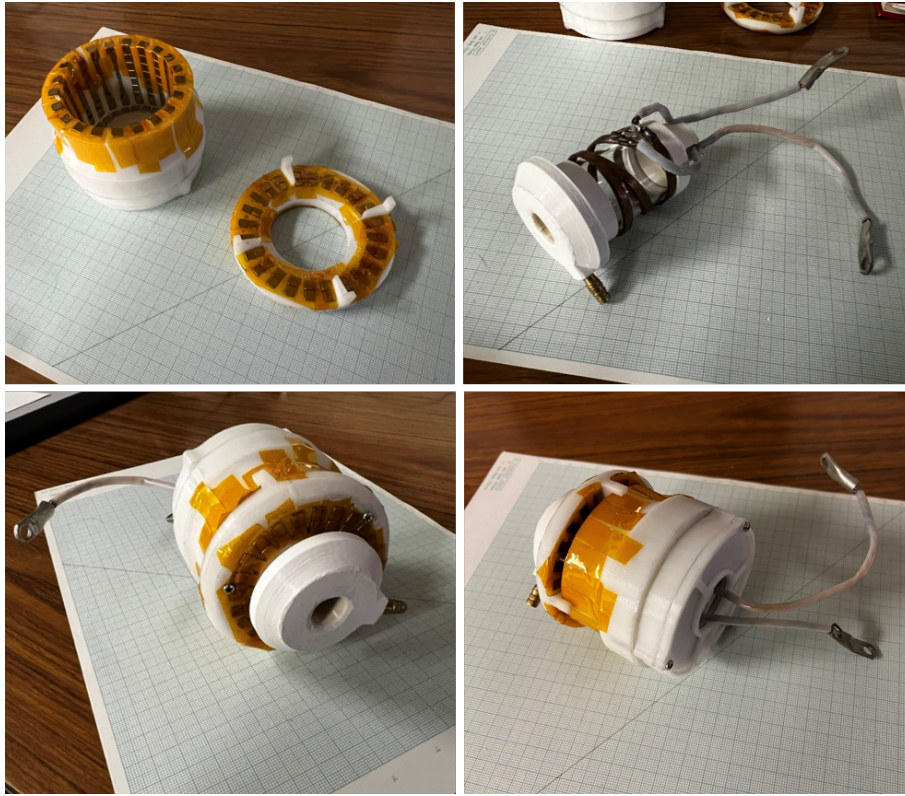


FIGURE 4.18: Final assembly for Ω_B^* showing the PVDF vessel with inserted magnets prior to completion (top left), the modified helicon plasma source module (top right), and the assembled final thruster (bottom).

physical nozzle is to ensure gas flow is within the magnetic nozzle prior to ionisation, and to prevent radial plasma loss in the acceleration region. The propellant is injected downwards from the top, in a configuration demonstrated to improve performance by Takahashi et al. [90].

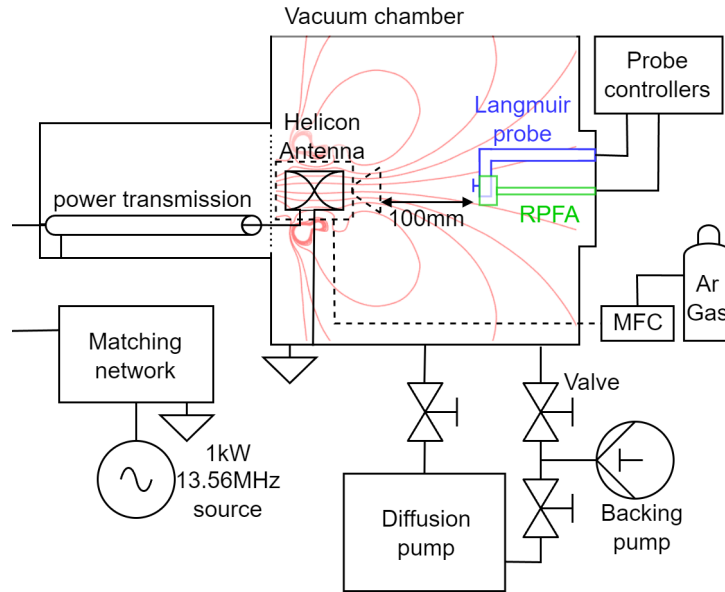


FIGURE 4.19: Diagram of the plasma diagnostic apparatus used, including Langmuir probe (blue), RPA (green), thruster housing and propellant line (dashed lines), example magnetic flux lines (red), and RF power delivery. Not to scale unless indicated.

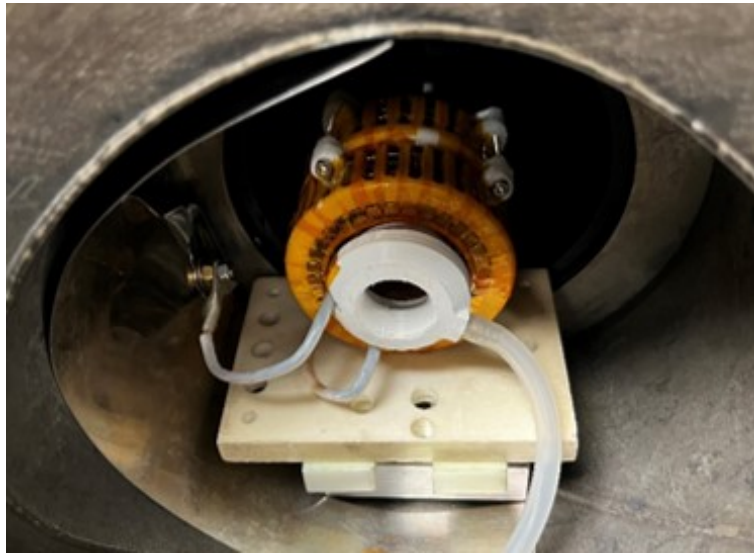


FIGURE 4.20: An optimised RF thruster (system B) inside the vacuum chamber, with magnet array, helicon plasma source, and a Borosilicate/PVDF physical plasma nozzle.

For consistency the forward power to the helicon antenna was maintained at $100W$, and the chamber pressure was kept at $2mTorr$ when injecting Argon propellant ($0.05mTorr$ base pressure). Measurements of ion density and energy were taken using a Langmuir probe and Retarding Potential Analyser (RPA) at an axial displacement of $100mm$ from the thruster exit ($170mm$ from the origin in the coordinate system used in this study). The L shaped geometry of the Langmuir probe mount allowed for radial measurements to be taken across the plasma

plume by rotating the probe (shown in two locations in Figure 4.21). The diagnostic configuration reflects the one used to undertake the study in Chapter 3 (Figure 3.13).

The plume visually conforming to the magnetic field lines for configuration A in Figure 4.21 (left), whereas the magnetic field effects are not as clear for configuration B due to visual quality. The relative broadness of the plumes of each discharge aligns qualitatively with the simulation results shown in Figure 4.12.



FIGURE 4.21: RF thrusters using magnetic configurations A (left) and B (right) operating at 50W power and 25sccm Ar flow rate at 2mTorr vacuum pressure. Langmuir probe also shown, located at 100mm from thruster exit.

For this study the expected ion energy is taken as normal to the RPA grid, $E_{z_{ion}} = E_{ion}$, therefore an analysis of Figure 4.22 produces the axial ion drift velocity v_z for each configuration. The ion energy distribution for Ω_B^* is typical, exhibiting a Maxwellian structure with a peak at 51eV. The distribution for Ω_A^* is bimodal, exhibiting an expected E_{ion} of 41eV and a peak separation ΔE_{ion} of 42eV. Taking the previous assumption of purely axial motion at the detector, v_z at $z = 170mm$ is $1.4 \times 10^4 ms^{-1}$ and $1.6 \times 10^4 ms^{-1}$ for Ω_A^* and Ω_B^* respectively. As shown in Figure 4.22, these values are smaller than the results predicted in simulation and presented in Table 4.1 (Δv_z between the results for v_z measured in simulation and experimentally of $6300 ms^{-1}$ and $820 ms^{-1}$ for Ω_A^* and Ω_B^* respectively) at this axial location, as expected due to the omission of neutrals and collisions in the PIC models used.

The measurements of n_i shown in Figure 4.23 are consistent with the simulation results in Figure 4.12 with a peak value in the order of $1 \times 10^{15} m^{-3}$ close to the z-axis. The measurements for Ω_A^* are also less broad than Ω_B^* as predicted by the simulation models. There is an outlier in the measurements of n_i for Ω_B^* at a radial distance of 40mm, this is likely due to uncertainty in the ion saturation measurement.

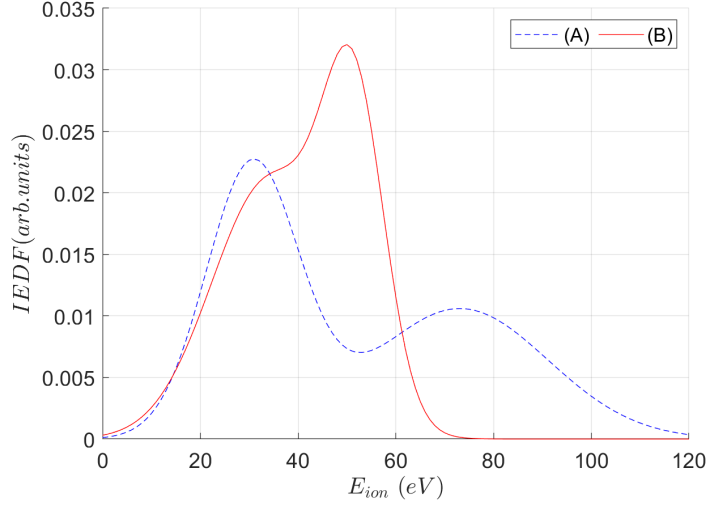


FIGURE 4.22: RPA data analysis showing normalised gaussian fits of Ar ion energy distributions at $100mm$ from the thruster exit ($z = 170mm$), and centred on the thruster z -axis for configurations A (dashed line) and B (solid line).

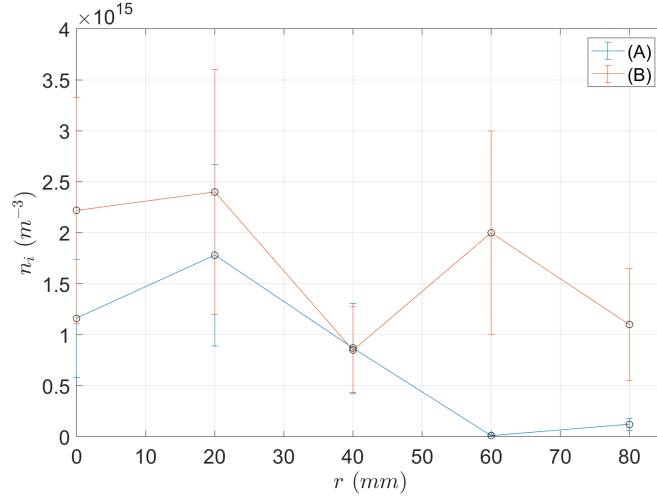


FIGURE 4.23: Experimentally measured radial profile of Ar ion number density n_i at $z = 170mm$ ($100mm$ from thruster exit) for configurations Ω_A^* (blue) and Ω_B^* (red), taken using a round planar Langmuir probe of area $1.75cm^2$.

Integrating the Ar ion number density n_i in r between $0mm$ and $80mm$ as shown in Figure 4.23 and taking the expected axial ion speeds v_z measured previously, gives an implied thrust ratio R_T between configurations Ω_A^* and Ω_B^* at $z = 170mm$ by using,

$$R_{TBA} = \frac{T_B}{T_A} = \frac{2\pi \langle v_z \rangle_B^2 \int_{r_1}^0 r n_i(r)_B dr}{2\pi \langle v_z \rangle_A^2 \int_{r_1}^0 r n_i(r)_A dr} \quad (4.10)$$

where T_A and T_B are the experimental measurements of thrust for each configuration, calculated using ion momentum flux through the circular area of radius 80mm normal to the z-axis ($r = 0$). The resulting values for T_A and T_B are $0.19 \pm 0.09mN$ and $0.5 \pm 0.2mN$ respectively. The value $R_{T_{BA}}$ of 2.6 ± 2.3 demonstrates the increase in performance from configuration Ω_A^* to Ω_B^* . $R_{T_{BA}}$ allows for a more direct comparison to the simulation results. Considering the uncertainty in T_A and T_B , $R_{T_{BA}}$ is 2.6 ± 2.3 , supporting the simulated prediction of thrust ratio $R'_{T_{BA}}$ of 5 ± 0.2 , and confirming the increase in thrust performance from Ω_A^* to Ω_B^* .

The discrepancy between $R'_{T_{BA}}$ and $R_{T_{BA}}$ of 2.4 is attributed to two factors. As each thrust result omits the effects of neutrals and charge exchange on total thrust, these are lower bounds on the experimentally determined thrust for each configuration. Furthermore, for the calculation T_B a portion of the n_i is cut off beyond the 80mm swept radius of the Langmuir probe. The out-of-range density measurements explain the lower-than-expected result, in-part, when compared to the thrust predicted in simulation of $1.5mN$ (Table 4.1).

The results demonstrate experimentally that the objective function $\mathcal{F}_2(\Omega^*)$ effectively reflects real thrust performance, validating its use for inverse design of magnetic fields for RF plasma systems. Given a forward power of 100W in both configurations, the thrust efficiencies η_t are $1.9 \times 10^{-3}mNW^{-1}$ and $5 \times 10^{-3}mNW^{-1}$. Additionally for specific impulses I_{sp} for Ω_A^* and Ω_B^* for the flow rate of 25sccm or $4.5 \times 10^{-5}kg s^{-1}$, are 435s and 1145s respectively. To further validate the results presented here, a future study will be performed using a μN thrust stand.

4.5 Conclusions

A genetic optimisation strategy was successfully applied to the thrust performance optimisation of the applied magnetic field (from a permanent magnet array of cubic NdFeB elements) used in an RF propulsion system. This included the demonstration of two objective functions with differing methods. The objective function to fit desired magnetic vector fields (\mathcal{F}_1) successfully converged to a desired field topology, producing the design for magnetic configuration Ω_A^* . Improvements were found by applying an objective function that made minimal assumptions about the desired field topology, and instead used a simplified analytical model of RF thrust performance and a series of metrics that characterised predicted plasma behaviour (\mathcal{F}_2). The function \mathcal{F}_2 also rapidly converged on improved solutions such as Ω_B^* , although further improvements could potentially be made with more compute resources.

Using objective function \mathcal{F}_2 scores for eight magnetic configurations Ω_i^* (including Ω_A^*) and particle-in-cell simulation, a positive correlation between the objective function and thrust performance was found both prior to and post tuning of γ_i . The trend is illustrated in Figure 4.15, showing a monotonically increasing relationship between the objective function score \mathcal{F}_2 and simulated thrust T within uncertainty for all candidates.

Final validation of both the optimisation strategy and the simulation models was undertaken via an experimental analysis of ion momentum flux for Ω_A^* and Ω_B^* . The results confirmed a performance increase between the two configurations as anticipated by the objective function scores increasing for $\mathcal{F}_2(\Omega_A^*)$ to $\mathcal{F}_2(\Omega_B^*)$ with a ratio $R_{T_{B/A}}$ of 2.6. The measured thrust also validated the PIC simulation models for Ω_A^* and Ω_B^* with experimentally measured ion speeds and plasma densities consistent with those predicted in simulations. Additionally, after multiple tests the NdFeB magnets began to heat, so future design iterations will use ferromagnetic materials with a higher heat conductivity than PVDF to extract heat.

The methods presented have demonstrated broad applicability for the rapid optimisation of RF plasma sources using large numbers of individual magnetic elements more generally. The study validates the use of genetic algorithms to accurately configure cubic magnetic elements in three dimensions based on axisymmetric assumptions, with applications beyond plasma sources, and offers a supporting example for the use of evolutionary algorithms to solve multi-parameter problems in areas such as electromagnetic systems and more broadly.

4.5.1 Future work

The PIC models used to simulate the plasma dynamics of the devices studied in Chapters 3 and 4 omit the process of RF coupling and ionisation of the plasma within each thruster. With further computational resources and model optimisation, the RF breakdown and coupling effects can be investigated in future PIC models by modelling the antenna and including other classical electromagnetic behaviour (Maxwell's equations). Another assumption is that the plasma is collisionless, and future PIC models will incorporate collisional processes to test their impact on simulated plasma behaviour.

The optimisation strategies presented herein are planned for the generative design and performance improvement for other electric propulsion systems, such as pulsed plasma thrusters, Hall Effect thrusters and ion thrusters. The methods studied in the thesis will be adapted to optimise design characteristics beyond thrust and specific impulse, including materials, cost, lifetime, and reliability.

Further strategies for topology optimisation of magnetic fields and plasma-based devices will be explored in future, such as adjoint methods, gaussian process regression-based meta-models, and convolutional neural networks. The presented objective functions will also be expanded to use the PIC simulation results directly, rather than the current method exhibited here, with PIC models being used to validate the objective score derived from the analysis of magnetostatic simulations. If successful, a demonstration of PIC simulation-based inverse design and optimisation is possible for any device incorporating a plasma process.

Bibliography

- [1] K. E. Tsiolkovsky, 'Exploration of the universe with reaction machines,' *The Science Review*, vol. 5, 1903.
- [2] C. Koppel and G. Quinsac, 'Electric thruster selection criteria,' in *8th European Conference for Aeronautics and Space Sciences (EUCASS)*, 2019.
- [3] W. Crookes, *On radiant matter [microform] : a lecture delivered to the British Association for the Advancement of Science, at Sheffield, Friday, August 22, 1879 / by William Crookes*, English. London, 1879, 30 p., [1] folded leaf of plates :
- [4] L. Tonks, 'The birth of "plasma",' *American Journal of Physics*, vol. 35, no. 9, pp. 857–858, 1967. DOI: [10.1119/1.1974266](https://doi.org/10.1119/1.1974266).
- [5] F. F. Chen *et al.*, *Introduction to plasma physics and controlled fusion*. Springer, 1984, vol. 1.
- [6] D. M. Goebel and I. Katz, *Fundamentals of electric propulsion: ion and Hall thrusters*. John Wiley & Sons, 2008.
- [7] M. A. Lieberman and A. J. Lichtenberg, *Principles of plasma discharges and materials processing*. John Wiley & Sons, 2005.
- [8] P. Chabert, T. V. Tsankov and U. Czarnetzki, 'Foundations of capacitive and inductive radio-frequency discharges,' *Plasma Sources Science and Technology*, vol. 30, no. 2, p. 024 001, 2021.
- [9] J. Lehané and P. Thonemann, 'An experimental study of helicon wave propagation in a gaseous plasma,' *Proceedings of the Physical Society (1958-1967)*, vol. 85, no. 2, p. 301, 1965.
- [10] R. Boswell, 'Plasma production using a standing helicon wave,' *Physics Letters A*, vol. 33, no. 7, pp. 457–458, 1970.
- [11] F. F. Chen, 'Helicon discharges and sources: A review,' *Plasma Sources Science and Technology*, vol. 24, no. 1, p. 014 001, 2015.
- [12] T. Shoji, Y. Sakawa, S. Nakazawa, K. Kadota and T. Sato, 'Plasma production by helicon waves,' *Plasma Sources Science and Technology*, vol. 2, no. 1, p. 5, 1993.
- [13] P. A. Keiter, E. E. Scime and M. M. Balkey, 'Frequency dependent effects in helicon plasmas,' *Physics of Plasmas*, vol. 4, no. 7, pp. 2741–2747, 1997.
- [14] F. F. Chen, 'Plasma ionization by helicon waves,' *Plasma Physics and Controlled Fusion*, vol. 33, no. 4, p. 339, 1991.

- [15] S. Shinohara, 'Helicon high-density plasma sources: Physics and applications,' *Advances in Physics: X*, vol. 3, no. 1, p. 1 420 424, 2018.
- [16] O. A. Popov, *High density plasma sources: design, physics and performance*. Elsevier, 1996.
- [17] R. Geller, *Electron cyclotron resonance ion sources and ECR plasmas*. Routledge, 2018.
- [18] A. Anders, *Cathodic arcs: from fractal spots to energetic condensation*. Springer Science Business Media, 2009, vol. 50, ISBN: 0387791086.
- [19] J. E. Polk, M. J. Sekerak, J. K. Ziemer, J. Schein, N. Qi and A. Anders, 'A theoretical analysis of vacuum arc thruster and vacuum arc ion thruster performance,' *IEEE Transactions on Plasma Science*, vol. 36, no. 5, pp. 2167–2179, 2008.
- [20] G. Y. Yushkov, A. Anders, E. M. Oks and I. G. Brown, 'Ion velocities in vacuum arc plasmas,' *Journal of Applied Physics*, vol. 88, no. 10, pp. 5618–5622, 2000, ISSN: 0021-8979.
- [21] R. Sanginés, A. Israel, I. Falconer, D. McKenzie and M. Bilek, 'Production of highly ionized species in high-current pulsed cathodic arcs,' *Applied Physics Letters*, vol. 96, no. 22, p. 221 501, 2010, ISSN: 0003-6951.
- [22] K. F. Luskow *et al.*, 'Particle-in-cell simulation of the cathodic arc thruster,' *Physics of Plasmas*, vol. 25, no. 1, p. 013 508, 2018, ISSN: 1070-664X.
- [23] J. E. Polk *et al.*, 'A theoretical analysis of vacuum arc thruster performance,' 2001.
- [24] A. Anders and G. Y. Yushkov, 'Ion flux from vacuum arc cathode spots in the absence and presence of a magnetic field,' *Journal of Applied Physics*, vol. 91, no. 8, pp. 4824–4832, 2002, ISSN: 0021-8979.
- [25] I. Beilis, *Plasma and Spot Phenomena in Electrical Arcs*. Springer Nature, 2020, vol. 113, ISBN: 3030447472.
- [26] S. Berger, D. McKenzie and P. Martin, 'EELS analysis of vacuum arc-deposited diamond-like films,' *Philosophical Magazine Letters*, vol. 57, no. 6, pp. 285–290, 1988, ISSN: 0950-0839.
- [27] S. Andersen, V. O. Jensen, P. Nielsen and N. D'Angelo, 'Continuous supersonic plasma wind tunnel,' *The Physics of Fluids*, vol. 12, no. 3, pp. 557–560, 1969.
- [28] E. Ahedo and M. Merino, 'Two-dimensional supersonic plasma acceleration in a magnetic nozzle,' *Physics of Plasmas*, vol. 17, no. 7, p. 073 501, 2010.
- [29] A. Fruchtman, K. Takahashi, C. Charles and R. Boswell, 'A magnetic nozzle calculation of the force on a plasma,' *Physics of Plasmas*, vol. 19, no. 3, p. 033 507, 2012.
- [30] J. M. Little, 'Performance scaling of magnetic nozzles for electric propulsion,' *Ph. D. Thesis*, 2015.
- [31] M. Merino, J. Mauriño and E. Ahedo, 'Kinetic electron model for plasma thruster plumes,' *Plasma Sources Science and Technology*, vol. 27, no. 3, p. 035 013, 2018.
- [32] T. Collard and B. Jorns, 'Magnetic nozzle efficiency in a low power inductive plasma source,' *Plasma Sources Science and Technology*, vol. 28, no. 10, p. 105 019, 2019.

- [33] E. Ahedo, S. Correyero, J. Navarro-Cavallé and M. Merino, 'Macroscopic and parametric study of a kinetic plasma expansion in a paraxial magnetic nozzle,' *Plasma Sources Science and Technology*, vol. 29, no. 4, p. 045 017, 2020.
- [34] Z. Chen, Y. Wang, J. Ren, H. Tang, P. Wu and M. Li, 'The fully-kinetic investigations on the ion acceleration mechanisms in an electron-driven magnetic nozzle,' *Plasma Sources Science and Technology*, vol. 31, no. 5, p. 055 013, 2022.
- [35] C. Charles, R. Boswell, A. Bouchoule, C. Laure and P. Ranson, 'Plasma diffusion from a low pressure radio frequency source,' *Journal of Vacuum Science & Technology A: Vacuum, Surfaces, and Films*, vol. 9, no. 3, pp. 661–663, 1991.
- [36] R. A. Gerwin, G. J. Marklin, A. G. Sgro and A. H. Glasser, 'Characterization of plasma flow through magnetic nozzles,' LOS ALAMOS NATIONAL LAB NM, Report, 1990.
- [37] T. M. York, B. A. Jacoby and P. Mikellides, 'Plasma flow processes within magnetic nozzle configurations,' *Journal of propulsion and Power*, vol. 8, no. 5, pp. 1023–1030, 1992.
- [38] B. W. Longmier *et al.*, 'Ambipolar ion acceleration in an expanding magnetic nozzle,' *Plasma Sources Science and Technology*, vol. 20, no. 1, p. 015 007, 2011.
- [39] A. V. Arefiev and B. N. Breizman, 'Ambipolar acceleration of ions in a magnetic nozzle,' *Physics of Plasmas*, vol. 15, no. 4, p. 042 109, 2008.
- [40] J. M. Little and E. Y. Choueiri, 'Thrust and efficiency model for electron-driven magnetic nozzles,' *Physics of Plasmas*, vol. 20, no. 10, p. 103 501, 2013.
- [41] F. Díaz, 'An overview of the vasimr engine: High power space propulsion with rf plasma generation and heating,' *AIP Conference Proceedings*, vol. 595, pp. 3–15, Oct. 2001. DOI: [10.1063/1.1424142](https://doi.org/10.1063/1.1424142).
- [42] A. Sasoh, 'Simple formulation of magnetoplasma dynamic acceleration,' *Physics of plasmas*, vol. 1, no. 3, pp. 464–469, 1994.
- [43] K. Takahashi, T. Lafleur, C. Charles, P. Alexander and R. W. Boswell, 'Axial force imparted by a current-free magnetically expanding plasma,' *Physics of Plasmas*, vol. 19, no. 8, p. 083 509, 2012.
- [44] C. Charles and R. Boswell, 'Current-free double-layer formation in a high-density helicon discharge,' *Applied Physics Letters*, vol. 82, no. 9, pp. 1356–1358, 2003.
- [45] E. Hooper, 'Plasma detachment from a magnetic nozzle,' *Journal of Propulsion and Power*, vol. 9, no. 5, pp. 757–763, 1993.
- [46] A. V. Arefiev and B. N. Breizman, 'Magnetohydrodynamic scenario of plasma detachment in a magnetic nozzle,' *Physics of Plasmas*, vol. 12, no. 4, p. 043 504, 2005.
- [47] E. Ahedo and M. Merino, 'On plasma detachment in propulsive magnetic nozzles,' *Physics of Plasmas*, vol. 18, no. 5, p. 053 504, 2011.
- [48] M. Merino and E. Ahedo, 'Plasma detachment in a propulsive magnetic nozzle via ion demagnetization,' *Plasma Sources Science and Technology*, vol. 23, no. 3, p. 032 001, 2014.

- [49] Z. Chen, Y. Wang, J. Ren, P. Wu, M. Li and H. Tang, 'Numerical investigation of 'detachment cone' in the magnetic nozzle,' in *the 36th Int. Electric Conf*, 2019, pp-324.
- [50] R. W. Moses Jr, R. A. Gerwin and K. F. Schoenberg, 'Resistive plasma detachment in nozzle based coaxial thrusters,' in *AIP Conference Proceedings*, American Institute of Physics, vol. 246, 1992, pp. 1293–1303.
- [51] K. Takahashi, T. Sugawara and A. Ando, 'Spatially-and vector-resolved momentum flux lost to a wall in a magnetic nozzle rf plasma thruster,' *Scientific reports*, vol. 10, no. 1, pp. 1–11, 2020.
- [52] M. Merino-Martinez and E. Ahedo, 'Magnetic nozzle far-field simulation,' in *48th AIAA/ASME/SAE/ASEE Joint Propulsion Conference & Exhibit*, 2012, p. 3843.
- [53] D. O'Reilly, G. Herdrich and D. F. Kavanagh, 'Electric propulsion methods for small satellites: A review,' *Aerospace*, vol. 8, no. 1, p. 22, 2021.
- [54] J. Brophy, C. Garner, B. Nakazono, M. Marcucci, M. Henry and D. Noon, 'The ion propulsion system for dawn,' in *39th AIAA/ASME/SAE/ASEE Joint Propulsion Conference and Exhibit*, 2003, p. 4542.
- [55] I. Funaki, K. Nishiyama, H. Kuninaka, K. Toki, Y. Shimizu and H. Toki, '20mn-class microwave discharge ion thruster,' in *27th International Electric Propulsion Conference, IEPC-01-103, Pasadena, USA*, 2001, pp. 15–19.
- [56] M. Tsay, K. Hohman, N. Rosenblad, E. Ehrbar, M. Robin and C. Farnell, 'Micro radio-frequency ion propulsion system,' in *48th AIAA/ASME/SAE/ASEE Joint Propulsion Conference & Exhibit*, 2012, p. 3947.
- [57] M. Sangregorio, X. Kan, W. Ningfei, G. Ning and Z. Zhang, 'Ion engine grids: Function, main parameters, issues, configurations, geometries, materials and fabrication methods,' *Chinese Journal of Aeronautics*, vol. 31, no. 8, pp. 1635–1649, 2018.
- [58] J. Polk *et al.*, 'An overview of the results from an 8200 hour wear test of the nstar ion thruster,' in *35th Joint Propulsion Conference and Exhibit*, 1999, p. 2446.
- [59] M. Tsay, J. Frongillo, J. Zwahlen and L. Paritsky, 'Maturation of iodine fueled bit-3 rf ion thruster and rf neutralizer,' in *52nd AIAA/SAE/ASEE Joint Propulsion Conference*, 2016, p. 4544.
- [60] C. R. Koppel and D. Estublier, 'The smart-1 hall effect thruster around the moon: In flight experience,' in *29th International electric propulsion conference*, 2005, p. 119.
- [61] A. Bapat, P. B. Salunkhe and A. V. Patil, 'Hall-effect thrusters for deep-space missions: A review,' *IEEE Transactions on Plasma Science*, 2022.
- [62] N. P. Brown and M. L. Walker, 'Review of plasma-induced hall thruster erosion,' *Applied Sciences*, vol. 10, no. 11, p. 3775, 2020.
- [63] V. Désangles *et al.*, 'Fast camera analysis of plasma instabilities in hall effect thrusters using a pod method under different operating regimes,' *Atmosphere*, vol. 11, no. 5, p. 518, 2020.

- [64] N. Maslennikov, 'Lifetime of the stationary plasma thruster,' in *IEPC'95- International Electric Propulsion Conference, 24 th, Moscow, Russia*, 1996, pp. 505–514.
- [65] I. G. Mikellides, I. Katz, R. R. Hofer and D. M. Goebel, 'Magnetic shielding of a laboratory hall thruster. i. theory and validation,' *Journal of Applied Physics*, vol. 115, no. 4, p. 043 303, 2014.
- [66] V. Vekselman, Y. E. Krasik, S. Gleizer, V. T. Gurovich, A. Warshavsky and L. Rabinovich, 'Characterization of a heaterless hollow cathode,' *Journal of Propulsion and Power*, vol. 29, no. 2, pp. 475–486, 2013.
- [67] D. R. Lev, I. G. Mikellides, D. Pedrini, D. M. Goebel, B. A. Jorns and M. S. McDonald, 'Recent progress in research and development of hollow cathodes for electric propulsion,' *Reviews of Modern Plasma Physics*, vol. 3, no. 1, pp. 1–89, 2019.
- [68] M. SCHATZ, 'Heaterless ignition of inert gas ion thruster hollow cathodes, a86—17833,' USA: NASA, Tech. Rep., 1986.
- [69] G. Aston, 'Ferm cathode operation in the test bed ion engine,' in *International Electric Propulsion Conference*, 1984.
- [70] D. Bock and M. Tajmar, 'Highly miniaturized feep propulsion system (nanofeep) for attitude and orbit control of cubesats,' *Acta Astronautica*, vol. 144, pp. 422–428, 2018.
- [71] C. Ma and C. N. Ryan, 'The design and characterization of a porous-emitter electrospray thruster (pet-100) for interplanetary cubesats,' in *7th Interplanetary CubeSat Workshop*, 2018, pp. 01 309–01 309.
- [72] M. Tajmar, A. Genovese and W. Steiger, 'Indium field emission electric propulsion microthruster experimental characterization,' *Journal of propulsion and power*, vol. 20, no. 2, pp. 211–218, 2004.
- [73] K. K. Jameson, *Investigation of hollow cathode effects on total thruster efficiency in a 6 kW Hall thruster*. University of California, Los Angeles, 2008.
- [74] H.-b. Tang, X.-a. Zhang, Y. Liu, H.-x. Wang and Y. Shen, 'Performance and preliminary life test of a low power hydrazine engineering design model arcjet,' *Aerospace Science and Technology*, vol. 15, no. 7, pp. 577–588, 2011.
- [75] A. V. Arefiev and B. N. Breizman, 'Theoretical components of the vasmr plasma propulsion concept,' *Physics of Plasmas*, vol. 11, no. 5, pp. 2942–2949, 2004. DOI: [10.1063/1.1666328](https://doi.org/10.1063/1.1666328).
- [76] F. R. C. Diaz, M. Giambusso, A. M. Corrigan, L. O. Dean and M. F. Warrayat, 'Recent progress on the vasmr® engine iepc-2022-525,' 2022.
- [77] M. Coletti, 'A thrust formula for an mpd thruster with applied-magnetic field,' *Acta Astronautica*, vol. 81, no. 2, pp. 667–674, 2012.
- [78] A. Boxberger, A. Behnke and G. Herdrich, 'Current advances in optimization of operative regimes of steady state applied field mpd thrusters,' in *36th International Electric Propulsion Conference*, 2019.

- [79] A. Kodys and E. Choueiri, 'A critical review of the state-of-the-art in the performance of applied-field magnetoplasmadynamic thrusters,' in *41st AIAA/ASME/SAE/ASEE Joint Propulsion Conference & Exhibit*, 2005, p. 4247.
- [80] R. L. Burton and P. Turchi, 'Pulsed plasma thruster,' *Journal of Propulsion and Power*, vol. 14, no. 5, pp. 716–735, 1998.
- [81] M. Keidar *et al.*, 'Magnetically enhanced vacuum arc thruster,' *Plasma Sources Science and Technology*, vol. 14, no. 4, p. 661, 2005.
- [82] T. Zhuang, A. Shashurin, T. Denz, M. Keidar, P. Vail and A. Pancotti, 'Performance characteristics of micro-cathode arc thruster,' *Journal of Propulsion and Power*, vol. 30, no. 1, pp. 29–34, 2014.
- [83] P. Neumann, M. Bilek, R. Tarrant and D. McKenzie, 'A pulsed cathodic arc spacecraft propulsion system,' *Plasma Sources Science and Technology*, vol. 18, no. 4, p. 045 005, 2009.
- [84] Y. A. Alexeev, M. N. Kazeev and V. F. Kozlov, 'Energy transfer to the propellant in high power ppt,' in *4th International Spacecraft Propulsion Conference*, vol. 555, 2004.
- [85] E. Michaux, S. Mazouffre and A. Blanchet, 'Time evolution of plasma parameters in the jet of a low-power vacuum arc thruster,' *Journal of Electric Propulsion*, vol. 1, no. 1, pp. 1–16, 2022.
- [86] S. Bathgate, M. Bilek and D. Mckenzie, 'Electrodeless plasma thrusters for spacecraft: A review,' *Plasma Science and Technology*, vol. 19, no. 8, p. 083 001, 2017.
- [87] T. Collard and J. P. Sheehan, 'Preliminary measurements of an integrated prototype of the cubesat ambipolar thruster,' in *52nd AIAA/SAE/ASEE Joint Propulsion Conference*, ser. AIAA Propulsion and Energy Forum. American Institute of Aeronautics and Astronautics, 2016. DOI: [doi:10.2514/6.2016-5042](https://doi.org/10.2514/6.2016-5042).
- [88] G. F. Crimi, *Investigation of a Microwave Generated Plasma in a Non-Uniform Magnetic Field*. University of Pennsylvania, 1967.
- [89] K. Takahashi, 'Helicon-type radiofrequency plasma thrusters and magnetic plasma nozzles,' *Reviews of Modern Plasma Physics*, vol. 3, no. 1, pp. 1–61, 2019.
- [90] K. Takahashi, 'Magnetic nozzle radiofrequency plasma thruster approaching twenty percent thruster efficiency,' *Scientific reports*, vol. 11, no. 1, pp. 1–12, 2021, ISSN: 2045-2322.
- [91] M. Manente *et al.*, 'Regulus: A propulsion platform to boost small satellite missions,' *Acta Astronautica*, vol. 157, pp. 241–249, 2019.
- [92] PhaseFour, *Maxwell*, May 2022. [Online]. Available: <https://phasefour.io/maxwell/>.
- [93] D. O'Reilly, G. Herdrich and D. F. Kavanagh, 'Electric propulsion methods for small satellites: A review,' *Aerospace*, vol. 8, no. 1, p. 22, 2021, ISSN: 2226-4310.
- [94] W. Yueqing *et al.*, 'Comparison of double layer in argon helicon plasma and magnetized dc discharge plasma,' *Plasma Science and Technology*, vol. 24, no. 3, p. 035 401, 2022.

- [95] K. Takahashi, C. Charles, R. Boswell and A. Ando, 'Performance improvement of a permanent magnet helicon plasma thruster,' *Journal of Physics D: Applied Physics*, vol. 46, no. 35, p. 352 001, 2013.
- [96] O. Popov, 'Characteristics of electron cyclotron resonance plasma sources,' *Journal of Vacuum Science & Technology A: Vacuum, Surfaces, and Films*, vol. 7, no. 3, pp. 894–898, 1989.
- [97] D. Packan *et al.*, 'H2020 minotor: Magnetic nozzle electron cyclotron resonance thruster,' in *Proc. 36th Int. Electr. Propuls. Conf.(IEPC)*, 2019.
- [98] M. Inchingolo, M. Merino and J. Navarro-Cavallé, 'Direct thrust measurements of a circular waveguide electron cyclotron resonance thruster,' 2022.
- [99] J. Jarrige, P.-Q. Elias, D. Packan and F. Cannat, 'Characterization of a coaxial ecr plasma thruster,' in *44th AIAA Plasmadynamics and Lasers Conference*, 2013, p. 2628.
- [100] C. Birdsall and A. Langdon, *Plasma Physics via Computer Simulation*. Taylor Francis, 2004, ISBN: 9780750310253. [Online]. Available: <https://books.google.com.au/books?id=S21qqDTm6a4C>.
- [101] R. Hofer, I. Mikellides, I. Katz and D. Goebel, 'Wall sheath and electron mobility modeling in hybrid-pic hall thruster simulations,' in *43rd AIAA/ASME/SAE/ASEE Joint Propulsion Conference & Exhibit*, 2007, p. 5267.
- [102] E. J. Horowitz, D. E. Shumaker and D. V. Anderson, 'Qn3d: A three-dimensional quasi-neutral hybrid particle-in-cell code with applications to the tilt mode instability in field reversed configurations,' *Journal of Computational physics*, vol. 84, no. 2, pp. 279–310, 1989.
- [103] H.-y. Wang, W. Jiang and Y.-n. Wang, 'Implicit and electrostatic particle-in-cell/monte carlo model in two-dimensional and axisymmetric geometry: I. analysis of numerical techniques,' *Plasma Sources Science and Technology*, vol. 19, no. 4, p. 045 023, 2010.
- [104] J. Cary *et al.*, 'Validation of computation by experiment for the vsim and usim codes,' *Bulletin of the American Physical Society*, vol. 62, 2017.
- [105] V. K. Decyk, 'Description of spectral particle-in-cell codes from the upic framework,' *Presentation at ISSS-10*, 2011.
- [106] H. Timkó, '2d arc-pic code description: Methods and documentation,' Report, 2011.
- [107] D. Meeker *et al.*, *Finite Element Method Magnetics*. 2017, vol. 4.
- [108] C. K. Birdsall, 'Particle-in-cell charged-particle simulations, plus monte carlo collisions with neutral atoms, pic-mcc,' *IEEE Transactions on plasma science*, vol. 19, no. 2, pp. 65–85, 1991.
- [109] F. Taccogna, S. Longo, M. Capitelli and R. Schneider, 'Self-similarity in hall plasma discharges: Applications to particle models,' *Physics of Plasmas*, vol. 12, no. 5, p. 053 502, 2005. DOI: [10.1063/1.1877517](https://doi.org/10.1063/1.1877517).
- [110] K. Huang, *Statistical mechanics*. John Wiley & Sons, 2008.

- [111] T. Yuan, J. Ren, J. Zhou, Z. Zhang, Y. Wang and H. Tang, 'The effects of numerical acceleration techniques on pic-mcc simulations of ion thrusters,' *AIP Advances*, vol. 10, no. 4, p. 045 115, 2020.
- [112] T. Binder, M. Pfeiffer, S. Fasoulas and H. Leiter, 'High-fidelity particle-in-cell simulations of ion thruster optics,' in *Proc. 35th Int. Electr. Propuls. Conf.*, 2017, pp. 1–19.
- [113] R. Courant, K. Friedrichs and H. Lewy, 'On the partial difference equations of mathematical physics,' *IBM journal of Research and Development*, vol. 11, no. 2, pp. 215–234, 1967.
- [114] K. Yee, 'Numerical solution of initial boundary value problems involving maxwell's equations in isotropic media,' *IEEE Transactions on antennas and propagation*, vol. 14, no. 3, pp. 302–307, 1966.
- [115] R. Procassini, C. Birdsall and E. Morse, 'A fully kinetic, self-consistent particle simulation model of the collisionless plasma–sheath region,' *Physics of Fluids B: Plasma Physics*, vol. 2, no. 12, pp. 3191–3205, 1990, ISSN: 0899-8221.
- [116] S. Zöhrer, A. Anders and R. Franz, 'Time-resolved ion energy and charge state distributions in pulsed cathodic arc plasmas of nb al cathodes in high vacuum,' *Plasma Sources Science and Technology*, vol. 27, no. 5, p. 055 007, 2018, ISSN: 0963-0252.
- [117] A. Anders, 'Ion energies in vacuum arcs: A critical review of data and theories leading to traveling potential humps,' in *2014 International Symposium on Discharges and Electrical Insulation in Vacuum (ISDEIV)*, IEEE, pp. 201–204, ISBN: 1479967521.
- [118] A. Anders, 'The fractal nature of vacuum arc cathode spots,' *IEEE Transactions on Plasma Science*, vol. 33, no. 5, pp. 1456–1464, 2005, ISSN: 0093-3813.
- [119] E. M. Oks, A. Anders, I. Brown, M. Dickinson and R. MacGill, 'Ion charge state distributions in high current vacuum arc plasmas in a magnetic field,' *IEEE Transactions on Plasma Science*, vol. 24, no. 3, pp. 1174–1183, 1996, ISSN: 0093-3813.
- [120] Q. Sun, W. Yang and Q. Zhou, '2d simulation of a copper cathode spot jet considering the charge composition in vacuum arc,' *Physics of Plasmas*, vol. 27, no. 5, p. 053 501, 2020, ISSN: 1070-664X.
- [121] L. Wang, S. Jia, Z. Shi and M. Rong, 'Numerical simulation of vacuum arc under different axial magnetic fields,' *Journal of Physics D: Applied Physics*, vol. 38, no. 7, p. 1034, 2005, ISSN: 0022-3727.
- [122] H. Timko *et al.*, 'Mechanism of surface modification in the plasma-surface interaction in electrical arcs,' *Physical Review B*, vol. 81, no. 18, p. 184 109, 2010.
- [123] W. Yang, Q. Zhou, Q. Sun and Z. Dong, 'Two-dimensional particle simulation on the behavior of multi-charged copper ions in the cathode spot of a pulsed vacuum arc discharge,' *Journal of Applied Physics*, vol. 126, no. 24, p. 243 303, 2019, ISSN: 0021-8979.
- [124] D. Wang, L. Wang, J. Liu and S. Jia, '2d particle-in-cell/monte carlo collisional simulation of the plasma initiation in the vacuum breakdown stage,' *Journal of Physics D: Applied Physics*, vol. 53, no. 3, p. 035 201, 2019, ISSN: 0022-3727.

- [125] D. Shmelev, S. Barengolts, I. Uimanov, M. Tsventoukh and K. Savkin, 'On plasma jet formation in vacuum arc with composite cathode,' in *Journal of Physics: Conference Series*, vol. 652, IOP Publishing, p. 012 041, ISBN: 1742-6596.
- [126] I. Cooper and D. McKenzie, 'All particle simulations of cathodic arc plasmas,' *Journal of applied physics*, vol. 99, no. 9, p. 093 304, 2006, ISSN: 0021-8979.
- [127] H. Kaufmann, M. Cunha, M. Benilov, W. Hartmann and N. Wenzel, 'Detailed numerical simulation of cathode spots in vacuum arcs: Interplay of different mechanisms and ejection of droplets,' *Journal of Applied Physics*, vol. 122, no. 16, p. 163 303, 2017, ISSN: 0021-8979.
- [128] D. Shmelev, I. Uimanov and V. Frolova, 'Modeling of plasma jet of vacuum arc with copper-chromium cathode under action of strong axial magnetic field,' in *Journal of Physics: Conference Series*, vol. 1393, IOP Publishing, p. 012 025, ISBN: 1742-6596.
- [129] R. Jaafarian, A. Ganjovi and G. Etaati, 'Study of the operating parameters of a helicon plasma discharge source using pic-mcc simulation technique,' *Physics of Plasmas*, vol. 25, no. 1, p. 013 510, 2018.
- [130] T. Lafleur *et al.*, 'Helicon wave propagation in low diverging magnetic fields.,' 2011.
- [131] T. Lafleur, 'Helicon plasma thruster discharge model,' *Physics of Plasmas*, vol. 21, no. 4, p. 043 507, 2014.
- [132] A. Ilin, F. Chan, J. Squire, A. Tarditi, B. Breizman and M. Carter, 'Simulation of plasma detachment in vasmr,' in *40th AIAA Aerospace Sciences Meeting & Exhibit*, 2002, p. 346.
- [133] F. Cichocki, J. Navarro-Cavallé, A. Modesti and G. Ramirez Vázquez, 'Magnetic nozzle and rpa simulations vs. experiments for a helicon plasma thruster plume,' *Frontiers in Physics*, p. 260, 2022.
- [134] Y. Hu and J. Wang, 'Fully kinetic simulations of collisionless, mesothermal plasma emission: Macroscopic plume structure and microscopic electron characteristics,' *Physics of Plasmas*, vol. 24, no. 3, p. 033 510, 2017.
- [135] Y. Hu, Z. Huang, Y. Cao and Q. Sun, 'Kinetic insights into thrust generation and electron transport in a magnetic nozzle,' *Plasma Sources Science and Technology*, vol. 30, no. 7, p. 075 006, 2021.
- [136] S. Di Fede, M. Magarotto, S. Andrews and D. Pavarin, 'Simulation of the plume of a magnetically enhanced plasma thruster with spis,' *Journal of Plasma Physics*, vol. 87, no. 6, p. 905 870 611, 2021. DOI: [10.1017/S0022377821001057](https://doi.org/10.1017/S0022377821001057).
- [137] S. Andrews, S. Di Fede and M. Magarotto, 'Fully kinetic model of plasma expansion in a magnetic nozzle,' *Plasma Sources Science and Technology*, vol. 31, no. 3, p. 035 022, 2022.
- [138] A. Y. Piggott, J. Lu, K. G. Lagoudakis, J. Petykiewicz, T. M. Babinec and J. Vučković, 'Inverse design and demonstration of a compact and broadband on-chip wavelength demultiplexer,' *Nature Photonics*, vol. 9, no. 6, pp. 374–377, 2015.

- [139] C. V. Pop, M. Essaid, L. Idoumghar and D. Fodorean, 'Novel differential evolutionary optimization approach for an integrated motor-magnetic gear used for propulsion systems,' *IEEE Access*, vol. 9, pp. 142 114–142 128, 2021, ISSN: 2169-3536.
- [140] T. Fahey, A. Muffatti and H. Ogawa, 'High fidelity multi-objective design optimization of a downscaled cusped field thruster,' *Aerospace*, vol. 4, no. 4, p. 55, 2017, ISSN: 2226-4310.
- [141] R. Boichot and Y. Fan, 'A genetic algorithm for topology optimization of area-to-point heat conduction problem,' *International Journal of Thermal Sciences*, vol. 108, pp. 209–217, 2016, ISSN: 1290-0729.
- [142] J. H. Holland, 'Genetic algorithms,' *Scientific american*, vol. 267, no. 1, pp. 66–73, 1992, ISSN: 0036-8733.
- [143] S. Cheng and D. P. Arnold, 'Optimization of permanent magnet assemblies using genetic algorithms,' *IEEE transactions on magnetics*, vol. 47, no. 10, pp. 4104–4107, 2011, ISSN: 0018-9464.
- [144] S. H. Yeo, H. Ogawa, D. Kahnfeld, L. Lewerentz and R. Schneider, 'Improved modeling for design optimization of cusped field thrusters with support of kinetic analysis,' *Acta Astronautica*, vol. 195, pp. 465–480, 2022, ISSN: 0094-5765.
- [145] C. Z. Cooley *et al.*, 'Design of sparse halbach magnet arrays for portable mri using a genetic algorithm,' *IEEE transactions on magnetics*, vol. 54, no. 1, pp. 1–12, 2017, ISSN: 0018-9464.
- [146] J. Degraeve *et al.*, 'Magnetic control of tokamak plasmas through deep reinforcement learning,' *Nature*, vol. 602, no. 7897, pp. 414–419, 2022, ISSN: 1476-4687.
- [147] K. I. Parker, 'State-of-the-art for small satellite propulsion systems,' 2016.
- [148] C. Charles, R. Boswell and M. Lieberman, 'Xenon ion beam characterization in a helicon double layer thruster,' *Applied Physics Letters*, vol. 89, no. 26, p. 261 503, 2006.
- [149] A. G. Ryan, M. M. Bilek, I. H. Cairns and D. R. McKenzie, 'Magnetised and unmagnetized axisymmetric particle-in-cell simulations of ion energy distributions in cathodic vacuum arcs,' *Plasma Sources Science and Technology*, 2022, ISSN: 0963-0252.
- [150] P. Neumann, M. Bilek, R. Tarrant and D. McKenzie, 'A pulsed cathodic arc spacecraft propulsion system,' *Plasma Sources Science and Technology*, vol. 18, no. 4, p. 045 005, 2009, ISSN: 0963-0252.
- [151] G. A. Mesyats and S. A. Barengol'ts, 'Mechanism of anomalous ion generation in vacuum arcs,' *Physics-Uspekhi*, vol. 45, no. 10, p. 1001, 2002, ISSN: 1063-7869.
- [152] L. Ryves, D. R. McKenzie and M. M. Bilek, 'Cathode-spot dynamics in a high-current pulsed arc: A noise study,' *IEEE transactions on plasma science*, vol. 37, no. 2, pp. 365–368, 2009, ISSN: 0093-3813.
- [153] S. A. Barengolts, G. A. Mesyats and D. L. Shmelev, 'Structure and time behavior of vacuum arc cathode spots,' *IEEE transactions on plasma science*, vol. 31, no. 5, pp. 809–816, 2003, ISSN: 0093-3813.
- [154] P. Siemroth, B. Schultrich and T. Schülke, 'Fundamental processes in vacuum arc deposition,' *Surface and Coatings Technology*, vol. 74, pp. 92–96, 1995, ISSN: 0257-8972.

- [155] K. Oh, D. Kalanov and A. Anders, ‘High-resolution observation of cathode spots in a magnetically steered vacuum arc plasma source,’ *Plasma Sources Science and Technology*, vol. 30, no. 9, p. 095 005, 2021, ISSN: 0963-0252.
- [156] B. Shadwick and C. Schroeder, ‘Physical fidelity in particle-in-cell modeling of small debye-length plasmas,’ in *AIP Conference Proceedings*, vol. 1086, American Institute of Physics, pp. 321–327, ISBN: 0735406170.
- [157] S. Hohenbild, C. Grübel, G. Y. Yushkov, E. M. Oks and A. Anders, ‘A study of vacuum arc ion velocities using a linear set of probes,’ *Journal of Physics D: Applied Physics*, vol. 41, no. 20, p. 205 210, 2008, ISSN: 0022-3727.
- [158] V. Krasov and V. Paperny, ‘Expansion of a multicomponent current-carrying plasma jet into vacuum,’ *Plasma Physics Reports*, vol. 43, no. 3, pp. 298–306, 2017, ISSN: 1562-6938.
- [159] A. G. Ryan, M. M. Bilek, I. H. Cairns and D. R. McKenzie, ‘Experimental validation of the use of additive manufacturing and metaheuristic inverse design to develop an electrodeless plasma thruster,’ in *73rd International Astronautical Congress*, p. 71 482.
- [160] A. G. Ryan and J. Olsen, ‘Application of particle-in-cell simulation techniques in the analysis and optimisation of magnetic nozzle geometries,’ in *68th International Astronautical Congress*, p. 37 321.
- [161] P. Di Barba, *Multiobjective shape design in electricity and magnetism*. Springer, 2010, vol. 47.
- [162] J. P. Sheehan, B. W. Longmier, I. Reese and T. Collard, ‘New low-power plasma thruster for nanosatellites,’ in *50th AIAA/ASME/SAE/ASEE Joint Propulsion Conference*, ser. AIAA Propulsion and Energy Forum. American Institute of Aeronautics and Astronautics, 2014. DOI: [doi:10.2514/6.2014-3914](https://doi.org/10.2514/6.2014-3914).
- [163] J. P. Sheehan, T. A. Collard, M. E. Ostermann, E. T. Dale, B. N. Wachs and B. W. Longmier, ‘Initial operation of the cubesat ambipolar thruster,’ in *2015 IEEE International Conference on Plasma Sciences (ICOPS)*, pp. 1–1, ISBN: 0730-9244. DOI: [10.1109/PLASMA.2015.7179981](https://doi.org/10.1109/PLASMA.2015.7179981).
- [164] F. F. Chen, ‘Physics of helicon discharges,’ *Physics of Plasmas*, vol. 3, no. 5, pp. 1783–1793, 1996. DOI: [10.1063/1.871697](https://doi.org/10.1063/1.871697).
- [165] S. C. Plaza, J. Jarrige, D. Packan and E. Ahedo, ‘Ion acceleration in the magnetic nozzle of an ecr thruster: Comparison of experimental measurements with a quasi 1d kinetic model,’ in *Space Propulsion 2018*, 2018.
- [166] F. Ebersohn, S. Girimaji, D. Staack, J. Shebalin, B. Longmier and C. Olsen, ‘Magnetic nozzle plasma plume: Review of crucial physical phenomena,’ in *48th AIAA/ASME/SAE/ASEE Joint Propulsion Conference & Exhibit*, 2012, p. 4274.
- [167] F. F. Chen, ‘Langmuir probe diagnostics,’ in *Mini-Course on Plasma Diagnostics, IEEEICOPS meeting, Jeju, Korea*, 2003, pp. 20–111.

- [168] I. H. Hutchinson, 'Principles of plasma diagnostics,' *Plasma Physics and Controlled Fusion*, vol. 44, no. 12, p. 2603, 2002.
- [169] R. Castro *et al.*, 'A comparative study of single and double langmuir probe techniques for rf plasma characterization,' *Contributions to Plasma Physics*, vol. 39, no. 3, pp. 235–246, 1999.
- [170] S. N. Bathgate, 'The use of magnetic fields to create high-speed plasma jets for spacecraft propulsion,' Ph.D. dissertation, 2017.
- [171] B. Breizman, M. Tushentsov and A. Arefiev, 'Magnetic nozzle and plasma detachment model for a steady-state flow,' *Physics of Plasmas*, vol. 15, no. 5, p. 057 103, 2008, ISSN: 1070-664X.
- [172] M. Ortner and L. G. C. Bandeira, 'Magpylib: A free python package for magnetic field computation,' *SoftwareX*, vol. 11, p. 100 466, 2020.

Appendix

Appendix A

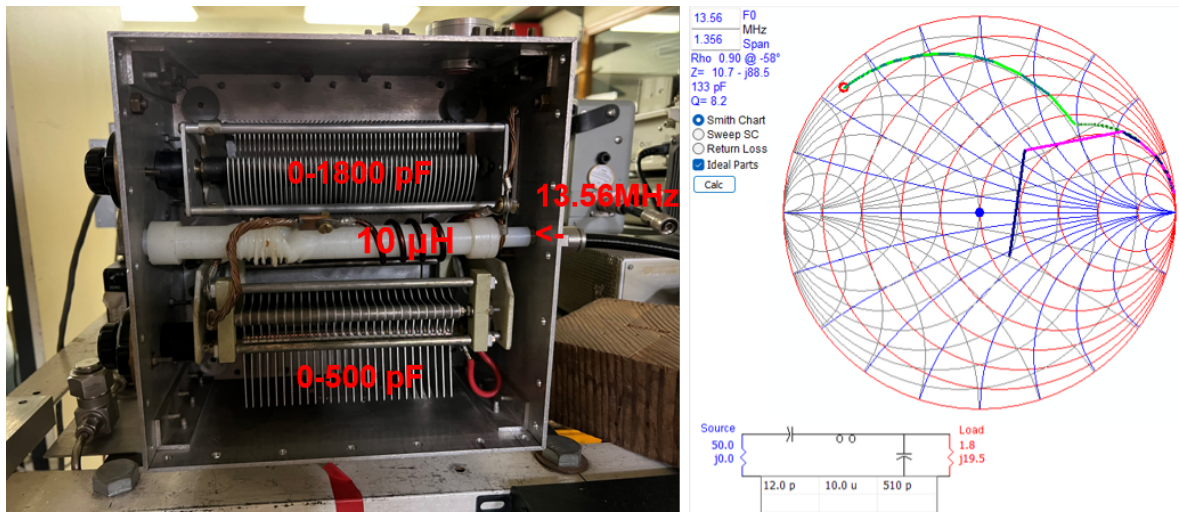


FIGURE 4.24: The modified matching network previously developed at the University of Sydney [170], now with a $10\mu H$ inductor to work with the helicon antenna used in the thesis (left), along with the smith chart confirming a match for the vector impedance measured to be 29Ω at 87° (Section 3.4.1) (right). The circuit diagram for the matching network is also shown (bottom right).

Appendix B

The following is an example of the Matlab objective function code used as part of the implementation of objective function method 1 \mathcal{F}_1 in Section 4.2.3.1.

```

vectors2 = 0;

%determine B field vectors are locations of interest
baseBrz = mo_getb(1, 40);
5 topBrz = mo_getb(1, 100);
base = sqrt(baseBrz(1)^2+ baseBrz(2)^2);
top = sqrt(topBrz(1)^2+ topBrz(2)^2);

vec_1 = 1;
10 vec_2 = 1;

% Apply a cost to vectors that lie outside the required thresholds
for vi = 40:10:70
    vrz = mo_getb(15, vi);
15 if (vrz(2)/norm(vrz) >= 0.7) && (vrz(1) <= 0)
        vectors1 = 1.0;
    else
        vectors1 = 0.01;
    end
20 vec_1 = vec_1*vectors1;
end

for vi2 = 72:10:93
    vj2 = (-5 / 13) * vi2 + 555 / 13;
25 vrz2 = mo_getb(vj2, vi2);
    vrz2(1)/norm(vrz2);
    if (vrz2(1)/norm(vrz2) <= -0.2) && (vrz2(2) >= 0.0)
        vectors2 = 1.0;
    else
30 vectors2 = 0.01;
    end
    vec_2 = vec_2*vectors2;
end

```

```
35  if (vec_1 * vec_2) == 1
    ramp = (top-base) / base;
else
    ramp = 0.0;
end

40  % return final score
    magscore = vec_1 * vec_2 + ramp;
```

Appendix C

